.

A Gain Calibration System for Accurate Measurements of Cosmic Microwave Background Polarization at POLARBEAR-2 Experiment

TAKATORI, Sayuri

The Graduate University for Advanced Studies,
SOKENDAI

December 10, 2021

ABSTRACT

The Big Bang cosmology, which explains the universe's evolution, is supported by many observational facts, but there are still mysteries, such as the horizon and flatness problems. However, these problems can be solved by assuming that a rapid accelerating expansion of space-time, called cosmic inflation, occurred before the hot Big Bang universe. The inflationary theory predicts that quantum fluctuations in space-time generate gravitational waves. The inflation theory is well supported by observations of the Cosmic Microwave Background (CMB), but the primordial gravitational waves of inflationary origin have not yet been observed. In this study, we focus on the fact that the generated gravitational waves act on the CMB to produce a unique polarization pattern called "B-mode" on a large angular scale and aim to verify the inflationary theory by observing this B-mode polarization pattern. On the other hand, the B-mode polarization pattern of the CMB is also produced by the gravitational lensing effect caused by the large-scale structure of the universe. This gravitationally lensed B-mode has a peak in the angular power spectrum at a small angular scale of $\ell \sim 1000$. Observing the gravitationally lensed B-mode is also a significant target to estimate the sum of the neutrino masses, $\sum m_\nu$, from the lensing potential of large-scale structures.

POLARBEAR-2 will observe the polarization of the CMB at the Atacama Highlands (5,200 m above sea level) in Chile, South America. POLARBEAR-2 is sensitive to both primordial gravitational wave B-mode polarization and gravitational lensing B-mode polarization because its power spectrum covers a wide range of angular scales ($30 < \ell < 2500$.) The POLARBEAR-2 experiment is sensitive to both B-mode polarization from primordial gravity waves and gravitational lensing effects. In addition, POLARBEAR-2 will install 7588 superconducting detectors (TES) to improve the statistical sensitivity, and simultaneous observations in two frequency bands, 90 GHz and 150 GHz, will help the separation of foreground radiation. We expect to obtain $r \leq 0.01$ (95% C.L.) for the inflationary model, where the parameter r is the tensor-scalar ratio related to the inflationary potential. From the lensing B-mode, we expect $\sum m_\nu \leq 40$ meV (68% C.L.) on the precision of $\sum m_\nu$.

To achieve the above goals, we need to understand the systematic errors in the observations. One of the significant systematic errors arises from the uncertainty of the detector responsivity. The detector used for the observation detects a small signal of the CMB using the sudden change in resistance when the superconductor transitions from a normal to a superconducting state, or vice versa. The detector is biased near the transition temperature for each observation. Therefore, during the observation, the response of the detector is affected by the temperature of the focal plane and atmospheric fluctuations. The stimulator is installed directly behind the secondary mirror of the telescope and emits unpolarized light of constant intensity through a small hole of 9 mm in diameter in the secondary mirror to the receiver and the detector mounted on the receiver. The light source is a high-temperature (1000 K) ceramic heater that emits blackbody radiation over a wide frequency range. A frequency-independent reflective focusing horn enables simultaneous calibration at multiple frequencies. The light is modulated by rotating a chopper. The response of the detectors is evaluated from the output of each bolometer to the modulated signal. Therefore, when calibrating the responsivity of the detector with the stimulator, the time constant is measured by changing the modulation frequency of the signal in steps, and the systematic error from the uncertainty of the time constants is reduced. The stimulator calibration technique will

also be used for future experiments such as Simons Observatory.

We clarified the requirements for the equipment needed for gain calibration and calibration of time constant, designed and developed the stimulator hardware, and conducted performance evaluation tests in the laboratory. The integrated evaluation test at the observation site also confirmed that the stimulator met the requirements. Furthermore, we have demonstrated that the gain calibration with the stimulator can keep the major systematic errors small enough to achieve the target sensitivity of the POLARBEAR-2 experiment, which shows the feasibility of experimental verification of the inflation theory.

Contents

1 Introduction

This thesis describes on the POLARBEAR-2 (PB-2) experiment. The PB-2 is a Cosmic Microwave Background (CMB) polarimetry experiment, which aims to unveil the mystery of the universe. Since CMB's discovery in 1965, CMB observations have given us various information about the universe. In this chapter, I motivate our experiment by providing an overview of the related topics in cosmology. First, I explain the standard model of cosmology and its problem. Then I mention the theory of cosmic inflation. We then discuss the polarization of the CMB again, focusing on the observable consequences of inflation. Finally, this chapter concludes with the status of current CMB polarization measurements. In the next chapter, I explain the PB-2 instrument and detector. In Chapter 3 and Chapter 4, I describe calibration requirements and the gain calibrator I developed. I discuss lab measurements in preparation for our deployment to the Atacama site in Chile in Chapter 5. We also present results from the deployment test in Chile. Finally, I discuss the impact of our future measurements on cosmology in Chapter 6. We summarize the thesis in Chapter 7.

1.1 Standard model of the cosmology

The standard model of cosmology is our current best explanation for many astronomical observations of our universe. In the 1940s, Gamow, Alpher, and Herman advocated the Big Bang Universe, which assumes that the universe was once extremely hot and dense. There are plenty of observations that support the Big Bang theory. Observations of distant luminous objects unveiled that the universe is expanding (Hubble and Humason, 1929 [1]). The Cosmic Microwave Background (Penzias and Wilson, 1965 [2]) and the relative abundance of light elements also support the hot universe in early times. The uniform and isotropic expansion of the universe can be described by General Relativity, which forms the framework of the Big Bang Universe.

1.1.1 Friedmann-Robertson-Walker (FRW) metric

Consider a model which assumes that the universe is uniform and isotropic. The model is consistent with observations on scales of over 100 Mpc. A uniform and isotropic universe can be categorized: flat (3-D Euclidean), closed (3-D spherical), and open (3-D hyperbolic) universes. Let introduce a metric dl which is defined by

$$dl^2 = \frac{dr^2}{1 - Kr^2} + r^2 d\theta^2 + r^2 \sin^2\theta d\phi^2. \tag{1}$$

The curvature of the universe is parametrized by K, where $K = 0$ corresponds to a flat universe, $K > 0$ corresponds to a closed universe, and $K < 0$ to an open universe.

A metric in 4-dimensional space-time is defined by

$$ds^2 = dt^2 - a(t)^2 \left(\frac{dr^2}{1 - Kr^2} + r^2 d\theta^2 + r^2 \sin^2\theta d\phi^2 \right), \tag{2}$$

where c is the speed of light, and $a(t)$ is the Robertson-Walker scale factor. The scale factor $a(t)$ indicates the size of the universe at time t. [1] This metric is known as the Friedmann-Robertson-Walker (FRW) metric. It can be seen that the metric ds in the space component uniformly expands or contracts proportional to the scale factor $a(t)$.

1.1.2 Freedmann equation

How the universe expands depends on the curvature of the universe. The curvature is determined by the amount of matter in the universe and the curvature tensor and the distribution of matter are related to the Einstein equation. The scale factor $a(t)$, which describes the expansion, can be obtained from the Einstein equation,

$$G_{\mu\nu} = 8\pi G T_{\mu\nu}. \tag{3}$$

Here, $G_{\mu\nu}$ is Einstein tensor, G is the gravitational constant and $T_{\mu\nu}$ is the energy-momentum tensor. Under the cosmological principle, the energy-momentum tensor is described as

$$T_{\mu}^{\nu} = \begin{bmatrix} -\rho & 0 & 0 & 0 \\ 0 & p & 0 & 0 \\ 0 & 0 & p & 0 \\ 0 & 0 & 0 & p \end{bmatrix}, \tag{4}$$

where, $\rho(t)$ is the energy density of the fluid and $p(t)$ is pressure of fields. In this case, the Einstein equation leads to a set of simple equations called Friedmann equations,

$$\left(\frac{\dot{a}}{a}\right)^2 = \frac{8\pi G}{3}\rho(t) - \frac{K}{a^2}, \tag{5}$$

$$\frac{\ddot{a}}{a} = -\frac{4\pi G}{3}\left(\rho(t) + 3p(t)\right). \tag{6}$$

If we consider a substance with positive energy and pressure,

$$\rho(t) + 3p(t) > 0, \tag{7}$$

hence the expansion of the universe only decelerates (as $\frac{\ddot{a}}{a} < 0$), due to the gravitational force. The current expansion speed $\dot{a}$ and the acceleration $\ddot{a}$ give the expansion rate at any time. From Eqs. (5)(6), the time evolution of the energy density $\rho(t)$ is given by

$$\dot{\rho} = -\frac{3\dot{a}}{a}\left(\rho + p\right). \tag{8}$$

If we know the pressure p, we can determine the density change in the expansion of the universe. We define the equation of state of matter as follows,

$$\omega \equiv \frac{p}{\rho}. \tag{9}$$

---

[1] Such a coordinate system in which the coordinates themselves do not change in value as space expands is called a co-moving coordinate system and is suitable for describing the motion of a typical observer.

energy	ω	scale factor
relativistic	$\frac{1}{3}$	$a(t) \propto \sqrt{t} (K = 0)$
non-relativistic	0	$a(t) \propto t^{\frac{2}{3}} \ (K = 0)$

Table 1: Time dependence of scale factor.

In a simple case with relativistic elements only, such as radiation traveling with the speed of light, the equation of state is $\omega = \frac{1}{3}$ from statistical mechanics. Assuming $K = 0$,[2] the energy density ρ follows a relation $\rho = a^{-4}\rho_0$ where ρ_0 represents the energy density of the present universe with $a_0 = 1$. Applying this to Eq. (5), we find that $a(t)$ is proportional to $\sqrt{t}$. In case non-relativistic elements are dominant, we obtain $\omega = 0$ because $p \ll \rho$. Accordingly, Eq. (6) leads to the following equation with $p = 0$,

$$\dot{\rho} = -\frac{3\dot{a}}{a}\rho. \tag{10}$$

It results in the energy density $\rho(t) = a^{-3}\rho_0$ and $a(t) \propto t^{\frac{2}{3}}$ from Eq. (5).

To summarize, the time dependence of the scale factor depends on the nature of the energy components as listed in Table 1, and the universe expands with negative acceleration with both relativistic and non-relativistic cases.

The universe is expanding, which means that if we go back in time, the universe was in a hot and dense status in the early universe. As the universe expanded, the temperature and density decreased. The Big Bang cosmology is supported well by (1). Hubble-Lemaitre law, (2). the origin of light elements and (3). the cosmic microwave background radiation.

1.1.3 Problems with the Big Bang

In 1992, the Cosmic Background Explorer satellite (COBE) detected first that the Cosmic Microwave Background (CMB) has an anisotropy of the order of 10^{-5} with the Differential Microwave Radiometer (DMR) [3]. Moreover, the accelerating expansion of the universe and the large-scale structure of galaxies support the Λ Cold Dark Matter (ΛCDM) model of the universe. The ΛCDM model says that the universe is geometrically flat, and the expansion of the universe is accelerating by Dark Energy. However, in spite of the agreement between measurements and the ΛCDM model, fascinating questions with profound implications for physics remain. Two critical questions are the horizon problem and the flatness problem.

1.2 Inflation of the universe

We can solve the problems mentioned in the previous section assuming cosmic inflation; the rapid accelerating expansion of the universe before the hot Big Bang. If a condition

$$\rho(t) + 3p(t) < 0 \tag{11}$$

---

[2] From Eq.5, we obtain $\dot{a}^2 + K = \frac{8}{3}\pi G a^2 \rho$. The right-hand side of the equation is proportional to a^{-1} (a^{-2}) for the non-relativistic (relativistic) case. Hence, in the early universe, i.e. $a \rightarrow 0$, we can assume K is negligibly small.

is satisfied, the universe is expanding with a rate $\frac{\ddot{a}}{a} > 0$. So, we need a driving energy for the inflation. Dividing the energy-momentum tensor into a vacuum term $-\rho_V g_{\mu\nu}$ and a matter term $T^M_{\mu\nu}$, Einstein's equation becomes

$$R_{\mu\nu} - \frac{1}{2}g_{\mu\nu}R = -8\pi G\rho_V g_{\mu\nu} + 8\pi G T^M_{\mu\nu} \equiv G_{\mu\nu}. \tag{12}$$

Introducing a parameter $\Lambda = 8\pi G\rho_V$,

$$G_{\mu\nu} = -\Lambda\delta_{\mu\nu} + 8\pi G T^M_{\mu\nu}. \tag{13}$$

Also, using Λ, we obtain

$$\left(\frac{\dot{a}}{a}\right)^2 = \frac{8\pi G}{3}\rho(t) - \frac{K}{a^2} + \frac{\Lambda}{3} \tag{14}$$

and

$$\frac{\ddot{a}}{a} = -\frac{4\pi G}{3}\left(\rho(t) + 3p(t)\right) + \frac{\Lambda}{3}. \tag{15}$$

The space expands exponentially if Λ is positive and dominant. This model is called the de Sitter universe. The theory of inflation is based on the idea that in the early universe, the universe expanded exponentially for a certain period of time.

1.2.1 Slow-roll inflation

Inflation theory assumes that the universe expanded exponentially during a specific period in the early universe. Here we see how such an expansion can be realized. Guth, who proposed the inflation theory [4], thinks that inflation is caused by a delay in the first-order phase transition, but this idea does not allow for reheating. Therefore such "old" inflation will never end[3]. In 1982, A.D. Linde [5], A. Albrecht, P. Steinhardt [6], proposed a new inflation model, called slow-roll inflation.

In the slow-roll inflation, we introduce a scalar field called the inflaton which has a potential energy, $V(\phi)$. The $V(\phi)$ is assumed to be large and its variation is gentle initially. The scalar field ϕ rolls slowly, thus called "slow-roll,"through the potential in the beginning so that the Hubble constant decreases only slightly during this time, and the universe grows exponentially. As the inflation nears its end, the inflaton oscillates around the local minimum point, converting the energy of the vacuum into that of ordinary matter and radiation, and ending the inflation. This released energy then causes reheating, creating a hot Big Bang Universe as illustrated in Fig. 1.

The energy density $V(\phi)$ of the scalar field ϕ is

$$\rho = \frac{1}{2}\dot{\phi}^2 + V(\phi), \tag{16}$$

and pressure is

$$p = \frac{1}{2}\dot{\phi}^2 - V(\phi). \tag{17}$$

---

[3] This is called the graceful exit problem.

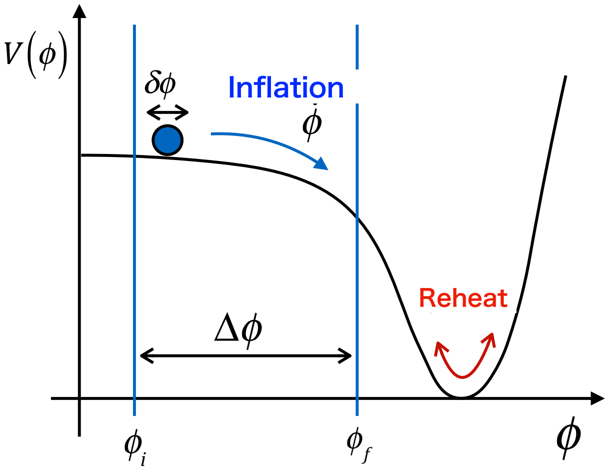

Figure 1: An example of scalar field potential. The potential energy $V(\phi)$ of the scalar field ϕ, call the inflaton, is initially large and with a gentrl variation only. The scalar field thus rolls slowly through the potential so that the Hubble constant decreases only slightly during this time, and the universe expands exponentially.

From Eq. (8), we obtain

$$\dot{\rho} = -3H(\rho(t) + p(t)), \tag{18}$$

$$\ddot{\phi} + 3H\dot{\phi} + V'(\phi) = 0. \tag{19}$$

When the scalar field dominates the energy density of the universe, $H \equiv \frac{\dot{a}}{a}$ is

$$H = \sqrt{\frac{8\pi G\rho}{3}} = \sqrt{\frac{8\pi G}{3}\left\{\frac{1}{2}\dot{\phi}^2 + V(\phi)\right\}}. \tag{20}$$

From Eqs.(19)(20), we obtain

$$2H\dot{H} = \frac{8\pi G\rho}{3}(\dot{\phi}\ddot{\phi} + V'(\phi)\dot{\phi}) = -8\pi GH\dot{\phi}^2, \tag{21}$$

$$\dot{H} = -4\pi G\dot{\phi}^2. \tag{22}$$

To increase the scale factor exponentially, the increase in H during the time interval $\delta t = \frac{1}{H}$ is

$$\left|\frac{\dot{H}}{H}\right|\frac{1}{H} \ll 1, \tag{23}$$

$$\left|\dot{H}\right| \ll H^2. \tag{24}$$

From Eqs.(21)(23), we obtain

$$\dot{\phi}^2 \ll |V(\phi)|\,. \tag{25}$$

Because the potential energy $V(\phi)$ of the scalar field ϕ is large enough, the relation $p \simeq -\rho$ holds and the Hubble parameter becomes

$$H \simeq \sqrt{\frac{8\pi G V(\phi)}{3}}. \tag{26}$$

The increase in $\dot{\phi}$ during the time $\delta t = \frac{1}{H}$ is $\mid \frac{\ddot{\phi}}{\dot{\phi}} \mid \frac{1}{H} \ll 1$. We ignore $\ddot{\phi}$ by using

$$\left|\ddot{\phi}\right| \ll H \left|\dot{\phi}\right|. \tag{27}$$

Eq. (19) becomes

$$\dot{\phi} = -\frac{V'(\phi)}{3H} = -\frac{V'(\phi)}{\sqrt{24\pi G V(\phi)}}. \tag{28}$$

The condition for the derivative of the potential is

$$\left|\frac{V'(\phi)}{V(\phi)}\right| \ll \sqrt{24\pi G}. \tag{29}$$

Also from Eq. (28), we obtain

$$\ddot{\phi} = -\frac{V''(\phi)\dot{\phi}}{3H} + \frac{V'(\phi)\dot{H}}{3H^2} = \frac{V''(\phi)V'(\phi)}{9H^2} - \frac{V'^3}{4\pi G V^2} \tag{30}$$

Therefore, the other condition on the second derivative is

$$\left|\frac{V''(\phi)}{V(\phi)}\right| \ll 24\pi G \tag{31}$$

In the slow-roll inflation, we introduce two parameters, ϵ and η, as follows,

$$\epsilon(\phi) = \frac{M_{\mathrm{P}}^2}{2}\left(\frac{V'}{V}\right) \ll 1, \tag{32}$$

and

$$\eta(\phi) = M_{\mathrm{P}}^2\left(\frac{V''}{V}\right) \ll 1. \tag{33}$$

These are called slow-roll parameter. Here $M_{\mathrm{P}} \equiv \frac{m_{\mathrm{pl}}}{\sqrt{8\pi}}$, m_{pl} is the Planck mass. The slow-roll parameters are related to the scalar spectral index n_s with the following relation,

$$n_s \simeq 1 - 6\epsilon + 2\eta \tag{34}$$

and the tensor-to-scalar ratio with the following relation,

$$r \simeq 16\epsilon. \tag{35}$$

1.2.2 Investigating the inflation model

In the slow-roll inflation model, the magnitude of the quantum fluctuation is related to the potential energy V of the scalar field. The relation is expressed in the tensor-to-scalar ratio r, the ratio of the amplitude of the tensor fluctuation to that of the scalar fluctuation, as follows,

$$V^{\frac{1}{4}} = 1.06 \times 10^{16}\,\mathrm{GeV}\left(\frac{r}{0.01}\right)^{\frac{1}{4}}. \tag{36}$$

For example, many inflation models suggest inflation occurred at the GUT (Grand Unified Theory) scale of $r \approx 0.01$. However, the physics of such large scales is greater than the energy currently attainable in accelerator experiments. So validation through observation of the universe is important. The currently suggested inflation models [7]can be narrowed by more precise measurements of r and n_s.

The latest (Mar 2022) constraint on the parameter is $r < 0.032$ (95% CL) from combination of BICEP/Keck 2018 and Planck PR4 data [8].

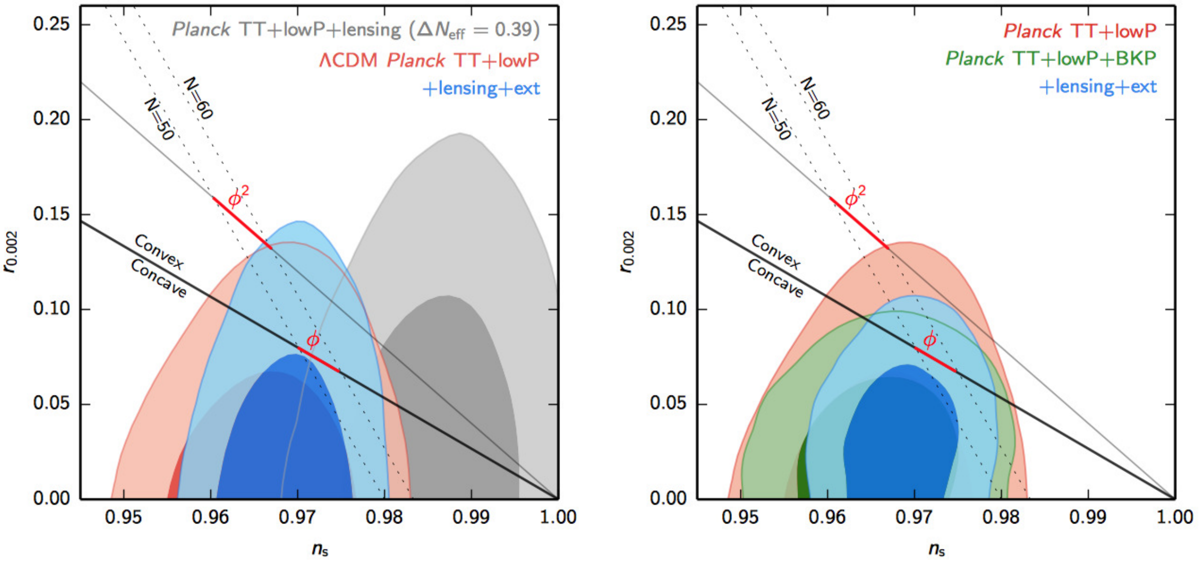

Figure 2: An example of the constraints on the inflation models from CMB observations of the Planck satellite in the r vs. n_s plane [?].

1.2.3 Cosmic microwave background

Observing the Cosmic Microwave Background (CMB) helps us to search inflation models and various physical quantities. We will begin with a detailed explanation of the CMB as an observation target.

Penzias and Wilson in 1965 discovered the CMB for the first time [2]. From this first discovery, there have been many projects for CMB observations. For example, the Far-Infrared Absolute Spectrometer (FIRAS) instrument on the CMB Explorer (COBE) satellite

[9] measured the spectrum of the CMB precisely, which can fit with blackbody radiation at $T_{CMB} = 2.725 \pm 0.001K$ [10].

$$B_\nu(T) = \frac{2h\nu^3}{c^2}\frac{1}{\exp(\frac{h\nu}{k_BT}) - 1}. \tag{37}$$

It strongly suggested the Big Bang universe. Also, Differential Microwave Radiometer (DMR) on the COBE satellite measured the CMB temperature anisotropy at the level of $1/10^5$ on angular scales larger than $\sim$ 7 degrees, as shown in Fig. 3. Furthermore, the Wilkinson Microwave Anisotropy Probe (WMAP) satellite measured the CMB temperature anisotropies with an angular resolution of $\sim$ 0.2 degree as shown in Fig 4. From these observations, we know today that the universe went through the hot and dense Big Bang, which was homogeneous and isotropic. Acoustic oscillations in the primordial plasma created temperature inisotropies. The interaction between photons and charged particles continued until the early universe became much cooler, around a temperature of 3000 K. This moment is called the recombination period, at $\sim$ 380,000 years after the Big bang (z $\sim$1100). After recombination, photons could travel freely, and these photons are called CMB.

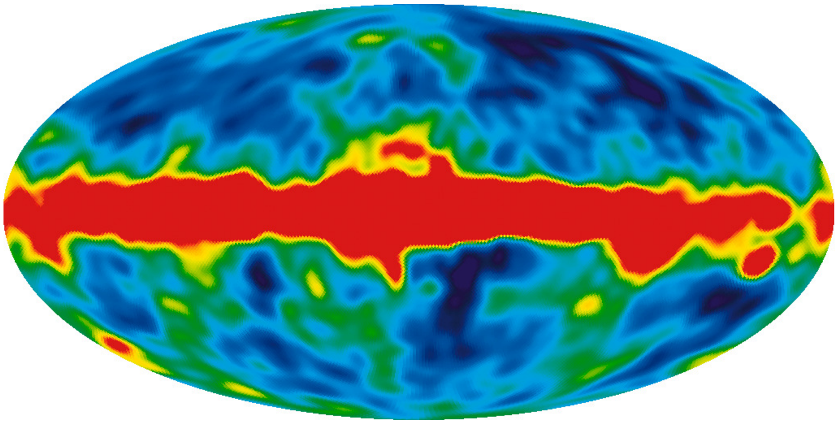

Figure 3: CMB map with COBE DMR's observation for two years. The image by NASA [11].

1.3 CMB power spectrum

To quantitatively analyze the statistical properties of the CMB, we create a two-dimensional map. The map describes the anisotropy on the celestial sphere from the observed data. Then, by expanding it with a spherical harmonic function $Y_\ell^m(\theta, \phi)$ with $\ell = 1, 2, ...,$ $m = -\ell, -\ell{+}1, ..., \ell{-}1, \ell$ (or two-dimensional Fourier transform in case the flat sky approximation is valid,) we transform the map data into a power spectrum, and obtain physical parameters from the fit to the power spectrum. For example, the temperature anisotropy is described in this way as

$$\Delta T(\hat{n}) = \sum_{\ell=1}^{\infty} \sum_{m=-ell}^{\ell} a_{\ell m} Y_\ell^m(\hat{n}). \tag{38}$$

Here, $\hat{n}$ represents the points on the sphere, $\Delta T(\hat{n}) \equiv T(\hat{n}) - T_0$ is the temperature anisotropy at each point of the sky with T_0 as the average sky temperature, and $a_{\ell m}$ is the amplitude

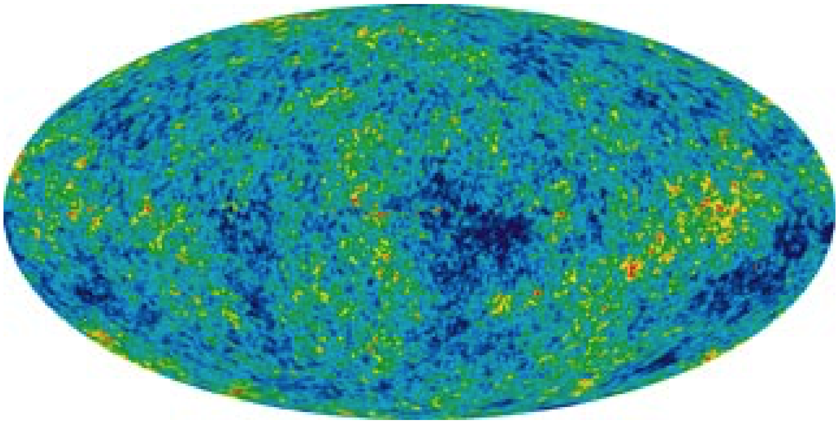

Figure 4: CMB map with WMAP. Measurements with different frequencies are combined in a weighted average to minimize the Galactic foreground contribution. The image by NASA [11].

of the corresponding spherical harmonic. From this decomposition, the power spectrum can be calculated as follows,

$$C_\ell = \frac{1}{2\ell+1}\sum_{m=-l}^{l} a_{\ell m}a^*_{\ell m}. \tag{39}$$

The factor $a_{\ell m}$ depends on the choice of the coordinate origin, but C_ℓ is independent of the coordinate system. By comparing the power spectrum shape with the theoretical curve of ΛCDM, we can extract information on cosmological parameters such as the mass density of baryons and cold dark matter.

Observing large ℓs requires a small angular resolution, and observing small ℓs requires large-angle scans. C_ℓ is measured as

$$\langle a_{\ell m}a^*_{\ell' m'}\rangle = \frac{1}{4\pi}\int d^2(\hat{n})d^2(\hat{n}')P_\ell(\hat{n}\cdot\hat{n}')\langle\Delta T(\hat{n})\Delta T(\hat{n}')\rangle \tag{40}$$

Since the CMB temperature fluctuations are thought to be caused by quantum fluctuations in a quantum field with almost no interaction, the distribution is expected to be approximately Gaussian. For ΔT that follows a Gaussian distribution, there is only one universe that we can observe, and what we can observe is the average over m in one universe. The difference between the C_ℓ we want to observe and the C_ℓ^{obs} we can actually observe arises from this fundamental limitation, which is called the "cosmic variance." Here C_ℓ^{obs} is written as

$$C_\ell^{obs} = \frac{1}{4\pi}\int d^2(\hat{n})d^2(\hat{n}')P_\ell(\hat{n}\cdot\hat{n}')\Delta T(\hat{n})\Delta T(\hat{n}') \tag{41}$$

In the case when C_ℓ^{obs} is measured for all ℓs in the range $\Delta\ell$ where C_ℓ is almost unchanged, the cosmic variance is reduced by $\propto \frac{1}{\sqrt{\Delta\ell}}$, and we expect

$$\langle\Delta C_\ell^2\rangle = \langle\Big(\frac{C_\ell - C_\ell^{\mathrm{obs}}}{C_\ell}\Big)^2\rangle = \frac{2}{2\ell+1}. \tag{42}$$

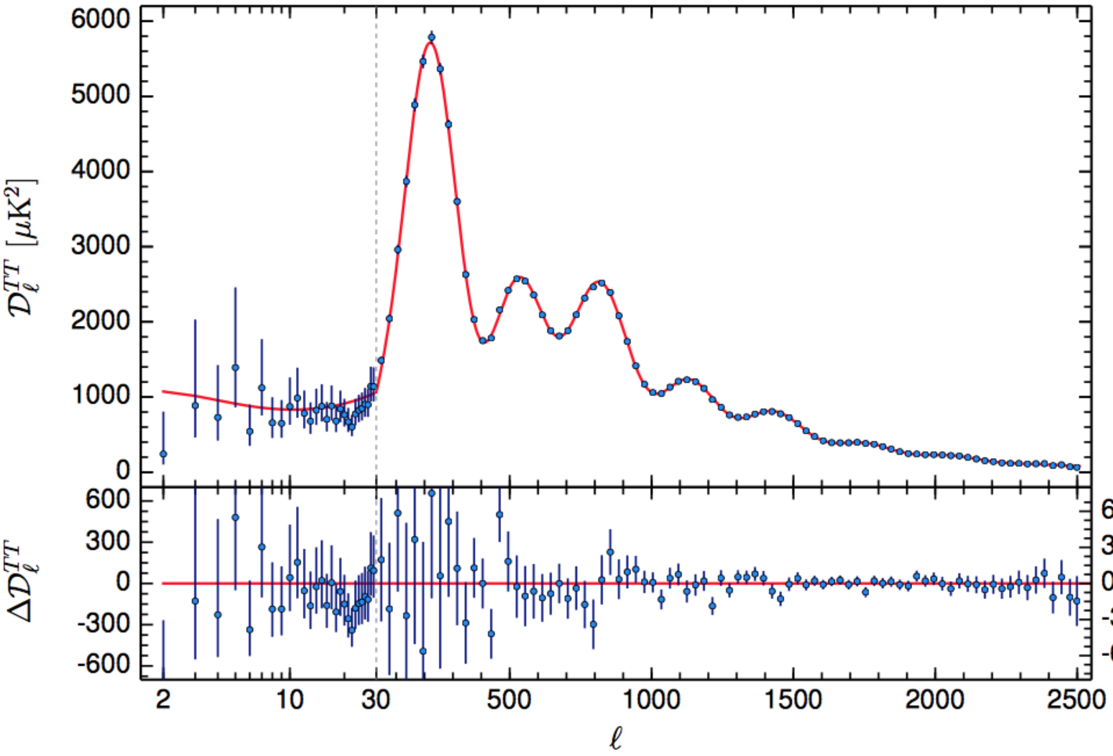

Figure 5: CMB temperature anisotropy power spectrum measurements by Plank satellite (2015). Power spectra are often presented as $D_\ell = \ell(\ell+1)C_\ell/2$. Theoretical curve (solid line) and observation (points with error bars) are in good agreement [12].

This expressions can be extended for the cases with partial sky observations. We define $f_{\rm sky}$ as the measured sky fraction, i.e. the ratio between the measured sky area and the entire celestial sphere ranging from 0 to 1. With the higher $f_{\rm sky}$ observed, the uncertainty in the C_ℓ estimation is reduced because more modes are averaged. Quantitatively, we can write

$$\Delta C_\ell \approx \sqrt{\frac{2}{(2\ell+1)f_{\rm sky}}}C_\ell. \tag{43}$$

1.3.1 CMB polarization

The CMB polarization is generated by Thomson scattering when quadrupole temperature anisotropies exist as illustrated in Fig. 6. Polarized light is produced when an incident photon from a specific direction is scattered by an electron. However, since there is no particular direction in the universe, light can come to an electron from any direction. For example, if the incident light's intensity is equal from any direction, the scattered light on average will be unpolarized. However, suppose there is a quadrupole temperature anisotropy in a stationary electron system. In that case, the intensity of the incident unpolarized light is not equal. The scattered light will have non-zero polarization.

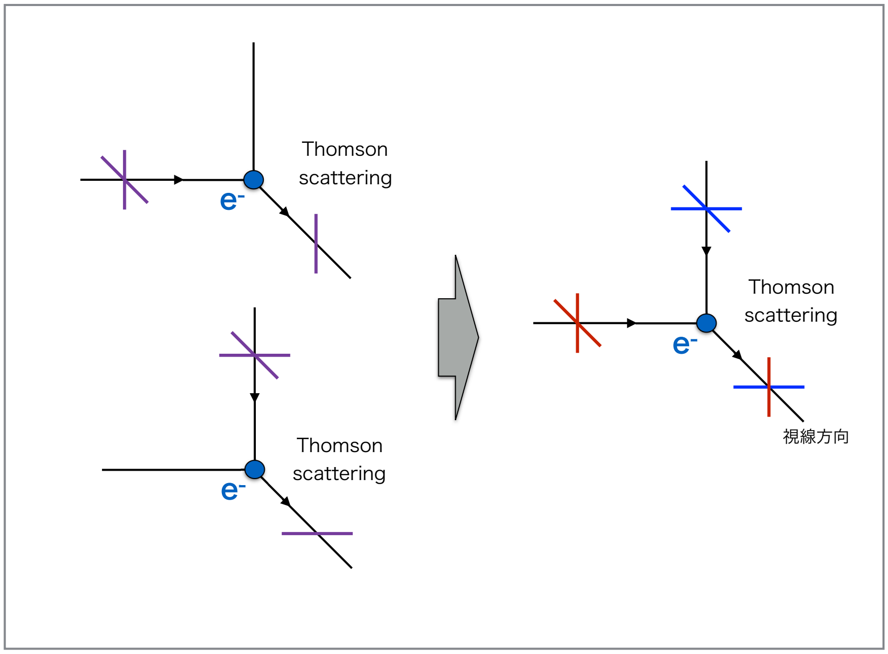

Figure 6: Thomson scattering and photon polarization are illustrated. When the photon distribution has a quadrupole anisotropy, the net polarization is non-zero [13].

We use Stokes parameters to parametrize the measured polarized field. The Stokes parameters characterize polarized intensities as I, Q, U, V. With the electric field amplitudes E_x, E_y, and the phase difference ϕ, Stokes parameters are given by

$$\begin{bmatrix} I \\ Q \\ U \\ V \end{bmatrix} = \begin{bmatrix} \langle E_x^2 + E_y^2 \rangle \\ \langle E_x^2 - E_y^2 \rangle \\ \langle 2E_xE_y \cos\phi \rangle \\ \langle 2E_xE_y \sin\phi \rangle \end{bmatrix}$$

. Thomson scattering generates linear polarization. Then, the Stokes parameter V can be ignored here because it represents circular polarization. The Stokes parameter I is the intensity of un-polarized component, and Q and U show linear polarization. When the coordinate system is rotated counterclockwise by an arbitrary angle φ, Q and U are transformed as

$$\begin{bmatrix} \tilde{Q} \\ \tilde{U} \end{bmatrix} = \begin{bmatrix} \cos 2\varphi & \sin 2\varphi \\ -\sin 2\varphi & \cos 2\varphi \end{bmatrix} = \begin{bmatrix} Q \\ U \end{bmatrix}. \tag{44}$$

If we introduce $Q \pm iU$ using the imaginary number i, we obtain the following compact form,

$$(Q \pm iU)(\hat{n}) = e^{\mp 2i\psi}(Q \pm iU)(\hat{n}). \tag{45}$$

Using the spin-2 spherical harmonics, we also obtain the following expression,

$$(Q \pm iU)(\hat{n}) = -\sum_{\ell m}(a_{E,\ell m} \pm i a_{B,\ell m})_{\pm 2}Y_{\ell m}(\hat{n}). \tag{46}$$

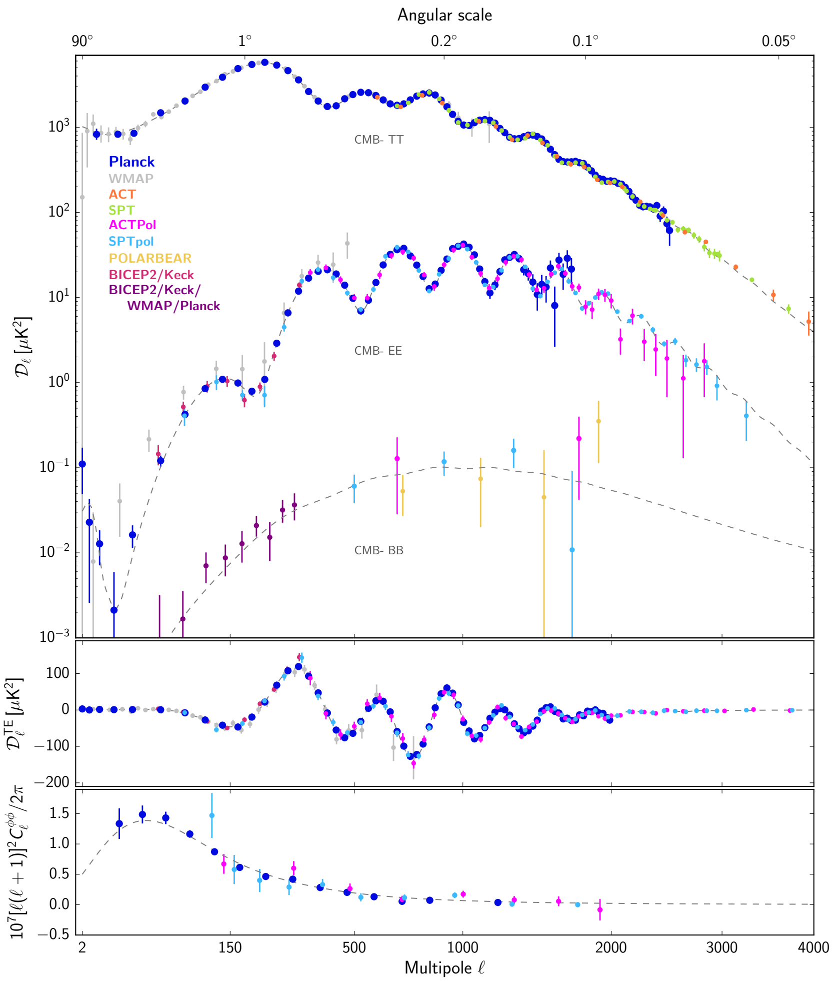

Figure 7: The power spectra of the temperature anisotropy, the E-mode, and the B-mode of the CMB. The upper line is the temperature anisotropy, the middle line is the E-mode, and the bottom line is the lensing B-mode (top). The cross-correlation spectrum between the temperature anisotropy and the E-mode of the CMB (middle). The lensing deflection power spectrum (bottom) [14].

1.4 Foregrounds observation

The B-mode spectrum is actually made more difficult to observe by foreground radiation. Therefore, accurate removal of these foreground emissions is essential for the precise measurement of B-modes. The primary foreground radiation is polarized radiation from galaxies. Dust particles are a source of polarized radiation. The interstellar medium (ISM) in galaxies contains fine dust particles that absorb thermal radiation. This dust causes polarized radiation with a frequency close to the peak frequency of the CMB. There is also radiation in the Milky Way, synchrotron radiation, generated by relativistic charged particles being accelerated radially around magnetic field lines in the galaxy's magnetic field. The magnetic fields of galaxies are not entirely understood, but they emit polarized light in MHz–GHz region. Finally, the Earth's atmosphere (clouds) is also known to emit polarized radiation. For example, ice crystals in tropospheric clouds scatter thermal radiation. Pseudo-polarization from the atmosphere during CMB observations has been shown to be correlated with the amount of cloud [15].

Since these foreground radiation signals have a different frequency dependence compared to the CMB, as shown in Fig. 8, the effect can be reduced by observing them at multiple frequencies. In other words, observation over multiple frequencies effectively removes the foreground radiation.

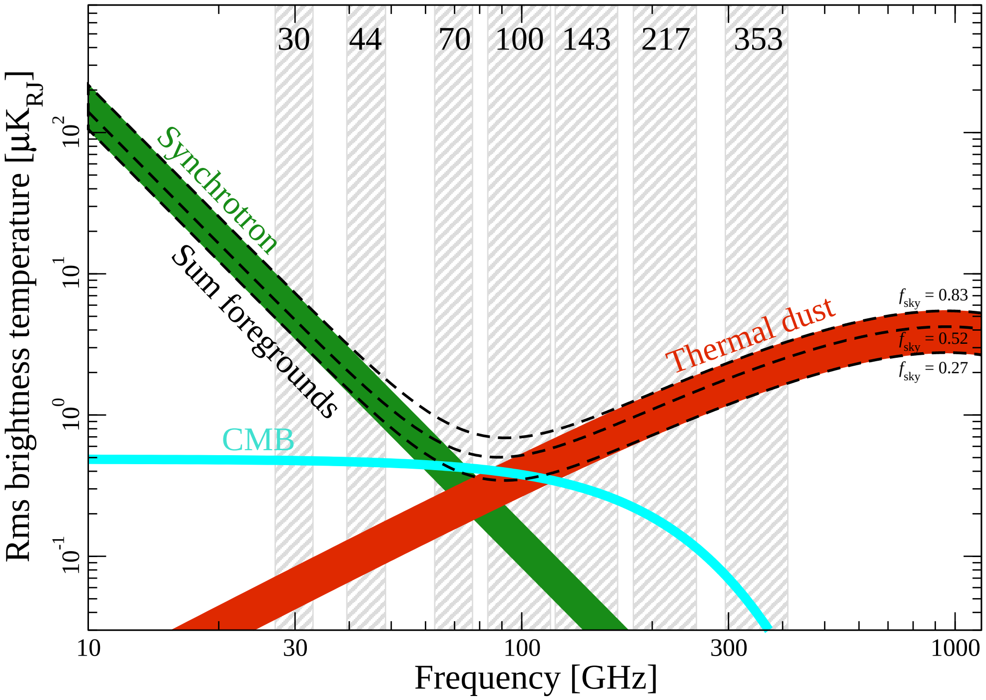

Figure 8: Spectral dependences of polarized foreground emission. Figure shows the RMS amplitude of polarization signal at high galactic latitude. The green band indicates polarized synchrotron emission, and the red band indicates polarized thermal dust emission. The cyan curve shows the CMB rms for a ΛCDM model with τ=0.05 [16].

1.5 Current CMB experiments

Observation of polarization B-mode has the best promise to detect primordial gravity waves at large angular scales. Weak gravitational lensing is effective for observing B-mode polarization on small angle scales. Many CMB experiments aim at observing the B-mode and E-mode polarization. Current CMB experiments can be broadly divided into ground-based, balloon, and satellite experiments. Table 2 summarizes projects in operation or in preparation. Fig. 10 shows measurements so far carried out. The advantage of ground-based experiments, including POLARBEAR, is that the number of detectors can be increased by enlarging the equipment, and thus the statistical sensitivity can be increased. However, it is necessary to take measures against the noise from the atmosphere. In the ground-based experiments, we cannot ignore the influence of the absorption of millimeter waves by water vapor and oxygen in the atmosphere. Therefore, dry and high-altitude Atacama Highlands in Chile and Antarctica are mainly chosen as observation sites to minimize the influence of the atmosphere. The Atacama Highlands near the equator have a broader sky coverage. Since the radiant heat of the atmosphere is frequency-dependent, observations are made in the frequency band called the millimeter-wave atmospheric window, which is less affected by millimeter-wave absorption. The observation frequencies chosen for the POLARBEAR-2, for example, are around 90 and 150 GHz, which are the frequencies of the three atmospheric windows between 60–300 GHz. Fig. 9 shows spectral dependences of the transmission and brightness temperature of the atmosphere from the Chajnantor plateau in Chile, showing the atmospheric windows.

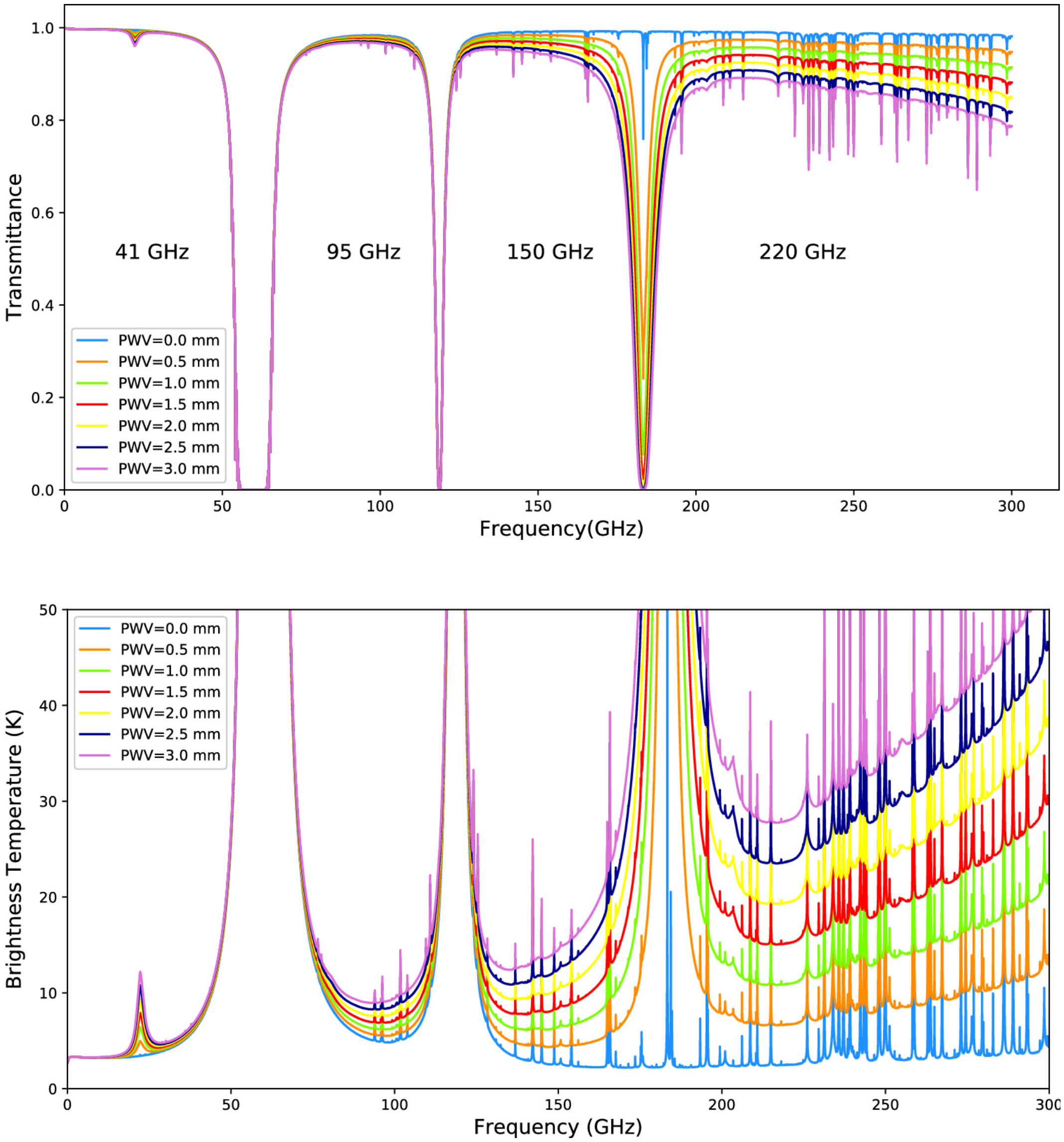

Figure 9: Spectral dependences of transmission and Brightness temperature of the atmosphere from the Chajnantor plateau. We chose the observing frequency bands on the atomosphic window which is less effect by absorbing [17].

1.6 Future ground-based CMB experiments

Ground-based CMB polarization experiments are categorized into "stages." Stage-2 CMB experiments were deployed around 2012 and typically had O(1,000) detectors. These experiments (e.g., POLARBEAR-1, ACT-Pol, SPT-Pol, BICEP-2) discovered B-modes at ℓ = 100–2,000, from the weak gravitational lensing effect. On the other hand, as of the end of 2021, no experiment found significant B-mode signals in $\ell < 100$. Therefore, only the upper limit is set to the tensor-to-scalar ratio r. The most stringent limit is $r < 0.032$ [8].

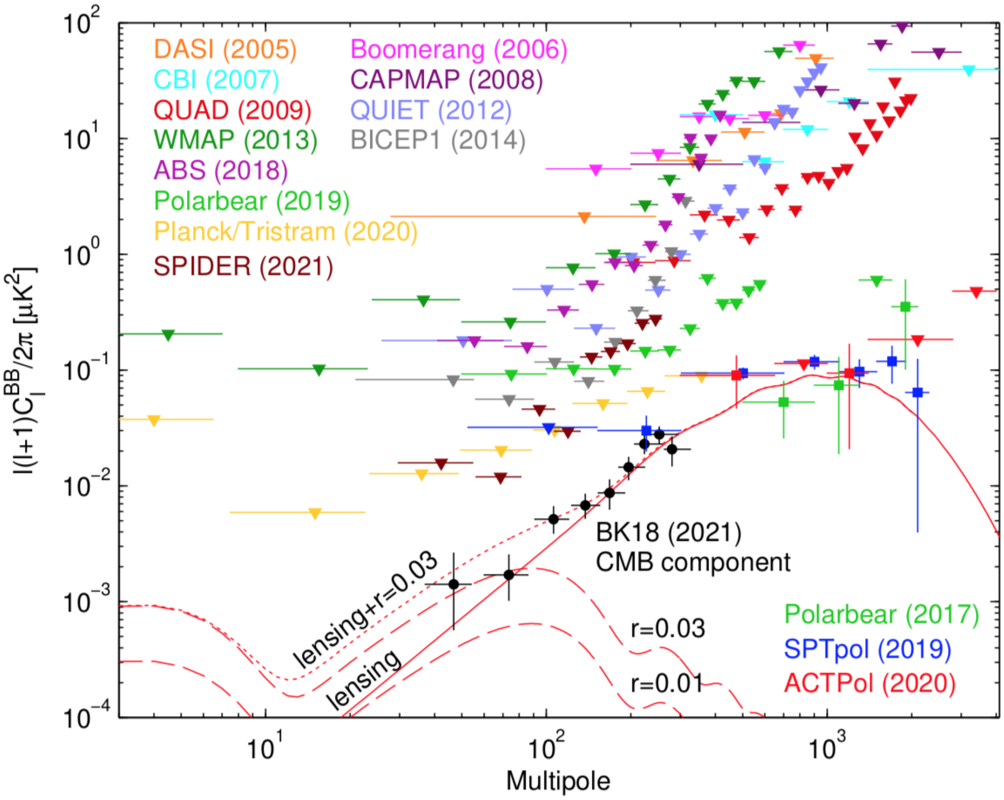

Figure 10: Measurements of CMB B-mode so far carried out [18].

Stage-3 CMB experiments (e.g., BICEP-3, Simons Array (SA), South Pole Telescope Third Generation (SPT-3G), and Advanced Atacama Cosmology Telescope (AdvACT)) have deployed with $\sim$ 10,000 detectors. SA is the next stage experiment of POLARBEAR-1. Upon completion of deployment of all three receivers, it will have 22,000 detectors at four different frequencies (90, 150, 220, 270 GHz) for the foreground separation. The SA's goal is to measure tensor-to-scale ratio to $\sigma(r) \sim 0.006$ to detect or rule out the majority of the single field slow-roll inflation models. SA is also designed to precisely measure the lensing B-modes at a level of $\sigma(\sum m_\nu) \sim 40\,\text{meV}$ (68% CL), assuming that the parameter degeneracy is mitigated with future optical surveys as DESI. As a next-generation Stage-4 CMB experiment, CMB-S4 is being planned to deploy in the end of 2020s. CMB-S4's goal is $\sigma(r) \sim 10^{-3}$ and $\sigma(\sum m_\nu) \sim 15\,\text{meV}$ (68% CL). Groups at two major CMB observatory sites are already getting together into two advanced observatories, which can be viewed as an intermediate step toward CMB-S4. One is the Simons Observatory (SO), formed by SA and AdvACT collaborations, and is coming together to deploy new telescopes in the Atacama desert, Chile. Another one is the South Pole Observatory (SPO), led by BICEP-3 and SPT-3G teams in the South Pole. The timing of both projects is adjusted with CMB-S4, providing insight into technologies and operations for CMB-S4.

type	advantage	disadvantage	project
ground	possibility of enlarging the equipment and increasing the number of detectors (the statistical sensitivity)	the noise from the atmosphere. limited sky coverage	POLARBEAR, GroundBIRD, ACT-pol, Keck array, BICEP3, SPTpol, Simons Observatory *, CMB-S4 * etc.
balloon	reduced the noise from the atmosphere. multi-frequency observation bands	limited observation time	EBEX, SPIDER, PIPER etc.
satellite	no noise from the atmosphere, multi-frequency observation bands, a larger sky coverage	Cost and time. No equipment upgrade after launch.	Plank, LiteBIRD *, PICO *

Table 2: Current and future CMB experiments. Future experiments are tagged with ‘ * .’

2 The POLARBEAR-2 Experiment

2.1 Science goals of the POLARBEAR-2 experiment

POLARBEAR-2 (PB-2) is a ground-based CMB polarimetry experiment for observing a wide range of power spectrum of CMB($30 < \ell < 2500$) (Fig. 11). The PB-2 aims to detect the B-mode polarization pattern from the inflationary primordial gravitational waves at large angular scales. The strength of the primordial gravitational wave is indicated by the tensor-to-scalar-ratio r, and the PB-2 plans to measure $r = 0.01$ (68% C.L.), which we denotes $\sigma(r) = 0.01$. With the measurement of weak gravitational lensing B-modes at small angler scales, PB-2 would constraint the sum of neutrino masses to 90 meV (68% C.L.) and 65 meV (68% C.L.) combined with Planck data [12]. In the future, the goal of the Simons Array experiment, which deploys three PB-2-type receivers, is to measure the tensor-to-scalar ratio to $\sigma(r) \sim 0.006$. Another goal is to measure the weak gravitational lensing B-modes precisely at a level of 40 meV (68% C.L.) with future optical surveys such as the Dark Energy Spectroscopic Instrument (DESI).

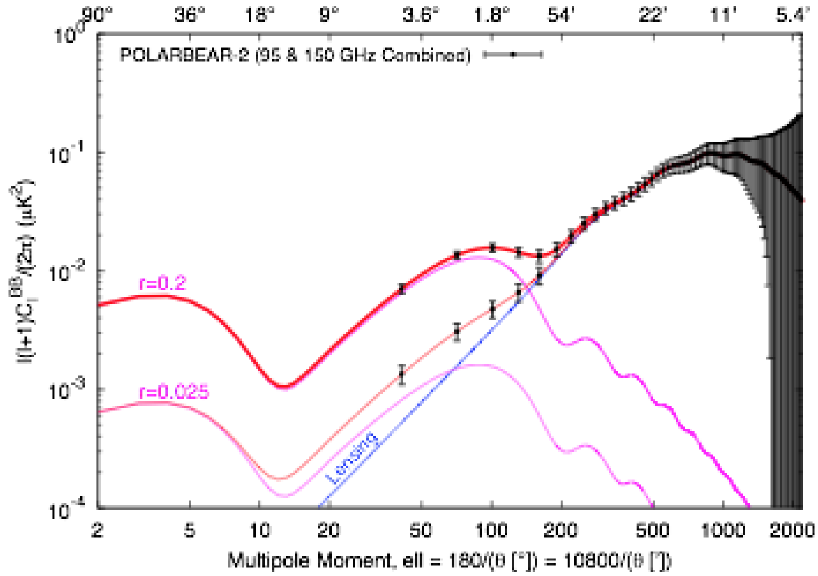

Figure 11: The expected sensitivity of POLARBEAR-2 with three-year observations. The thick (thin) line is the spectrum of B-mode originating from primordial gravity waves with $r = 0.2$ (0.025). POLARBEAR-2 is sensitive to both B-modes from primordial gravitational waves and the gravitational weak lensing effect because it observes a wide range of power spectrum ($30 < \ell < 2500$) [19].

The telescope is locate at the James Ax Observatory at an altitude of 5,200 meters on the Mt. Cerro Toco site in the Atacama Desert, Northern Chile (West longitude 67°47′10.40″, South latitude 22°57′29.03″). The Atacama Desert is dry, and precipitable water vapor (PWV) is usually quite low, around 1.0-1.5 mm. For a millimeter-wave observation like the PB-2, high attitude and low PWV are advantageous because water molecules' absorption (Fig. 9) and the thermal emittance add less optical loading on the receiver.

The gradual variations of the optical loading introduce the noise in the low-frequency region ($1/f$ noise). Also, there are benefits of stable weather, a large observable sky coverage, and relatively easy access to the site in this location. Chilean site's mid-latitude location enables us to observe a large sky area of $f_{\mathrm{sky}} > 70\%$, while it is typically $f_{\mathrm{sky}} = 20\%$ at the South Pole. In addition, in Atacama, sky rotation during each observation reduces instrumental systematic errors in polarization measurements, which is not the case at the South Pole. There are currently many other millimeter and sub-millimeter observations in the Atacama Desert (Fig. 12) : the Atacama Cosmology Telescope (ACT) [20]; Cosmology Large Angular Scale Surveyor (CLASS) [21]; Atacama Large Millimeter/sub-millimeter Array (ALMA); Atacama Pathfinder Experiment (APEX) [22].

Figure 12: The Chilean site and the Simons Array telescope. The photo by Debra Kellner.

2.2 The Simons Array telescope

In December 2018, the PB-2 receiver was mounted on a Nicholas Simons Telescope, the Norce telescope of the Simons Array, which has the same design as the Huan Tran Telescope (HTT) for POLARBEAR-1 (PB-1) (Fig. 13). The telescope has a parabolic primary mirror and the elliptical secondary mirror, forming an off-axis reflective Gregorian system. This optical system satisfies the Mizuguchi-Dragone condition [23]. In the Mizuguchi-Dragone condition, two mirrors act as an equivalent on-axis parabolic reflective system. This can suppress the polarization caused by mirror reflection. This optical design can have a large diffraction-limited field of view (FOV). The FOV of the PB-2 is designed to be 4.8 degrees in diameter, and the PB-2 has low side-lobes and low cross-polarization. The prime focus image between the primary and secondary is re-imaged at the Gregorian focus in the receiver.

The illumination pattern to the primary reflector is 2.5 meters. The reflector material is aluminum, with its surface machined to an accuracy of 53 μm RMS. The guard ring panels surround the primary mirror, and the overall diameter is 3.5 meters. The sky resolution is 3.5 arcminutes full width at half maximum (FWHM) at 150 GHz and 5.2 arcminutes FWHM at 90 GHz. The secondary mirror is 1.4-meter diameter, made of aluminum, with a baffling enclosure, blocking reflected light on the ground. The telescope can move both azimuth and elevation direction during the observation.

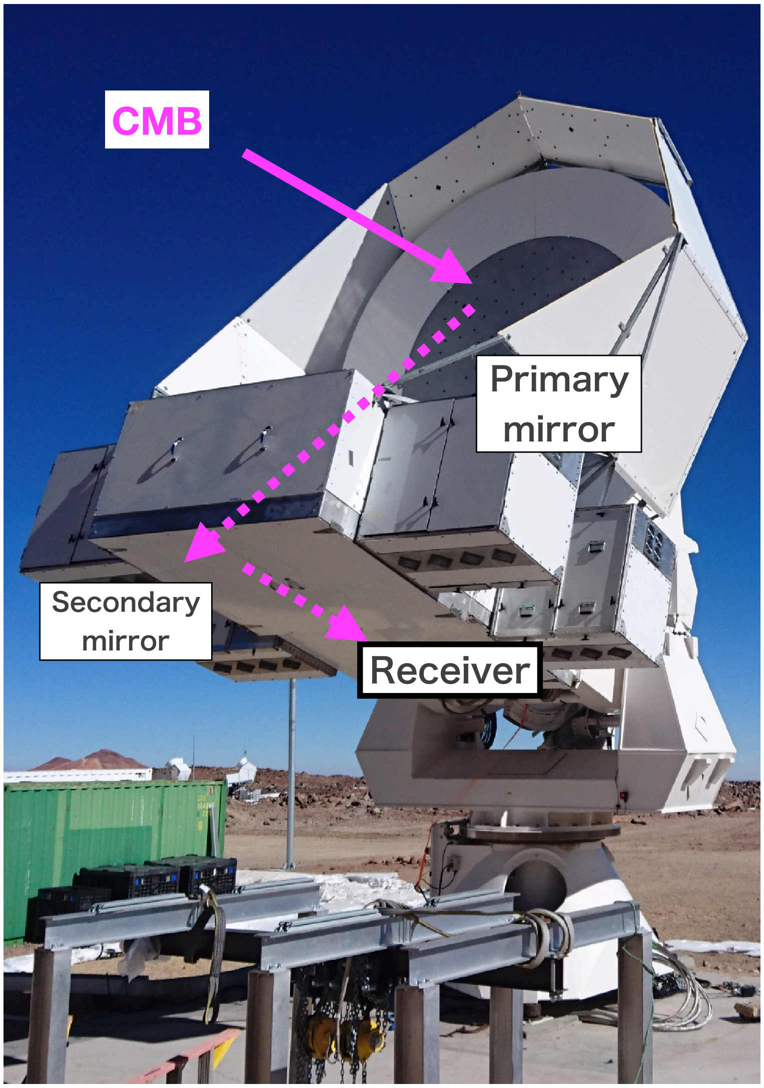

Figure 13: The Nicholas Simons Telescope, the Norce telescope of the Simons Array. The light of the CMB is incident on the receiver by the primary and the secondary mirrors.

2.3 POLARBEAR-2 receiver

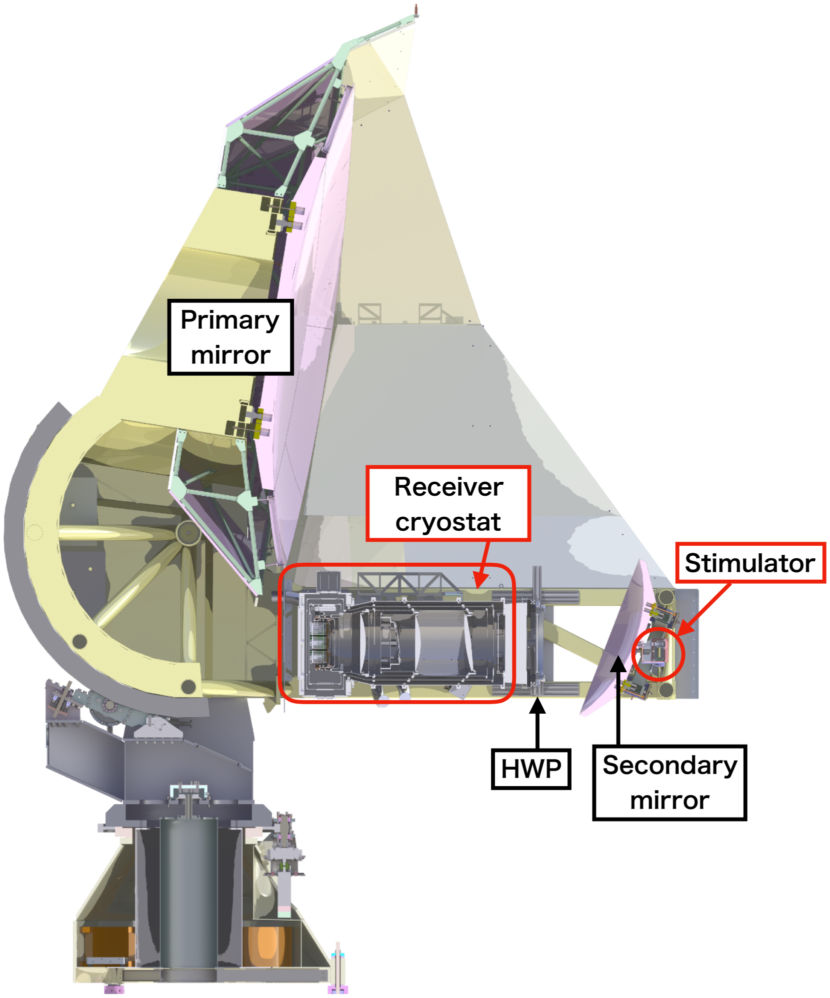

Figure 14: The cross-sectional view of the CAD drawing of the Simons Array.

The PB-2 receiver is installed on the telescope as shown in Fig. 14. The PB-2 receiver is 1.9 meters long, 1.2 meters wide, and 0.88 meters high (Fig. 15). The term "receiver" here refers to the entire system, including the bolometers and optical system that receives the incoming CMB radiation. The PB-2 receiver is an extensive cryogenic optical system. All the components of the optical system in the receiver are cryogenically cooled to reduce the thermal loading. The PB-2 receiver is designed to suppress parasitic photons with absorption on the inner surface.

Three "shells", a 4 K shell, a 50 K shell which is cooled by pulse tube coolers (PTCs) [24], and a 300 K shell, surround the bolometers and the optical system. Another important role of the 300 K shell, the outermost part of the PB-2 receiver, is to maintain a vacuum. In addition, two vacuum extraction ports are provided to allow an efficient transition to a high vacuum state (Fig. 16).

The PB-2 receiver has three cryogenic lenses to refocus the Gregorian focus onto the focal plane tower. More details on the lenses are explained in Sec. 2.3.1.

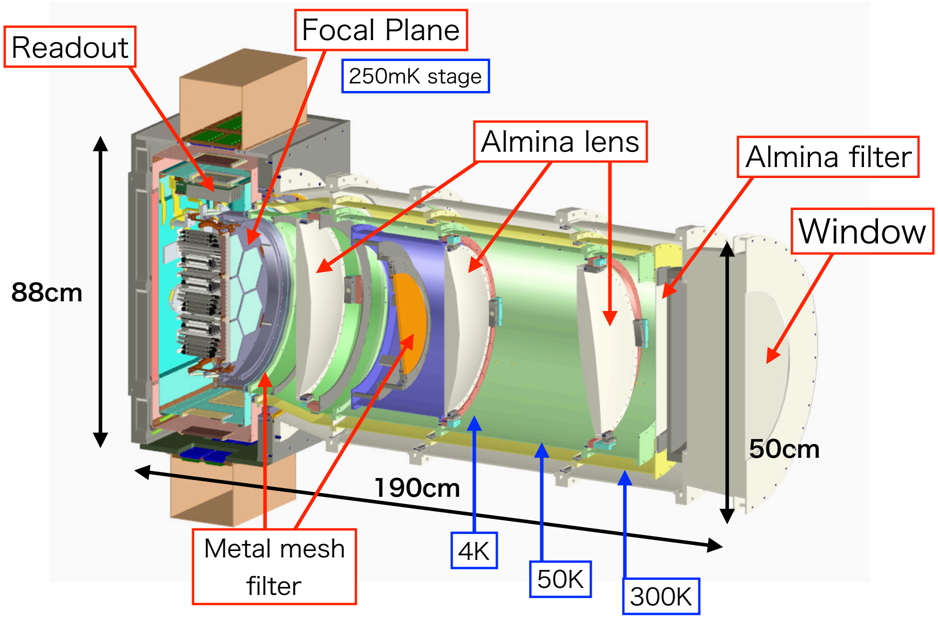

Figure 15: The PB-2 receiver overview. The PB-2 receiver has three cooled alumina lenses, focusing light onto the focal plane tower. The receiver consists of a 4 K shell, a 50 K shell which is cryogenically cooled by PTCs, and a 300K shell that also maintains the vacuum.

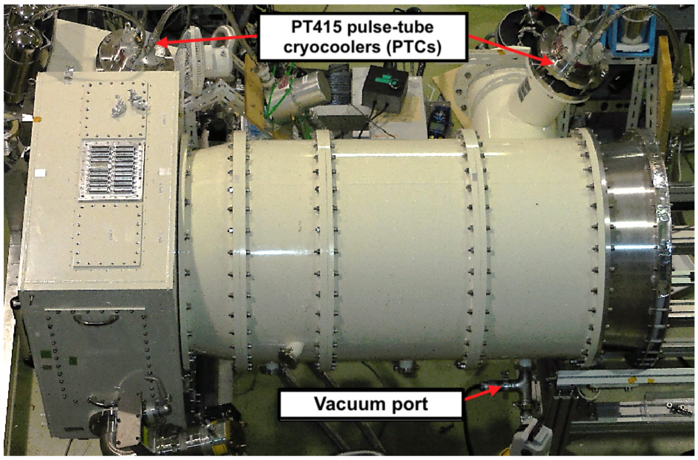

Figure 16: Photograph of the receiver viewed from above. The receiver's 50 K and 4 K shells are cooled by two pulse-tube cryocoolers . There is another vacuum port on the other side.

It is necessary to insulate each temperature stage thermally, but at the same time, it is needed to provide a rigid support to reduce unwanted vibration-induced heating. The PB-2 receiver uses G-10 as a support material between 300 K and 50 K and between 50 K and 4 K. In addition, Vespel [25], which has a lower thermal conductivity, is used for the support mechanism at cryogenic temperatures [26].

	POLARBEAR-1	POLARBEAR-2
observation frequency	150 GHz	90 GHz,150 GHz
number of bolometers (pixels)	1274 (637 pixels)	7588 (1897 pixels)
$\mathrm{NET_{bolo}}$	$480\,\mu\mathrm{K}\sqrt{\mathrm{s}}$	$360/360\,\mu\mathrm{K}\sqrt{\mathrm{s}}$ (90/150 GHz)
$\mathrm{NET_{array}}$	$23\,\mu\mathrm{K}\sqrt{\mathrm{s}}$	$5.6/5.6\,\mu\mathrm{K}\sqrt{\mathrm{s}}$ (90/150 GHz) $4.0\,\mu\mathrm{K}\sqrt{\mathrm{s}}$ (90 + 150 GHz)
FOV	2.4°	4.8°
FWHM	3.5 arcmin	5.2 / 3.5 arcmin (90/150 GHz)
sky coverage	1.7%	65%
observation time	5 year	3 year

Table 3: Specifications of PB-1 and PB-2. The number of pixels is the same as the number of antennas [27].

2.3.1 Optics

Zotefoam (HD-30) [28] is used as the optical window of the PB-2 receiver. The diameter of Zotefoam window is 500 mm, and thickness is 200 mm. Zotefoam has high transmittance in the observed frequency bands and high absorption in the infrared radiation band. The typical temperature of the vacuum side of Zotefoam is 252 K, and the transmittance is measured to be 98% in the 150 GHz observation frequency band. It is capable of transmitting millimeter waves while maintaining a vacuum. Zotefoam has also been used in SPT, EBEX, and PB-1 experiments. Inside the optical window is about 50 layers of thin Radio-Transparent Multi-Layer Insulation (RT-MLI) made of materials that transmit the observed frequency bands and reflect infrared radiation [29].

Alumina transmits the observed frequency bands and blocks the infrared radiation. The PB-2 puts an alumina filter on 4 K stage as an infrared filter. The alumina filter in 430 mm diameter is placed in the aperture to stop the 200 K infrared radiation from the RT-MLI and the 300 K shell to reduce the heat load on the 4 K shell. The PB-2 uses three re-imaging lenses made of 99.9% high purity alumina (aluminum oxide Al_2O_3) with low loss and high thermal conductivity (Fig. 17). The alumina lenses have a high dielectric constant to achieve a high refractive index ($n \approx 3.1$) [27], a large FOV, and a high Strehl ratio [30]. Three lenses are called, from the sky side to the focal plane side, a field lens, an aperture lens, and a collimator lens (Fig. 15). High-purity alumina requires an anti-reflection (AR) coating to reduce reflections on the surface. We adopted two different AR coating techniques. The curved surface has an epoxy AR coating, while the flat surface uses Mullite and Skybond foam [31]. As a result, both sides of the field lens have an epoxy AR coating, while the aperture lens and collimator lens have a hybrid configuration with both AR coating techniques to reduce fringe dips as shown in Fig. 18.

The PB-2 receiver includes a Metal Mesh Filter (MMF) and a Lyot stop. The MMF is a filter whose structure consists of fine holes drilled in metal. The cutoff frequency can be freely varied by controlling the holes' diameter because it is difficult for light to penetrate holes thinner than its wavelength. An alternating layer of polyethylene and metal mesh acts as a low-pass filter for the incident light; the cutoff frequencies of the MMF are 171 GHz (5.7 icm), 261 GHz (8.7 icm), and 360 GHz (12 icm) [27]. The MMF is incorporated both at the cold aperture stop (T $\sim$ 4 K) and just before the detector array (T $\sim$ 0.3 K).

The Lyot stop is an essential component to adjust the beam aperture. The Lyot stop uses KEK black [27] as the absorber material on the surface to block unexpected stray light.

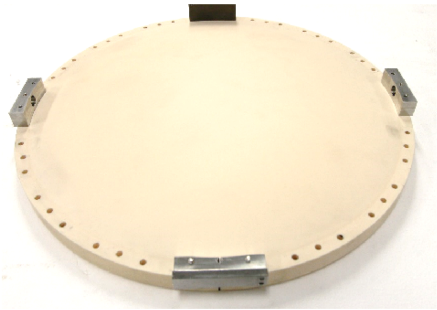

Figure 17: Alumina lens before anti-reflection coating. The lens is made of alumina with a purity of 99.9% and a refractive index of $n \approx 3.1$ [32].

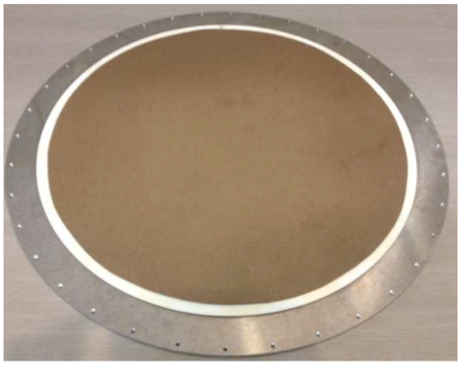

Figure 18: Alumina filter with an anti-reflective coating. It is about 460 mm in diameter and 2 mm thick, and is made of 99.9% pure alumina [31].

2.3.2 Cryogenic system

The PTCs used in the PB-2 are the two-stage PT415 model, available from Cryomech Inc. It is a closed-loop refrigeration system using compressed helium gas and is designed to have a cooling capacity of about 35 W (first stage) at 50 K and 1.5 W (second stage) at 4 K. Both PTCs are mounted on the receiver at a 21-degree tilt to work well when scanning at 45 degrees elevation angle of the telescope. Heat straps connect the shells to cool the various optical components inside the receiver, such as the lenses. Inner shells couple to the PTC thermally via a high-purity aluminum strip and a gold-plated copper interface (Fig. 19).

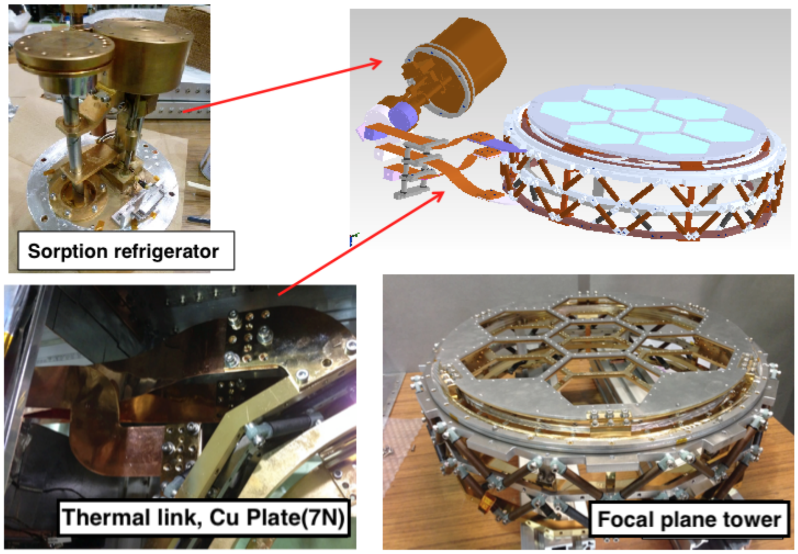

Figure 19: The bolometers mounted on the focal plane tower are cooled down to 0.3 K using a helium sorption cooler.

The PB-2 operates transition edge sensor (TES) bolometers at the superconducting transition point, around 450 mK. The focal plane tower is the most crucial temperature stage, and it is important to cool it. For cooling down to this temperature, a sorption refrigerator is used. This refrigerator is equipped with one He-4 pump and two He-3 pumps and cools the liquid helium using the characteristics of its vapor curve. The sorption refrigerator operates in a closed-cycle with a liquid He-4 and He-3 adsorption pump and requires periodic recycling. When the liquid helium in the refrigerator has evaporated completely, the temperature of the cryostat will rise, and then a new cycle will start again. Therefore, the operation of the TES bolometer must be synchronized with the cooling cycle of this refrigerator. The "hold time" is the time each cryogenic stage in the cryostat is at the target temperature and lasts only as long as the liquid He-3 remains and vaporizes. The cryostat refrigerator must be controlled to achieve the fastest cooling and the longest hold time. Repeating a standard 24-hours schedule requires 18 hours of hold time, which is 24 hours minus 6 hours. We satisfied the requirement as shown in Fig. 20.

Some readout electronics are sensitive to radio-frequency (RF) radiation interference. For this reason, the 4 K stage in the receiver back-end is designed to be fully shielded from RF interference.

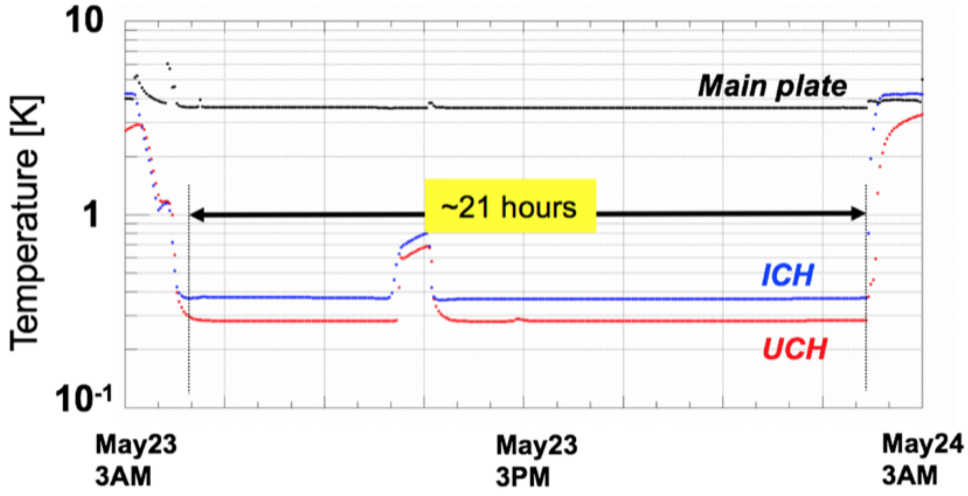

Figure 20: The hold time example. ICH and UCH are the temperatures of the Inter-Cooler head and the Ultra-Cooler head of the sorption refrigerator. The basic cycle repeats the 24-hour schedule with a hold time of 18 hours. This figure is courtesy of M. Hasegawa.

2.4 Half-wave plate

The PB-2 system is equipped with a continuously-rotating half-wave plate (HWP) in front of the receiver to modulate the linearly-polarized signal. The HWP is made of birefringent crystal, and the PB-2's HWP uses single-crystal sapphire, 3.6 mm thick [33]. Sapphire is one of the most typical birefringent material crystals. Due to the crystal structure of this material, the refractive index depends on the linear polarization state of the electromagnetic wave. The difference in the two orthogonal refractive indices creates a phase difference between the two orthogonal components of the incident electromagnetic wave. With this property, it is possible to modulate the incoming linearly-polarized light by rotating the crystal at an arbitrary speed. To modulate both 90 GHz and 150 GHz at PB-2, we stack three thin sapphire plates. AR coating is applied to both surfaces of the HWP to minimize thermal radiation from the adhesive layer. The rotation rate of the HWP is 2 Hz at PB-2. The HWP is mounted on a ball-bearing rotation stage and is driven via a belt connected to a servomotor.

Fluctuation of unpolarized thermal radiation from the atmosphere produces noise that grows at low frequencies ($1/f$ noise). Therefore, the effect of $1/f$ noise is unavoidable, especially in large angular scans, which are essential for measuring the B-modes derived from the primordial gravitational waves. However, by rotating the HWP, the polarization signal can be modulated to a higher frequency than the $1/f$ noise. By demodulation at a later stage, we obtain the signal only without $1/f$ noise. This method has already been demonstrated in practice in the PB-1 experiment [34]. Modulating the polarization signal from the sky by HWP makes it possible to scan large angular scales (below $\ell \sim 30$) without losing the polarization signal. For more detailed information about the HWP, here is a helpful reference [35].

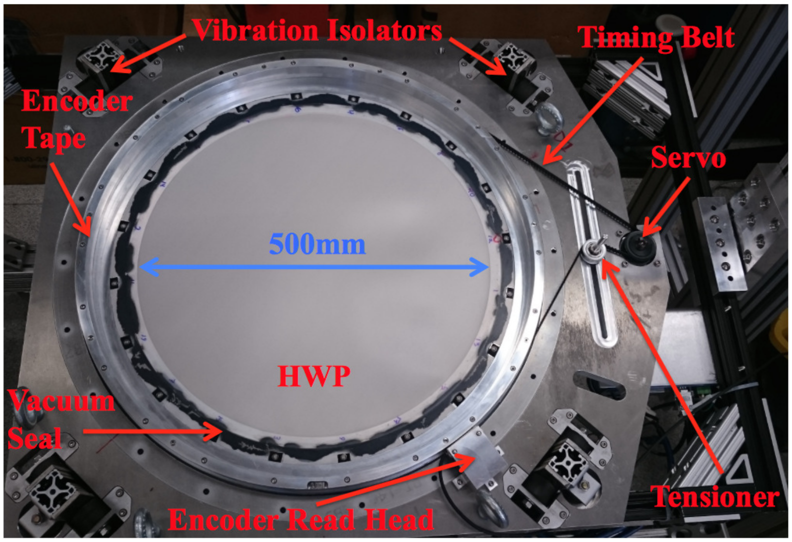

Figure 21: HWP overview. The HWP is developed at UC Berkeley. This figure is taken from C. A. Hill et al. (2016) [33].

2.5 Focal plane

In CMB experiments, semiconductor or superconducting bolometers have historically been used as detectors. Superconducting Transition Edge Sensor (TES) bolometers [36] are now used in most CMB experiments including the PB-2. TES bolometers can operate with sufficiently low noise that the measurement noise is limited by the photon noise of the incident optical signal, not by the detector's performance itself. Therefore, it is necessary to increase the number of bolometers to improve the overall sensitivity of the experiment. The PB-2 has a total of 7,588 TES bolometers. Multiplexing of the readout system is also an essential technique for CMB experiments requiring many detectors to improve sensitivity. More details on the multiplexing are explained in Sec. 2.6.

The PB-2 focal plane has seven hexagonal wafers (Fig. 22). Each silicon wafer has 271 multi-chronic pixels, which is sensitive to two orthogonal linear polarizations (Fig. 23, Fig. 28). One pixel can observe at both 90 GHz and 150 GHz. Each pixel has a broad-band sinuous antenna [37] and four TES bolometers. The microstrip filters split the signals from the antenna into two observation bands, and each signal power is measured with two TES bolometers.

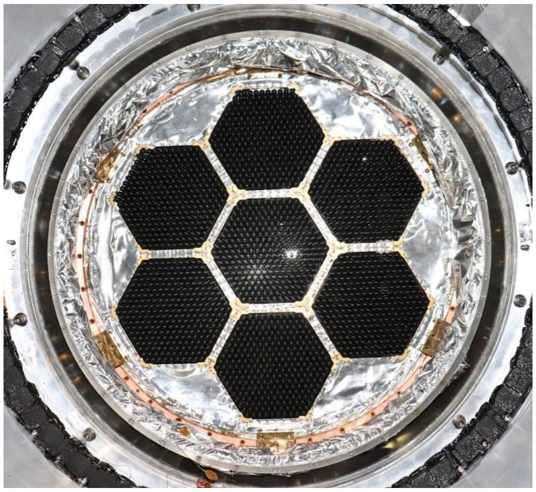

Figure 22: Focal plane detector array of the PB-2. Seven wafers are laid out in a honeycomb structure, with a total of 7× 271 pixels × 4 ch = 7588 TES bolometers.

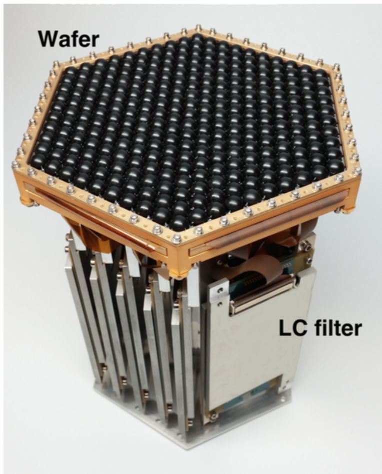

Figure 23: Detector module with 271 pixels, each covered with a hemispherical lenslet to focus the light on the sinuous antenna.

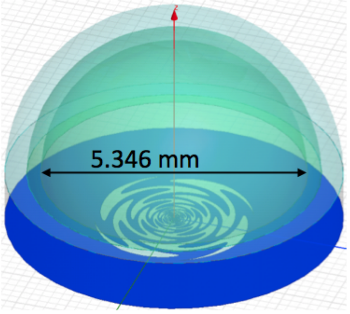

Figure 24: Lenslet and antenna, the shape of which is designed by simulation using HFSS [38] in order to efficiently focus the CMB light onto the antenna [37].

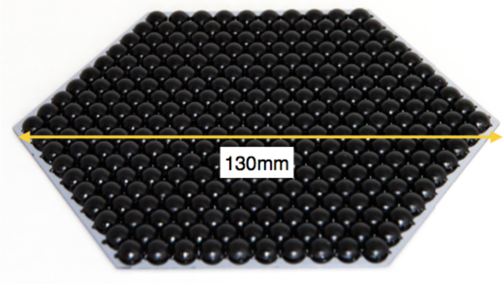

Figure 25: Detector wafer with 271 lenslets. Each lenslet has two layers of AR coating for both 90 GHz and 150 GHz [39].

2.5.1 TES bolometer

One of the advantages of TES bolometers is that they are suitable for voltage bias. That allows us to operate TES bolometers with a high loop gain, increasing uniformity across the array of bolometers and making them acceptable for multiplexing. Each bolometer in the multiplexer unit is channeled by an LC resonator with a unique resonant frequency. The resonator is placed behind the detector array (Fig. 23). The PB-2 bolometer was fabricated at the University of California, Berkeley. We can find details on the fabrication of the antennas and detectors in [40].

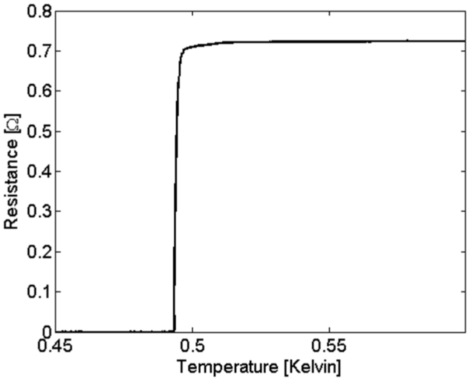

Figure 26: Transition edge of TES. The TES bolometer can measure small signals by using the property that the resistance of a superconducting absorber changes steeply between the superconducting and the normal states [36].

The TES bolometer can measure small signals by using the property that the resistance of a superconducting absorber changes steeply between the superconducting and the normal states (Fig. 26). Typically, a bolometer consists of a thin film of superconducting material, weakly connected to a thermal bath in which the thin film is maintained at temperature T_{bath} ($T_{\mathrm{bath}} <$ critical temperature T_{c}) (Fig. 27). The TES operates by heating the film around the superconducting transition temperature T_{c} with a voltage bias. The TES bolometer absorbs the electrical excitation caused by the signal at the antenna as thermal power through Joule heating. In this way, a slight change in the temperature of the TES causes a significant change in the resistance of the TES and the current driving it. Thus, a small signal from the incident light can be measured.

The antenna, filter, and TES bolometer are fabricated together on a 6-inch diameter silicon wafer using lithography techniques to reduce the inductance (Fig. 28). There are also "dark" bolometers in the focal plane that are not sensitive to light signals and are used for characterization and calibration purposes.

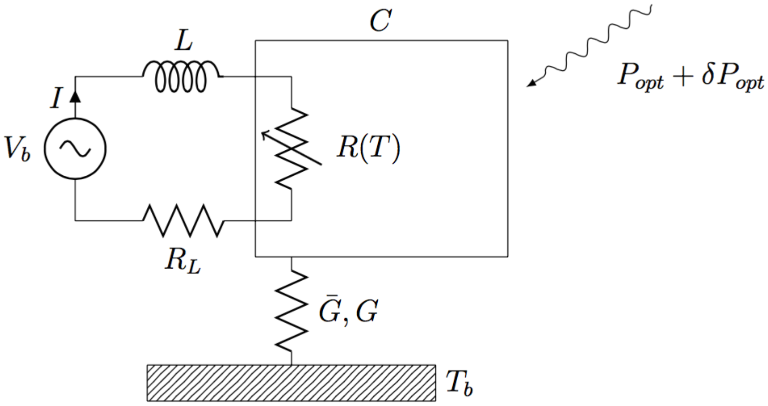

Figure 27: Simplified diagram of the TES bolometer. A TES bolometer is connected to a heat bath to maintain thermal stability. When heat flows into the TES bolometer from the antenna, the current through the circuit decreases to maintain the temperature. This change in current allows it to detect small signals. This figure is taken from [41].

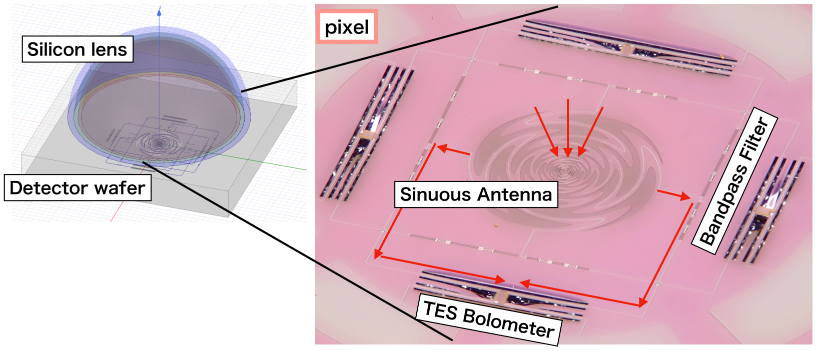

Figure 28: An image of a single pixel, showing an SEM image of sinuous antenna, TES bolometer and a CAD image of a lenslet.

2.5.2 TES operation

When the optical power P_{opt} changes slightly, the resistance $R_{\text{bolo}}(T)$ of the TES bolometer changes slightly around the constant voltage bias V_{bias}. The total power on the bolometer P_{total} is the sum of the bias power P_{elec} and the optical power from sky P_{opt} and written as,

$$P_{total} = P_{\text{opt}} + P_{\text{elec}} = P_{\text{opt}} + \frac{V_{\text{bias}}^2}{R_{\text{bolo}}} = G(T_{\text{bolo}} - T_{\text{bath}}) \tag{47}$$

Here, T_{bath} is the thermal bath temperature and G is a thermal link with conductivity.

Under constant voltage bias, temperature of the bolometer is stabilized by negative electrothermal feedback (ETF).

$$\frac{dP_{elec}}{dT_{\text{bolo}}} = -\frac{V_{\text{bias}}^2}{R_{\text{bolo}}^2}\frac{dR_{\text{bolo}}}{dT_{\text{bolo}}} = -P_{\text{elec}}\frac{1}{T_{\text{bolo}}}\frac{T_{\text{bolo}}}{R_{\text{bolo}}}\frac{dR_{\text{bolo}}}{dT_{\text{bolo}}} = -\frac{P_{\text{elec}}\alpha}{T_{\text{bolo}}}. \tag{48}$$

Here the slope of the superconducting transition is parametrized by

$$\alpha = \frac{T_{\text{bolo}}}{R_{\text{bolo}}}\frac{dR_{\text{bolo}}}{dT_{\text{bolo}}} = \frac{d\log(R_{\text{bolo}})}{d\log(T_{\text{bolo}})}. \tag{49}$$

The ETF keeps the total power constant and allows the system for stable operation. The ETF is parametrized by a loop gain $\mathcal{L} = P_{\text{elec}}\alpha/GT_{\text{bolo}}$, where $G = dP/dT$ is the differential thermal conductance between the bolometer at $\sim T_c$ and the thermal bath.

The system is linear for small signals and can use a single Fourier component for simplicity. Assuming time-varying perturbation with time at angular frequency ω, the perturbation of optical power can be $P_{\text{opt}} + \delta P_{\text{opt}}e^{i\omega t}$. Also, the temperature of bolometer can be $T_{\text{bolo}} = T_c + \delta T_{\text{bolo}}e^{i\omega t}$. Here, $\delta T_{\text{bolo}}e^{i\omega t} \ll T_{\text{c}}$ and fluctuations at different frequencies occur independently. Eq.(47) be written as,

$$P_{\text{opt}} + \delta P_{\text{opt}}e^{i\omega t} + P_{\text{elec}} - \frac{V_{\text{bias}}^2\alpha}{RT_{\text{bolo}}}\delta T_{\text{bolo}}e^{i\omega t} = \bar{G}(T_c - T_{\text{bath}}) + G\delta T_{\text{bolo}}e^{i\omega t} + i\omega C\delta T_{\text{bolo}}e^{i\omega t} \tag{50}$$

$$\delta P_{\text{opt}} = \left(\frac{V_{\text{bias}}^2\alpha}{RT_{\text{bolo}}} + G + i\omega C\right)\delta T_{\text{bolo}}, \tag{51}$$

where $\bar{G}$ is the average thermal conductance. The loop gain $\mathcal{L}(\omega)$ is,

$$\mathcal{L}(\omega) = -\frac{\delta P_{\text{elec}}}{\delta P_{total}} = \frac{P_{\text{elec}}\alpha}{GT_c(1+i\omega\tau_0)} = \frac{\mathcal{L}}{1+i\omega\tau_0} \tag{52}$$

Here, $\delta P_{\text{elec}} = -\frac{\delta P_{\text{elec}}\alpha}{T_{\text{c}}}\delta T$ is feedback. The bolometers change in current as the optical power change. We define the bolometer responsivity S_I [4] as,

$$S_I = \frac{dI_{\text{elec}}}{dP_{\text{opt}}} = \frac{\sqrt{2}}{V_{\text{bias}}}\frac{dP_{\text{elec}}}{dP_{\text{opt}}} = -\frac{\sqrt{2}}{V_{\text{bias}}}\frac{\mathcal{L}}{(1+\mathcal{L}+i\omega\tau_0)} = -\frac{\sqrt{2}}{V_{\text{bias}}}\frac{\mathcal{L}}{i\omega\tau_0(\mathcal{L}+1)} \tag{53}$$

The heat absorbed by the TES bolometer is released into the thermal bath with a thermal time constant τ_0. The bolometer's thermal time constant τ_0 is written as

$$\tau_0 = \frac{C}{G}. \tag{54}$$

Also the effective time constant τ of the bolometer is written as

$$\tau = \frac{C}{G(\mathcal{L}+1)} = \frac{\tau_0}{\mathcal{L}+1}. \tag{55}$$

If the bolometer operates in the high loop gain limit of $\mathcal{L} \gg 1$,

$$S_I \approx -\frac{\sqrt{2}}{V_{\text{bias}}}. \tag{56}$$

---

[4] The PB-2 uses an AC voltage bias, and V_{bias} is RMS here.

2.5.3 Readout parameters

The PB-2 bolometers are optimized for the 90 and 150 GHz observation bands, and the saturation power is optimized to match the expected optical power in these bands. Each observation band has a fractional bandwidth of about 30% [42].

The TES material is aluminum doped with about 4,000 ppm manganese, and the doping reduces the critical temperature to about 0.44 K relative to undoped aluminum (1.2 K). A thin film of titanium serves as the load resistor for the antenna, and a superconducting microstrip exchanges signals with the bolometer. A microstrip line made of niobium Ti is used here to reduce parasitic impedance. These have been designed to meet the requirements of the experiment (Table.4).

parameters	90 GHz	150 GHz
f_{center}	94.3 GHz	147.8 GHz
f_{BW}	30.6%	26.0%
Optical efficiency	22.5 %	31.8%
P_{opt}	2.9 pW	4.9 pW
P_{sat}	7.2 pW	12.2 pW
$f_{\frac{P_{\mathrm{elec}}}{P_{\mathrm{opt}}}}$	1.5	1.5
T_c	428 mK	428 mK
T_b	250 mK	250 mK
G	40.7 pW/K	69.1 pW/K
g	76.4 pW/K	129.6 pW/K
C	0.76 pJ/K	1.30 pJ/K
R_{TES}	0.89	1.13
f_{R_N}	0.6	0.6
R_0	1.48	1.89
α	250	250
L	40	40
τ	1–5 ms	1–5 ms
τ_0	10 ms	10 ms

Table 4: Detector design parameters [43], [44]

If the time constant is too short, the detector bandwidth will exceed the readout bandwidth, and the detector operation will become unstable. On the other hand, if the time constant is large compared to the scanning speed of the telescope or the beam size, the $1/f$ noise of the bolometer signal will be large. The lower limit of the detector's time constant is limited by the bandwidth of the frequency-domain multiplexed readout electronics that provide the AC voltage bias to the bolometer wired to the LCR notch filter. A single value of L is used for each resonator so that an electrical time constant τ_{elec} is nearly constant for all resonators, and the variation is caused by the variation of R for each detector. The fundamental time constant of this readout circuit is set by,

$$\tau_{\mathrm{elec}} \leq \frac{L_{\max}}{R_{\min}} \tag{57}$$

where L_{max} and R_{min} are constrained by cross talk requirements and are typically ~ 20 nH and $\sim$1 , which give $\tau_{\mathrm{elec,max}} \approx 15$ ms. In τ_{elec} of 0.15 ms for TES operating at 0.8 Ω and a time constant of 0.9 ms for the fastest detector.

Furthermore, the bolometer operates in the high loop gain limit of $\mathcal{L} \gg 1$, $\beta = \frac{I}{R}\frac{\partial R}{\partial I} = 0$. The detector time constant constraint must be above 5.8 times the readout time constant [36].

$$\tau \geq 5.8 \times \tau_{\mathrm{elec}} \geq 5.8 \times (2 \times 0.15) = 0.9\,\mathrm{ms} \tag{58}$$

The upper limit of the allowable value of τ depends on the telescope's scanning speed and beam size. The PB-2 is designed to scan the sky at a speed of $\geq$1 [deg/sec], with a beam size of $\theta_{\mathrm{FWHM}} = 8$". Therefore, the fundamental time constant of the astronomical signal coupled through the telescope is given by $\tau_{\mathrm{sky}} = \theta_{\mathrm{FWHM}}/v_{\mathrm{scan}}$. Since the sky sample rate must be faster than the Nyquist frequency of the scan pattern, the time constant must be at least twice as large as τ_{sky}. In practice, an additional safety factor of 2 is introduced to ensure that the time constant is set properly even with manufacturing variations. The scan speed and beamwidth determine the upper limit of the detector time constant.

$$\frac{1}{\tau} \geq 2 \times \nu_{\mathrm{sky,Nyquist}} = 2 \times 2 \times \nu_{\mathrm{sky}} = 4 \times \frac{v_{\mathrm{scan}}}{\theta_{\mathrm{FWHM}}} \tag{59}$$

$$\tau \leq \frac{1}{4} \times \frac{\theta_{\mathrm{FWHM}}}{v_{\mathrm{scan}}} \sim 5\,\mathrm{ms}, \tag{60}$$

where v_{scan} is the telescope scanning velocity.

2.5.4 Lenslet

Each pixel is covered with a silicon lenslet, which optically couples with the sinuous antenna (Fig. 24). Since the lenslet and the planar fabrication wafer are made of silicon, a high dielectric material with $n = 3.1$, an AR coating is required. The lenslet is covered with a two-layer AR coating which is optimized for both 90 and 150 GHz bands (Fig. 25). The black coloration is an epoxy-based coating similar to that applied to optical elements in the receiver; the radius of the lenslet is 3.393 mm. We can find details on the fabrication of the lenslet in **??**.

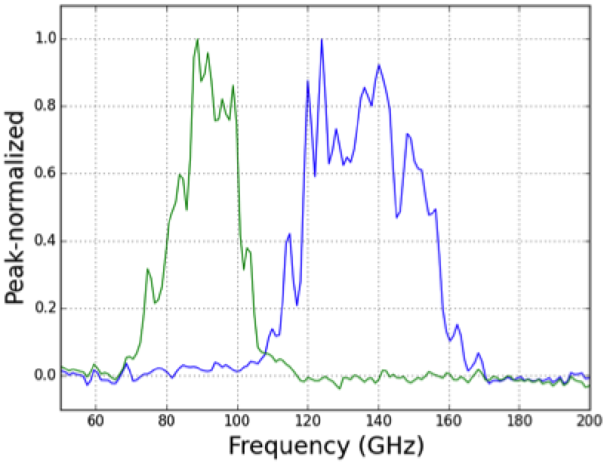

Figure 29: They are separated by microstrip filters for 90 GHz and 150 GHz [40].

2.6 Readout system

The readout system employs Digital frequency domain Multiplexing (DfMux) system and includes both cryogenic and ambient temperature components. The signal from TES bolometers is multiplexed by DfMux system and amplified in the cryostat at a temperature of about 4 K. To amplify the signal, we use a frequency multiplexed Superconducting Quantum Interference Device (SQUID).

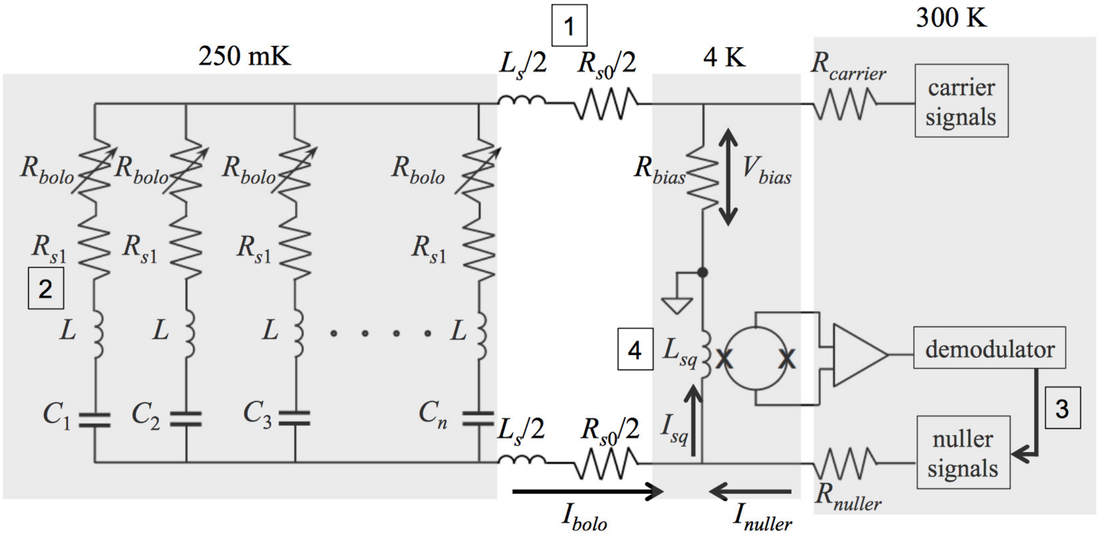

Figure 30: The schematic diagram of PB-2 readout system. In the PB-2, the DfMux provides biasing and readout of 40 detector channels with a single cryogenic cable between the 4 K SQUID array and the 250 mK detector stage [45].

2.6.1 DfMux system

Multiplexing system reduces the number of wiring which is required to read out individual bolometers. It reduces the thermal load through wiring on the cryogenic stage of the detector, which is cooled to $T \sim 0.3$ K. The multiplexing factor is determined from constraints on the cryogenic design of the experiment and electrical power consumption (Fig. 30).

The PB-2 uses Digital frequency domain Multiplexing (DfMux) system. In order to assign a resonant frequency to each detector for the multiplexing, the capacitance value C of each resonator is assigned individually. The maximum value of capacitance (the lowest resonant frequency) is set from the constraint of the physical size of the LC chip.

The bias frequency of each bolometer, f_k, is determined by the value of the LC connected in series and is given by

$$f_k = \frac{1}{2\pi\sqrt{LC_k}}, \tag{61}$$

where the index k is not attached to L because the PB-2 uses inductors of the same value for all bolometers ($L = 60\ \mu$ H). The frequency spacing is chosen to keep the crosstalk low and constant across the set of multiplexed detectors. Frequency assignments are logarithmic over a frequency range of 1.6 - 4.5 MHz, corresponding to a capacitance of 20 - 155 pF.

The LCR peaks are corresponding to

$$V_k = \frac{I}{R_{\mathrm{TES}} + i\omega L + \frac{1}{i\omega C_k}} \tag{62}$$

Where R_{TES} is the resistance of TES, ω is resonance frequency, and L is inductance, C_k is the capacitance of each channel. The DfMux provides biasing and readout of 40 detector channels (Fig. 31). The optical signal modulates the resistance of the TES, and the SQUID measures the resulting amplitude modulation of the bias current; the output voltage of the SQUID is digitized and demodulated to recover the signal for each readout channel. In the following, one set of multiplexed detectors is referred to as a ”comb.”

2.6.2 SQUID amplifier

The PB-2 uses a SQUID (Superconducting Quantum Interference Device) amplifier to read out the multiplexed signal from a voltage-biased TES bolometer as described above. A SQUID device with Josephson coupling has coupled a superconductor with a normal conductor or an insulator. The current signals are inductively coupled to a SQUID amplifier. The SQUID converts the current in each frequency band into a voltage by converting magnetic flux (Fig. 32).

In practice, a single SQUID loop does not provide sufficient amplification to read out the DfMux. However, combining many SQUIDs in an array can improve their amplification. For example, combining SQUIDs in series will noticeably increase trans-impedance, output impedance, input inductance, and noise decrease, while the gain remains unchanged. The SQUID in PB-2 is a series array of 100 SQUIDs, each with a bandwidth of several MHz.

The SQUIDs are susceptible devices for measuring current signals, but they are highly non-linear and have a large input impedance to the TES (Fig. 34). To solve this problem, a nulling current is supplied to the input coil of the SQUID as feedback. This nulling current

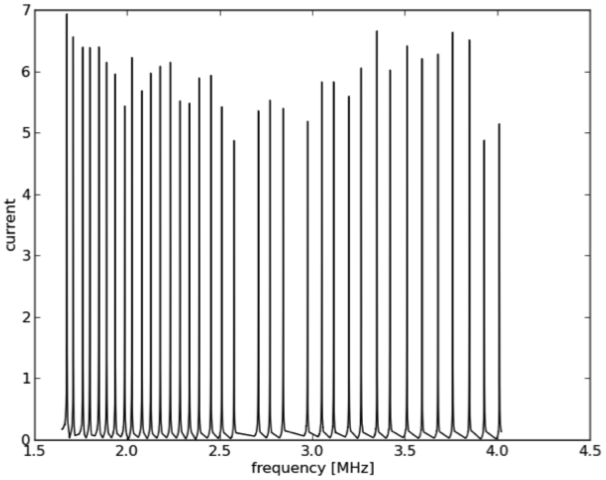

Figure 31: Example result of network analysis for a single set of 40 LC and TES bolometer [45].

is chosen to be entirely out of phase with the bias current of each detector, resulting in a zero bias current flowing through the input coil. This effectively reduces the input impedance of the SQUID to zero, improving its dynamic range.

For this feedback to the SQUID, the PB-1 uses analog feedback, but the PB-2 uses Digital Active Nulling (DAN) for wide bandwidth. The signal amplified by the SQUID is read out by a SQUID controller placed at room temperature, and the inductance of the SQUID input coil amplifies the readout noise. The SQUID in PB-2 was designed with an input inductance of 50 nH, input current noise of 5 pA/$\sqrt{\text{Hz}}$, and transformer impedance of 100 .

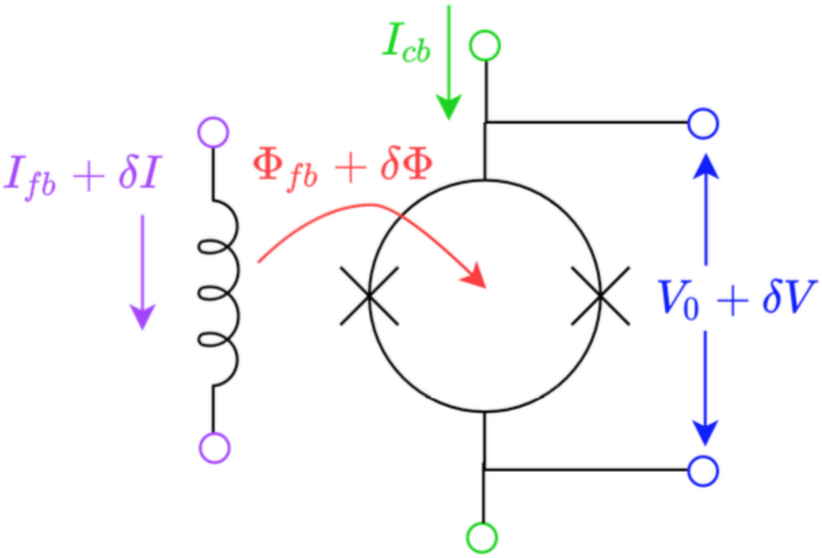

Figure 32: The input coil inductor coupled to the SQUID loop senses the increasing *deltaI* of the signal current. The current change induces a magnetic flux $\Phi_{\mathrm{f_b}} + \delta\Phi$ in the SQUID loop. where given a suitable current bias I_{cb}, the voltage at the SQUID junction changes by $V_0 + \delta V$. This figure is plotted by J. Groh [26].

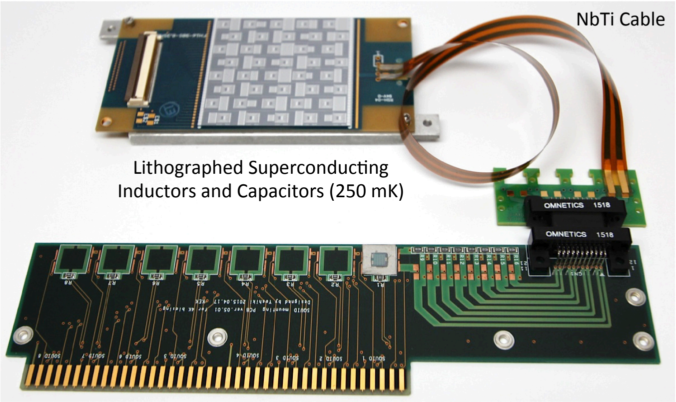

Figure 33: SQUID card. The SQUID board is installed on a 4 K stage.

The SQUID arrays are fabricated by lithography and divided into 4.5 mm x 4.5 mm silicon chips, as shown in Fig. 33. The SQUID board is installed on a 4 K stage and must be mounted away from the detector array with a $T \sim 4$ K PTC heat sink with a high cooling capacity to dissipate heat with current bias. A back-end of the receiver is surrounded by a cage that serves to protect the SQUID array amplifiers from electromagnetic interference (EMI). It also has six ports for signal readout, three each on the top and bottom of the receiver. Each port has 20 D-sub 37-pin connectors. The upper port reads out the bolometer signal, and the lower port reads out the thermometer signal from inside the receiver.

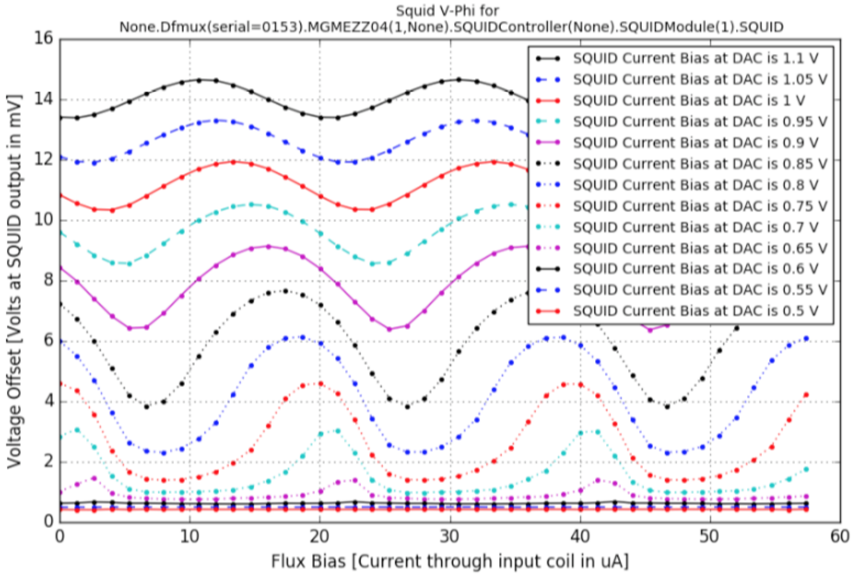

Figure 34: The response curve of a SQUID is shown for varying values of I_{bias} and I_{in}. Each colored line is a sweep of I_{in} while holding I_{bias} constant. This figure is plotted by T. Elleflot [46].

2.6.3 Data sampling

The samples measuring the response of the TES bolometer generate about 60 MB/s of data for the entire observatory at a sample rate of about 152 Hz. The readout board streams the detector samples via Ethernet to a control computer in a container adjacent to the telescope. They are repackaged into a compressible format convenient for offline analysis. This compressed data is then transferred via a radio link to the nearest town, San Pedro de Atacama. The data will then be delivered to PB-2 Collaboration computing sites worldwide.

2.7 Standard operation

The basic daily schedule is as follows: after the refrigeration cycle to cool the focal plane tower is completed, the bolometers are tuned, a calibration measurement (see Chapter 3) to check the tuning status is performed for about 10 minutes, an Elnod scan is performed, and a scan called Constant Elevation Scans (CES) is performed to observe the CMB. Calibration measurements are also taken before and after the CES observations; each observation patch for observing the CMB is available for six to eight hours per day. For each patch of observations, we work at a constant elevation angle during each CES and scan back and forth in azimuth while the patch moves through the sky.

Remote observations are basically used for regular daily observations. The data includes time-ordered data from the readout electronics that measure the response of the TES bolometer. The data also contains information about the position through which the telescope scans the sky, the temperature of the cryostat, helium pressure, and weather conditions at the observatory. By monitoring these various types of data, we can detect and correct problems early and minimize downtime.

2.8 Deployment to Chile

The POLARBEAR-2 receiver was developed at the High Energy Accelerator Research Organization (KEK). After that, the receiver was disassembled and transported to the Chilean observatory in 2018. The receiver was then assembled and integrated into the telescope at the Chilean observatory. The gain calibrator stimulator, described later, was also installed during this period (Fig. 35). The instrument commissioning started in January 2019 [**?**]. The first commissioning period for PB-2 is from the first light in January 2019 until the site shut down in February 2020 by COVID-19. After that, we resumed the commissioning test again in January 2021, and the commissioning test has been conducted until now. The results in this paper are based on the data acquired during the first commissioning period and the first half of this period of the second commissioning period.

Figure 35: The PB-2 receiver installed to the telescope (left) and the stimulator installed in the back of the secondary mirror (right).

3 Gain Calibration

3.1 Systematic errors

CMB polarization experiments' high sensitivities require high statistical precision and minimization of systematic errors. A false estimation systematic error can cause a misunderstanding of the faint CMB polarization signals. Therefore, the evaluation of systematic errors is becoming more critical in recent data analysis. This section discusses the main systematics and its effect on the CMB power spectrum.

3.1.1 Scan strategies

With a patch on the sky of angular extent $\Delta\theta$, the maximum angular scale that can be probed is given by $\ell_{\rm min} \approx 180°/\Delta\theta$. For example, in order to measure $\ell_{\rm min} \sim 50$, $\Delta\theta$ must be greater than $3.6°$. the uncertainty of the anisotropy map per unit solid angle, the so-called map depth w_T, is proportional to the square root of the patch size. If the region is scanned uniformly, the map depth of the temperature anisotropy can be obtained as

$$w_T^{-1/2} = \sqrt{\frac{4\pi f_{\rm sky}}{t_{\rm obs}}}\frac{NET_{\rm bolo}}{\sqrt{N_{\rm bolo}}} = \sqrt{\frac{4\pi f_{\rm sky}}{t_{\rm obs}}}NET_{\rm array} \tag{63}$$

where $NET_{\rm array}$ is the momentary noise-equivalent temperature of the detector array with $N_{\rm bolo}$ bolometers, $t_{\rm obs}$ is the total observation time, and $4\pi f_{\rm sky}$ is the patch size. Here, we assume that the scan covers the overall scan patch. $f_{\rm sky}$ is a fraction of sky coverage. The experiment can only measure the CMB at a fraction of the whole sky or $f_{\rm sky} < 1$, which reduces the number of modes available to average out the noise.

The map depth $w_P^{-1/2}$ of the polarization anisotropy map in a bolometric experiment is usually given by

$$w_P^{-1/2} = \sqrt{2}w_T^{-1/2} \tag{64}$$

How the patch is scanned coupled with the low-frequency noise performance of the detectors will limit the maximum angular scale that can be probed. The angular power-spectrum is estimated from the two-dimensional Fourier transform of the observed anisotropy map. Uncertainty in the angular power-spectrum due to the noise in the map and the sample variance. The statistical uncertainty per single Fourier mode, N_ℓ, can be expressed by the map depth as [47],

$$N_\ell = \omega_{\rm P}^{-1}e^{\ell(\ell+1)\sigma_{\rm b}^2} = \omega_{\rm P}^{-1}W_\ell^{-1} \tag{65}$$

where $W_\ell = e^{-\ell(\ell+1)\sigma_{\rm b}^2}$ is a window function. The exponential term represents the degradation of sensitivity due to resolution assuming a Gaussian beam with $\sigma_{\rm b} = \theta_{\rm FWHM}/\sqrt{8\ln 2}$. σ_b is the beamwidth of telescope. For the uncertainty of angular power spectrum, we can improve the uncertainty by averaging among Fourier modes as

$$\Delta C_\ell^{BB} = \sqrt{\frac{2}{(2\ell+1)f_{\rm sky}}}(C_\ell^{BB} + N_\ell) \tag{66}$$

Here, $(2\ell+1)f_{\rm sky}$ is the approximate number of modes of multipole ℓ, and the C_ℓ term in parentheses is the sample variance, where ΔC_ℓ^{BB} is minimum for maximum $f_{\rm sky}$. Since the realization of CMB anisotropy can be observed only once in the real universe, estimating the angular power spectrum inevitably involves Poisson noise, which is the so-called cosmic sample variance. When the statistical uncertainty becomes less than the sample variance, it is necessary to increase the number of modes to reduce the sample variance.

3.1.2 Beam contamination

Since the B-mode signal be faint, controlling the various systematic effects is needed. Systamatic error in signals can be divided into two categories, the leak intensity into polarization and the mix polarization states. Such effects can be modeled generically by constructing the Muller-matrix that transforms the Stokes vector on the sky into that observed by the detector.

The PB-2, like the PB-1, uses polarization signals from two orthogonal polarization detectors in a single pixel. This paired difference method is effective for measuring linear polarization like CMB polarization. Each detector in a single spatial pixel has its sky beam. Ideally, this detector beam would have the same shape and power as it propagates upward through the optical system. So taking the difference in the time-ordered data measured from each detector in a single pixel, the clear polarization signa measured with the sky overlap beam. However, due to detector characteristics and optical design effects, the shape and power of the two sky beams are usually not identical. Any asymmetry or non-ideality of the beam that differs from the original detector beam will result in the systematics of the difference beam. In the presence of difference beam systematics, when the beam and sky map is convolved in Fourier space after subtracting the two paired beams, the residual leakage due to the difference beam characteristics causes systematic errors in the power spectrum. Therefore, the analysis should be carefully performed to consider the optical and detector non-idealities.

The systematic of the difference beam is mainly caused by the detector and optical design of the instrument. The directivity and beam profile of the detector is determined by the coupling between the antenna and the lenslet. In addition, the design of the reflective optics themselves will also produce differential beams, as orthogonal polarization states differ as they propagate through the optical system.

For the simple case, polarization is measured using orthogonal pair bolometers. Each bolometer beam can be modeled with an elliptical Gaussian profile as,

$$B(x,y) = \frac{1}{2\pi\sigma_x\sigma_y}\exp\left(-\frac{(x-\rho_x)^2}{2\sigma_x^2}-\frac{(y-\rho_y)^2}{2\sigma_y^2}\right) \tag{67}$$

with individual detector ellipticities given by $e = (\sigma_x - \sigma_y)/(\sigma_x + \sigma_y)$, where σ_x, σ_y is the Gaussian beam sizes of each detectors [48] [41]. Then the differential beam are defined in Table 5. And an illustration of differential beam patterns for each effect shown in Fig. 36.

How this beam differential contributes to systematic errors is also dependent on the properties of the scan strategy. We use the $f_{1,2}$ as a parameter that depend on the mitigated leakage by scan strategy [49] [50].

Effect	parameter	Definition
Differential Gain	ΔG	$G_1 - G_2$
Differential Gain fraction	γ	$\frac{G_1-G_2}{G_1+G_2}$
Differential beam width(Monopole)	μ	$\frac{\sigma_1-\sigma_2}{\sigma_1+\sigma_2}$
Differential Pointing(Diepole)	ρ	$\rho_1 - \rho_2$
Differential ellipticity(Quadrupole)	e	$\frac{\sigma_x-\sigma_y}{\sigma_x+\sigma_y}$
Differential Rotation	ε	$\frac{1}{2}(\varepsilon_1 + \varepsilon_2)$

Table 5: Definitions of terms used in differential beam property discussions [48].

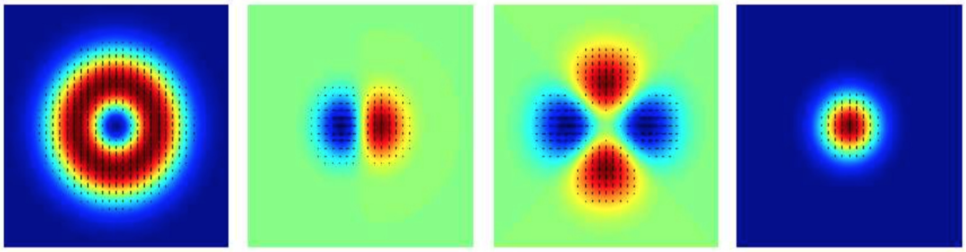

Figure 36: Differential beam systematics. An illustration from differential beamwidth(the monopole), differential pointing (dipole), differential ellipticity (quadrupole) and differential gain effects; Q parameter only is depicted. Figure is from [48].

3.2 Calibration requirement for POLARBEAR-2 experiment

It is necessary to design the instrument so that these systematic errors are controllable and low. Therefore, a design criterion should be estimated in advance to guide the device design. This design criterion is used as a benchmark or upper limit in developing the device so that the systematic errors due to these effects are smaller than the statistical errors expected in the experiment. In PB-2, the design criteria are as Table 7 [30],

A design criterion requires systematic leakage to be less than or equal to the statistical error of the respective device in all experiments. For differential gain, a design criterion is computed that requires systematic leakage to be less than or equal to the statistical error of each device at $\ell = 100$ near the original peak. In determining the design criteria, the scanning strategy is also assumed to be $f_{1,2} = 1$, but this is not entirely ideal. In reality, any scanning strategy chosen will have $f_{1,2} < 1$; this criterion will be conservative [30].

3.3 Gain calibration

To accurately measure the CMB polarization, it is essential to evaluate and understand the systematic error. Therefore, it is necessary to measure each parameter related to the detector output and calibrate it [51]. In particular, among these parameters, the stimulator, the gain calibrator, plays a critical role in measuring the gain response (time response). This paper mainly focuses on the gain calibration using the stimulator independently, and the case of using the HWP is discussed in the appendix.

Effect	ΔC_ℓ^{EE}	ΔC_ℓ^{BB}
Differential gain	$\Delta G^2 f_1 \star C_\ell^{TT}$	$\Delta G^2 f_1 \star C_\ell^{TT}$
Differential beam width(Monopole)	$4\mu^2(\ell\sigma)^4 f_1 \star C_\ell^{TT}$	$4\mu^2(\ell\sigma)^4 f_1 \star C_\ell^{TT}$
Differential pointing(Diepole)	$c_\theta^2 J_2^2(\ell\rho) + J_1^2(\ell\rho) C_\ell^{TT} \star f_2$	$s_\theta^2 J_2^2(\ell\rho) - J_1^2(\ell\rho) C_\ell^{TT} \star f_2$
Differential ellipticity(Quadrupole)	$\ell_1^2(z) c_\theta^2 C_\ell^{TT}$	$I_1^2(z) s_\theta^2 C_\ell^{TT}$
Differential rotation	$4\varepsilon^2 C_\ell^{BB}$	$4\varepsilon^2 C_\ell^{EE}$

Table 6: Contributions of various differential beam asymmetries to systematic errors in the E-mode and B-mode angular spectra [48].

Systematics	150GHz	90GHz
Differential Gain fraction	0.019 %	0.019 %
Differential beam width(Monopole)	0.474 %	0.215 %
Differential Pointing(Diepole)	0.877”	0.877”
Differential ellipticity(Quadrupole)	0.948 %	0.430 %

Table 7: various differential beam systematics design criteria [30].

3.3.1 Gain difference

In CMB polarization experiments, we measure the CMB polarization intensity by comparing the signal of a couple of detectors in one pixel. Using Stokes parameters T, Q, U, an output of a couple of the bolometer $V_i (i = 1, 2)$ are described as,

$$V_1 = G_1 \cdot (T + \epsilon_1[Q \cos 2\phi_1 + U \sin 2\phi_1]) \tag{68}$$

$$V_2 = G_2 \cdot (T + \epsilon_2[Q \cos 2\phi_2 + U \sin 2\phi_2])\,. \tag{69}$$

Here G_i is defined as the gain response. The gain is the conversion factor between the temperature on the sky (units Kelvin) and the output of the bolometer (units Volt). T represents the total intensity (temperature), while Q and U represent linearly polarized components. $\phi_i = \phi_i(\nu)$ the orientation angle of the anntena, which is calibrated by polarizing planets or wire grid measurements [52]. ϵ_i is the polarization leakage, which is calibrated by polarizing planets. The difference of the output of detector, and the difference between the pair detectors ΔV is derived as,

$$\Delta V = (G_1 - G_2)T + (\epsilon_1 G_1 \cos 2\phi_1 - \epsilon_2 G_2 \cos 2\phi_2)Q + (\epsilon_1 G_1 \sin 2\phi_1 - \epsilon_2 G_2 \sin 2\phi_2)U \tag{70}$$

In ideal case, $\Delta G \equiv G_1 - G_2 \sim 0$. Actuality, the difference ΔG is not zero.If there are any uncertainty of gain difference ΔG, the non-polarized T component leaks into the polarized Q and U components. The effect of the residual difference is observed as quasi-polarized light [50]. As mentioned in the previous section, the systematic errors in the power spectrum can be estimated by expanding the beam and Fourier transforming the sky map. The result depends on the beam characteristics of the receiver and the scanning method of observation. $\Delta G^2 f_1 \star C_\ell^{TT}$ is the systematic of the spectral of B-mode from C_ℓ^{TT} via ΔG. f_1 is a parameter that depends on the scanning parameter of observation. The gain difference works as a systematic error of the spectrum of the B mode, as shown in calibration requirements. For example, when the gain difference ΔG is 1 %, 10^{-4} fraction of C_ℓ^{TT} leaks as a systematic error due to the gain difference in each of the B mode. The observed spectrum at the target sensitivity is suppressed on the large-angle scale at $\ell < 100$.

3.3.2 Relative gain calibration

Generally, the gain G of each detector is not constant during the season. The gain G keeps fluctuating due to the bolometer's tuning bias and optical loading status. We refer to the time variation of the gain over season $\delta G/G$ as a "relative gain" variation. To compensate for the relative gain, we developed a stimulator, gain calibrator, to measure the gain before and after the observation; the details of the stimulator are described in a next section.

3.3.3 Absolute gain calibration

The absolute gain of the bolometer is derived directly from the measurements of the planet. The bolometer absolute gain is measured and calibrated by observing planets with known antenna temperatures (Jupiter, Saturn, etc.). However, the absolute gain by observing planets is not perfect because of systematic errors in planetary temperature modeling due to planetary brightness and detector bandpass. To make absolute measurements of the C_ℓ^{BB} spectrum, an absolute calibration of the gain is necessary. The most accurate absolute calibration is the CMB signal itself. Therefore, an absolute gain factor is finally determined to minimize the difference between the best fit of the measured C_ℓ^{TT} spectrum and the C_ℓ^{TT} spectrum with ΛCDM measured by WMAP-9 [53].

The relative gain measured by the stimulator is finally corrected as an absolute gain value and used in future analysis.

3.3.4 Gain calibration methods

In order to complete the sensor calibration, various methods are required to be combined. Some methods are absolute calibration that can convert bolometer output directly into temperature on the sky. The others are called relative, which only provides the gain compared to that at a certain time. The periods to perform calibration is important too because the gain fluctuation occurs in every time scale. The calibration schedule is determined considering the methods' performance and utility. There are a lot of methods developed for CMB observations. Commonly utilized methods are summarized in Table 8. The stimulator is included in "Thermal source". We introduce our observation instrument and requirements for the calibration in a later section.

Method	gain	Remark	Ref.
Dipole	Absolute	Diffucult from the ground	[54]
C_ℓ^{TT}	Absolute	Comparing with reference CMB spectrum	[55–57]
Planet	Absolute	Dependent of their position	[58]
Elevation nod	Relative	Moving telescope elevation to change sky loading	[59]
Thermal source	Relative	Black-body of controlled temperature	[55, 60]
Bias tickle	Relative	Method performed in readout circuit	[61]

Table 8: Methods to calibrate sensor gain in CMB measurements. Dipole and C_ℓ^{TT} are calibration method given as CMB distribution in the sky. Planet and Elevation nod are observation method of something optical other than CMB. Thermal source and Bias tickle are operation using apparatus on ground. The stimulator is included in "Thermal source".

4 Gain Calibrator for POLARBEAR-2

4.1 Instrument model for gain requirements

First, to estimate the required value of the device for relative gain calibration and time response, we consider a simple model in this section.

The word gain in this section means relative gain. The relative gain is assumed to vary mainly due to the tuning of the detector and the loading condition at each scan. In this section, we enumerate requirements determined by higher-level scientific and technical requirements. To calculate each value, we assume parameter as follows unless specially remarked, noise level of single detector: $NET_{\rm bolo} = 360\,\mu{\rm K}\sqrt{\rm s}$ (NET stands for Noise Equivalent Temperature) and measurement time: $t_{\rm obs} = 120$ seconds per frequency During the observation, the gain is assumed to be changing slowly and linearly, and the stimulator can evaluate the change before and after the scan. It is also assumed that the same intensity of light is incident on the same pixel.

4.1.1 Basic model (gain)

The calibration of the gain and the time constant require the stimulator's intensity and stability.

For simply, let $V_{\rm obs} = g \cdot T_{\rm stm}$, where $V_{\rm obs}$ [V] is the power measured by a single detector, g is the relative gain measured by stimulator, and $T_{\rm stm}$ [K] is the intensity of the stimulator signal. Here, $T_{\rm stm}$ and its error $\sigma_{T_{\rm stm}}$ is common parameter to all detectors.

$$g \equiv \frac{V_{\rm obs}[{\rm V}]}{T_{\rm stm}\ [{\rm K}]} \tag{71}$$

$$\delta g = \sqrt{\left(\frac{1}{T_{\rm stm}}\right)^2 \sigma^2_{V_{\rm obs}} + \left(\frac{V_{\rm obs}}{I^2_{\rm stm}}\right)^2 \sigma^2_{T_{\rm stm}}} \tag{72}$$

$$\frac{\delta g}{g} = \sqrt{\left(\frac{\sigma_{V_{\rm obs}}}{V_{\rm obs}}\right)^2 + \left(\frac{\sigma_{T_{\rm stm}}}{T_{\rm stm}}\right)^2} = \sqrt{\frac{1}{g^2}\left(\frac{\sigma_{V_{\rm obs}}}{T_{\rm stm}}\right)^2 + \left(\frac{\sigma_{T_{\rm stm}}}{T_{\rm stm}}\right)^2} \tag{73}$$

Using $NET[\mu K\sqrt{s}]$ and observation time t [s], $\sigma_{V_{\rm obs}}$ is described as,

$$\sigma_{V_{\rm obs}} = \frac{g \cdot NET}{\sqrt{t}}. \tag{74}$$

Then, eq.(73) is rewritten as

$$\frac{\delta g}{g} = \sqrt{\left(\frac{NET}{T_{\rm stm}\sqrt{t}}\right)^2 + \left(\frac{\sigma_{T_{\rm stm}}}{T_{\rm stm}}\right)^2}. \tag{75}$$

In particular, considering the case of each stimulator measurement, let $\delta g_{\rm array}$ be the error when averaged over all detectors in a single stimulator measurement; $\delta g_{\rm array} = \delta g_{\rm bolo}/\sqrt{N_{\rm bolo}}$. When the array noise $NET_{\rm array} = NET_{\rm bolo}/\sqrt{N_{\rm bolo}} = 5.6\ \mu{\rm K}\sqrt{\rm s}$ is small enough,

$$\frac{\delta g_{\rm array}}{g_{\rm array}} = \sqrt{\left(\frac{NET_{\rm array}}{T_{\rm stm}\sqrt{t}}\right)^2 + \left(\frac{\sigma_{T_{\rm stm}}}{T_{\rm stm}}\right)^2} \sim \frac{\sigma_{T_{\rm stm}}}{T_{\rm stm}} \tag{76}$$

In addition, let δg_{bolo} be the error per detector in one measurement. In the following, since we want to obtain the lower limit of T_{stm}, we assume in particular that $\sigma_{T_{\mathrm{stm}}}$ is small enough and used the following equation,

$$\frac{\delta g_{\mathrm{bolo}}}{g_{\mathrm{bolo}}} = \sqrt{\left(\frac{NET_{\mathrm{bolo}}}{T_{\mathrm{stm}}\sqrt{t}}\right)^2 + \left(\frac{\sigma_{T_{\mathrm{stm}}}}{T_{\mathrm{stm}}}\right)^2} \sim \frac{NET_{\mathrm{bolo}}}{T_{\mathrm{stm}}\sqrt{t}} \tag{77}$$

4.1.2 Basic model (time response)

With time constant τ [ms] and chopping frequency f [Hz] ($f_{\mathrm{max}} = 50$ [Hz]), expected output follows next formula,

$$V_{\mathrm{obs}} = \frac{g \cdot T_{\mathrm{stm}}}{\sqrt{1 + (\tau\omega)^2}} \tag{78}$$

Where $\omega = 2\pi f$. Measurement value at $\omega \sim 0$,

$$V_0 = g \cdot T_{\mathrm{stm}} \tag{79}$$

Measurement value at $\omega_1 = 2\pi f_{\mathrm{max}}$

$$V_1 = \frac{g \cdot T_{\mathrm{stm}}}{\sqrt{1 + (\tau\omega_1)^2}} \tag{80}$$

Then, estimated time constant is

$$\tau = \frac{1}{\omega_1}\left\{\left(\frac{V_0}{V_1}\right)^2 - 1\right\}^{\frac{1}{2}} \tag{81}$$

An error of time constant measurement value $\delta\tau$ is as, using V_0, V_1,

$$\delta\tau \equiv \sqrt{\left(\frac{\partial\tau}{\partial V_0}\right)^2 (\delta V_0)^2 + \left(\frac{\partial\tau}{\partial V_1}\right)^2 (\delta V_1)^2} \tag{82}$$

Then,

$$\delta V_1 = \frac{\delta V_0}{\sqrt{1 + (\tau\omega_1)^2}} = \frac{g \cdot NET_{\mathrm{bolo}}}{\sqrt{1 + (\tau\omega_1)^2}\sqrt{t}} \tag{83}$$

And

$$\delta\tau = \frac{\sqrt{2}(1 + (\tau\omega_1)^2)}{\omega_1^2 \tau T_{\mathrm{stm}} g}\delta V_0 = \frac{\sqrt{2}(1 + (\tau\omega_1)^2) NET_{\mathrm{bolo}}}{\omega_1^2 \tau T_{\mathrm{stm}}\sqrt{t}} \tag{84}$$

For example, in the case that $NET_{\mathrm{bolo}} = 360\mu\mathrm{K}\sqrt{\mathrm{s}}$, $T_{\mathrm{stm}} = 40\,\mathrm{mK}$, $\tau = 1$ msec, $f = 50$ Hz, then $\delta\tau \sim 0.01$ [ms], And this is small enough.

4.2 System requirements from systematics

4.2.1 (A) I to P leakage from gain mismach

The gain difference error makes systematic. In 3.2, $\langle \delta G_{\mathrm{frac}} \rangle$ is needed to be less than 0.019% . The relative gain difference between detectors δG_{bolo} for each detector δG_{frac} [5]is s

$$\delta G_{\mathrm{frac}} = \frac{\delta G_{\mathrm{bolo}}}{\sqrt{2}} + \delta G_{\mathrm{sys}} \tag{85}$$

Here, δG_{sys} is the instrument-derived systematic error, which comes from the bolometer bandpass, mirror-derived polarization, and asymmetry of the optics. In one season (one year), we assume that 600 CES observations are taken. The number of paired bolometers is about 3600, so if we assume that there is no instrument-derived systematic error in the measurement at each CES. We get, without no systematics from instruments, and after focal plane and observation averaging,

$$\langle \delta G_{\mathrm{frac}} \rangle = \frac{\delta G_{\mathrm{frac}}}{\sqrt{N_{\mathrm{obs}} N_{\mathrm{pixel}}}} \sim \frac{\delta G_{\mathrm{bolo}}}{1740} \cdot \left(\frac{N_{\mathrm{obs}}}{600}\right)^{-\frac{1}{2}} \cdot \left(\frac{N_{\mathrm{bolo}}}{3600}\right)^{-\frac{1}{2}} \tag{86}$$

$$\frac{\delta g_{\mathrm{bolo}}}{g_{\mathrm{bolo}}} = \frac{NET_{\mathrm{bolo}}}{T_{\mathrm{stm}}\sqrt{t}} < \delta G_{\mathrm{bolo}} = 1740 \times 0.019 \sim 47 \ [\%] \tag{87}$$

Substituting $NET_{\mathrm{bolo}} = 360\mu\mathrm{K}\sqrt{\mathrm{s}}$, $t_{\mathrm{obs}} = 120$ s, $\delta g_{\mathrm{bolo}} = \sqrt{2}\delta g_{\mathrm{frac}}$. Then,

$$T_{\mathrm{stm}} > \frac{360\mu K}{47\%\sqrt{120}} \sim 0.1 \text{ mK} \tag{88}$$

The required temperature stability is

$$\frac{\sigma_{T_{\mathrm{stm}}}}{T_{\mathrm{stm}}} \sim \frac{\sigma_{T_{\mathrm{Heater}}}}{T_{\mathrm{Heater}}} < \frac{\delta g_{\mathrm{array}}}{g_{\mathrm{array}}} = \frac{\delta G_{\mathrm{bolo}}}{\sqrt{N_{\mathrm{pixel}}}} = 0.65\% \tag{89}$$

4.2.2 (B) Monitor before and after gain variation

Consider the change in gain g_{scan} during the observation. The major shift in nonlinearity is due to the change in loading to the detector caused by the temperature fluctuation of the focal plane. Here, we assume that the gain g_{scan} changes nonlinearly with $g_1 = 1\%/\,\mathrm{K}$. since PB1 has a nonlinear gain change of about 1 % for loading change $\delta T = 1$ K before and after one CES from the actual measurement. So we assume that the gain is more stable than this. However, if the nonlinearity in the detector of PB-2 is sufficiently smaller than that of PB1, the required value becomes more stringent. Therefore, it is necessary to evaluate the nonlinearity of the PB-2 detector in detail by actual measurement in the future.

$$\frac{\delta g_{\mathrm{scan}}}{g_{\mathrm{scan}}} \approx g_1 \Delta T \sim 1\% \cdot \left(\frac{g_1}{1\%/\,\mathrm{K}}\right) \cdot \left(\frac{\delta T}{1\,\mathrm{K}}\right) \tag{90}$$

---

[5] The definition is $G_{\mathrm{frac}} = \frac{G_1 - G_2}{G_1 + G_2}$. $\delta G_{\mathrm{frac}} = \frac{2G_1 G_2}{(G_1+G_2)^2}\sqrt{\frac{\delta G_1^2}{G_2} + \frac{\delta G_2^2}{G_1}} \sim \frac{1}{\sqrt{2}}\frac{\delta G}{G}$ if $G_1 = G_2 = G$ and $\delta G_1 = \delta G_2 = \delta G$

Here, we require that the gain measurement can be performed with better accuracy than the gain change during scan.

$$\frac{\delta g_{\mathrm{array}}}{g_{\mathrm{array}}} < 1\% \tag{91}$$

$$\frac{\sigma_{T_{\mathrm{stm}}}}{T_{\mathrm{stm}}} \sim \frac{\sigma_{T_{\mathrm{Heater}}}}{T_{\mathrm{Heater}}} < 1\% \tag{92}$$

For example, when $T_{\mathrm{stm}} \sim 1000$ K, $\sigma_{T_{\mathrm{stm}}}$ is need to be less than $10\,K$. For calculating the lower limit of signal intensity, using eq.(77),

$$\frac{NET_{\mathrm{bolo}}}{T_{\mathrm{stm}}\sqrt{t}} < 1\% \tag{93}$$

The required temperature intensity is

$$T_{\mathrm{stm}} > 3\,\mathrm{mK} \cdot \left(\frac{\mathrm{t}}{120\,\mathrm{s}}\right)^{-\frac{1}{2}} \tag{94}$$

4.3 System requirement from instrument

4.3.1 (C) Designed time constant value

The PB-2 bolometer's time constant value τ is designed is $1 - 5\,\mathrm{ms}$. Required calibration accuracy is $\delta\tau < 0.1\,\mathrm{ms}$. From eq.(84),

$$\delta\tau = \frac{\sqrt{2}(1+(\tau\omega)^2)NET_{\mathrm{bolo}}}{\omega^2\tau T_{\mathrm{stm}}\sqrt{t}} < 0.1\,\mathrm{ms} \tag{95}$$

Then, from the inequality of arithmetic and geometric means,

$$T_{\mathrm{stm}} > \frac{\sqrt{2}NET_{\mathrm{bolo}}}{\omega^2\sqrt{t}\cdot 0.1\,\mathrm{ms}^{-1}} \cdot \left(\frac{1}{\tau} + \tau\omega^2\right) > \frac{\sqrt{2}NET_{\mathrm{bolo}}}{\omega^2\sqrt{t}\cdot 0.1\,\mathrm{ms}^{-1}} \cdot 2\,\omega \tag{96}$$

The required temperature intensity is

$$T_{\mathrm{stm}} > \frac{2\sqrt{2}NET_{\mathrm{bolo}}}{\omega T_{\mathrm{stm}}\sqrt{t}} \sim 3\,\mathrm{mK} \cdot \left(\frac{\omega}{2\pi \times 50\,\mathrm{Hz}}\right)^{-1} \left(\frac{\mathrm{t}}{120\mathrm{s}}\right)^{-\frac{1}{2}} \tag{97}$$

4.3.2 (D) Relative gain error < absolute gain error

The calibration accuracy of relative gain by the stimulator measurement is required to be better than the calibration accuracy of absolute gain by spectrum. The accuracy of absolute gain is determined by instrument design and scan strategy. We describe the absolute gain error as G_{abs}.

$$C_l^{TT} \approx G_{\mathrm{abs}}^2 \tag{98}$$

$$\delta C_l^{TT} \approx 2G_{\text{abs}}\delta G_{\text{abs}} \tag{99}$$

Here we assumed $G_{\text{abs}} = 1$. δG_{abs} can be estimated as sample variance.

$$\delta G_{\text{abs}} \approx \frac{1}{2}\delta C_l^{TT} \approx \frac{1}{2\sqrt{N_{\text{mode}}}} \approx \frac{1}{2}\sqrt{\frac{1}{f_{\text{sky}}\sum_l^{l_{\text{max}}}(2l+1)}} \sim \frac{1}{2\sqrt{f_{\text{sky}}}l_{\text{max}}} \tag{100}$$

Here N_{mode} is number of mode,

$$\delta G_{\text{abs}} \sim 0.03\% \cdot \left(\frac{f_{\text{sky}}}{65\%}\right)^{-\frac{1}{2}} \cdot \left(\frac{l_{\text{max}}}{2000}\right)^{-1} \tag{101}$$

Averaged δg_{array} is need to be smaller than δG_{abs}. Averaged δg_{array} is

$$\langle \delta g_{\text{array}} \rangle \sim \frac{\delta g_{\text{array}}}{25}\left(\frac{N_{\text{obs}}}{600}\right)^{-\frac{1}{2}} \tag{102}$$

Here $NET_{\text{array}} = 5.6\mu K\sqrt{t}$. In one season (one year), we assume that 600 CES observations are taken. Considering NET_{array} is small enough and $\langle \delta g_{\text{array}} \rangle / g_{\text{array}} < \delta G_{\text{abs}}/G_{\text{abs}}$, the required temperature stability in one CES is

$$\frac{\delta g_{\text{array}}}{g_{\text{array}}} \sim \frac{\sigma_{T_{\text{stm}}}}{T_{\text{stm}}} < 0.03\% \times \sqrt{N_{\text{obs}}} \sim 0.75\% \tag{103}$$

$$\frac{\sigma_{T_{\text{stm}}}}{T_{\text{stm}}} \sim \frac{\sigma_{T_{\text{Heater}}}}{T_{\text{Heater}}} < 0.75\% \tag{104}$$

Next, thinking the δg_{bolo} case for calculating the required temperature intensity.

$$\langle \delta g_{\text{bolo}} \rangle = \frac{\delta g_{\text{bolo}}}{\sqrt{N_{\text{obs}}N_{det}}} \sim \frac{\delta g_{\text{bolo}}}{1470}\left(\frac{N_{\text{obs}}}{600}\right)^{-\frac{1}{2}}\left(\frac{N_{\text{bolo}}}{3600}\right)^{-\frac{1}{2}} \tag{105}$$

Considering T_{stm} is small and $\langle \delta g_{\text{bolo}} \rangle / g_{\text{bolo}} < \delta G_{\text{abs}}/G_{\text{abs}}$. The required temperature intensity is

$$\frac{\delta g_{\text{bolo}}}{g_{\text{bolo}}} \sim \frac{NET_{\text{bolo}}}{T_{\text{stm}}\sqrt{t}} < 0.03\% \times \sqrt{N_{\text{obs}}N_{\text{bolo}}} \sim 44\% \tag{106}$$

$$T_{\text{stm}} > \frac{360\mu K}{44\%\sqrt{120}} \sim 0.8\text{mK} \tag{107}$$

4.3.3 (E) The accuracy of time constant measurement for chopper frequency

The accuracy of the time constant is proportional to the accuracy of modulation frequency. Therefore, to avoid systematic bias in estimating τ, we require an order of magnitude smaller f precision, 10% relative.

4.3.4 (F) Chopping timing readout.

For analyzing the modulated signal, the timing of the TES readout and stimulator system is synchronized. Not to confuse every chopping timing, a timing resolution must be better than the chopping period at a maximum frequency. In item (C), we assumed $f_{\max} = 44\,\mathrm{Hz}$ (11 ms on-off interval). The timing resolution in 0.1 ms is enough to recognize the chopping period.

4.4 System requirements summary

Table 9 is the summary table. From item (A)-(D), we need the intensity is lager than 3 mK and the signal stability less than $< 0.65\%$ (one CES), $< 0.03\%$ (one Season) Table 10.

Item	Intensity	Stability
I to P leakage from gain mismach	> 0.1 mK	<0.65 % (1CES)
Monitor before and after gain variation	> 3 mK	<1% (1CES)
designed time constant value	> 3 mK	–
Relative gain error $<$ absolute gain error	> 0.8 mK	<0.75 % (1CES), $< 0.03\%$ (1 Season)
τ resolution (modulation frequency)	($> 44\,\mathrm{Hz}$)	10%
(encoder timing)	-	$< 11\,\mathrm{ms}$

Table 9: short summary for requirement ($t_{\mathrm{obs}} = 120\mathrm{sec}$)

Item	requirements
Intensity	3 mK($t_{\mathrm{obs}} = 120\,\mathrm{sec}$)
stability	one CES $< 0.65\%$, one Season $< 0.03\%$

Table 10: Requirement summary for design of system

4.5 Gain calibrator (stimulator)

The stimulator has a ceramic heater (1000K) as the thermal radiation source, which covers up to two observation frequency bands (90/150 GHz) (Fig. 37). And we use the optimized horn for the optical system. The stimulator is optically coupled with the detectors through a nine-millimeter diameter light pipe penetrating the secondary mirror. And the light is chopped (with a mechanical chopper) to modulate the reference signal. This modulated signal is emitted through a light pipe to the PB-2 receiver. We can estimate the relative gain of the detectors by monitoring the response to the stable optical signal from the stimulator.

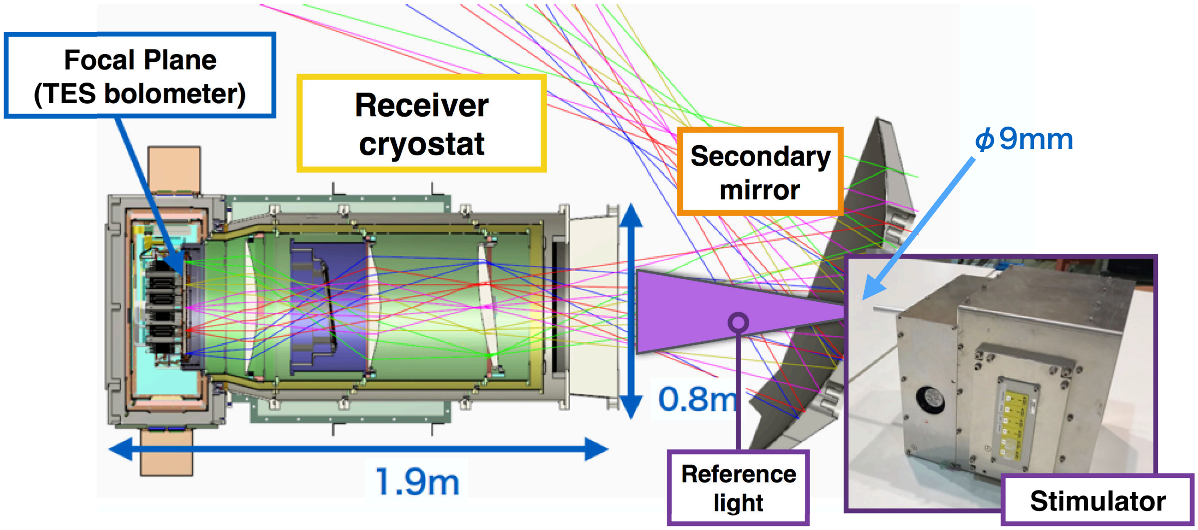

Figure 37: Overview of the stimulator system. The stimulator is installed directly behind the secondary mirror of the telescope and emits unpolarized light to the receiver. The intensity of this light is stable, we can evaluate how much the bolometer response changes by observing the response of the bolometers to the reference signal.

4.5.1 Mechanical design

The design of the PB-2 stimulator is discussed in this section. A schematic image of the PB-2 stimulator is shown in Fig. 38 The stimulator is assembled into ∼ 20 cm cubic box. The size of the box is strictly limited by the space behind the telescope's secondary mirror. There are connectors and switches on the left and right faces of the casing and a service window on the back face. Fig. 45 show images during assembly. The box has two rooms: front and rear. The front room contains only a motor and cooling fan, and the rear room includes a heater and the others. The reason to have two rooms is the motor should be cooled considering the life of the motor, but the heater shouldn't for temperature stability. The heater, inner cover, and support parts are assembled into a "heater unit." The heater unit has a double-layered structure to improve the stability of heater temperature and heat holding capability. It is accessible from the backside of the stimulator. Since the heater is generally used for a year continuously, it is a consumable item, and this design was adopted so that anyone can easily replace the heater parts. By preparing spare cartridge heater parts in advance, when the heater fails, they can be replaced quickly, for example, during the cooling cycle.

Jigs to settle the stimulator to secondary mirror is specially designed. The stimulator is attached as shown in Fig. 39.

The control components are assembled in a multi-purpose, 19-inch module box (2 units), and the box is mounted in a comoving rack of the telescope. The AC and DC power supplies are mounted in the same frame.

To read the chopper position, an IR optical encoder[6] is attached to the stimulator. An encoder module and a signal transceiver are mounted on a printed circuit board. The board

---

[6] OMRON EE-SX1140

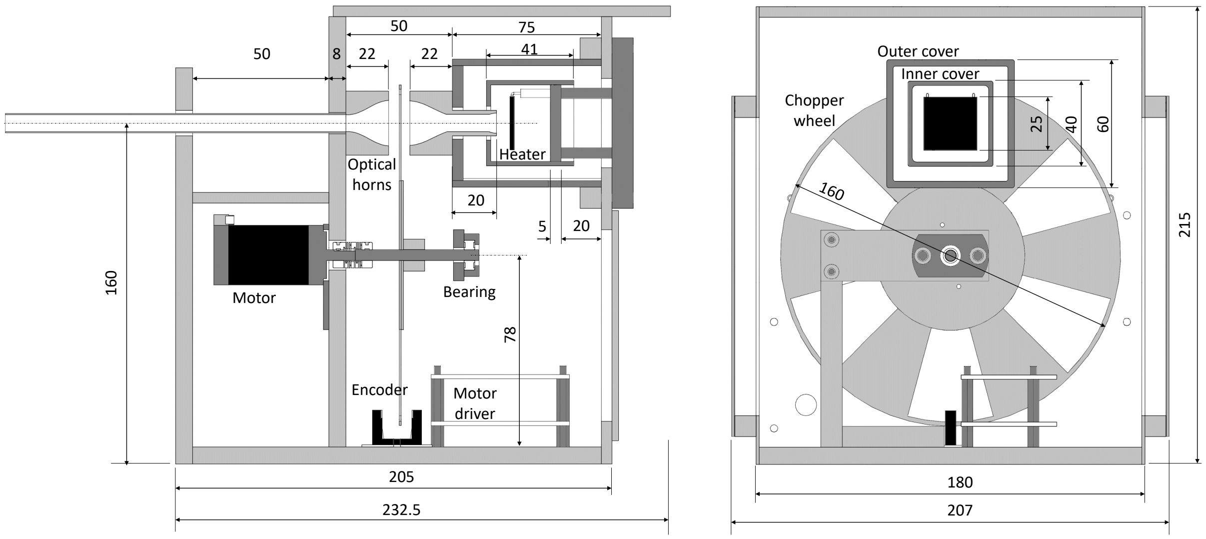

Figure 38: Cross-sectional image of the PB-2a stimulator. Image in two different planes is shown. Dimensions are shown in millimeters. (Left) in a plane parallel to the optical axis. (right) the plane perpendicular to the optical axis and include a heater.

is set inside of the stimulator casing. The transceiver transmits encoder output via a long (7 m) cable between the stimulator and its controller. The encoder records the chopper synchronized signal. The sensor's sampling rate is faster enough than the sampling rate of the bolometer timestream ($\sim$ 152 Hz).

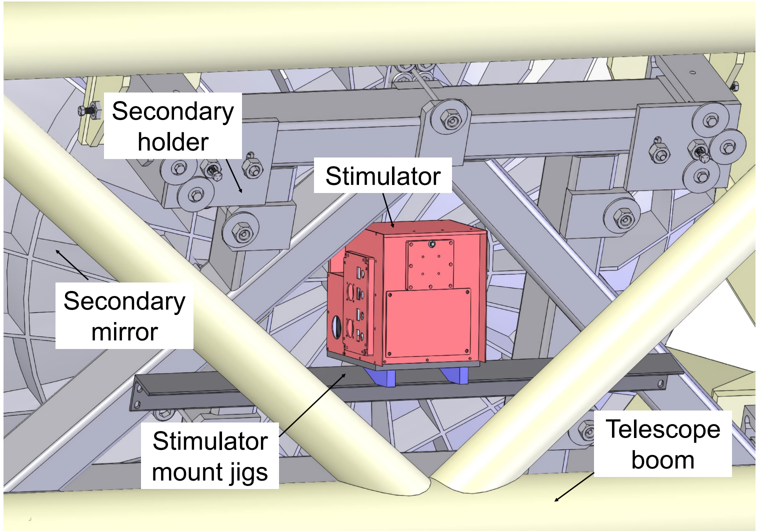

Figure 39: A CG image of how the stimulator is mounted on a telescope. The stimulator (painted in pink) is mounted on a base plate (dark gray). The base plate is attached to the insulating block (blue) and L-shape beam. The beam is bolted on the telescoping boom as well as the secondary mirror.

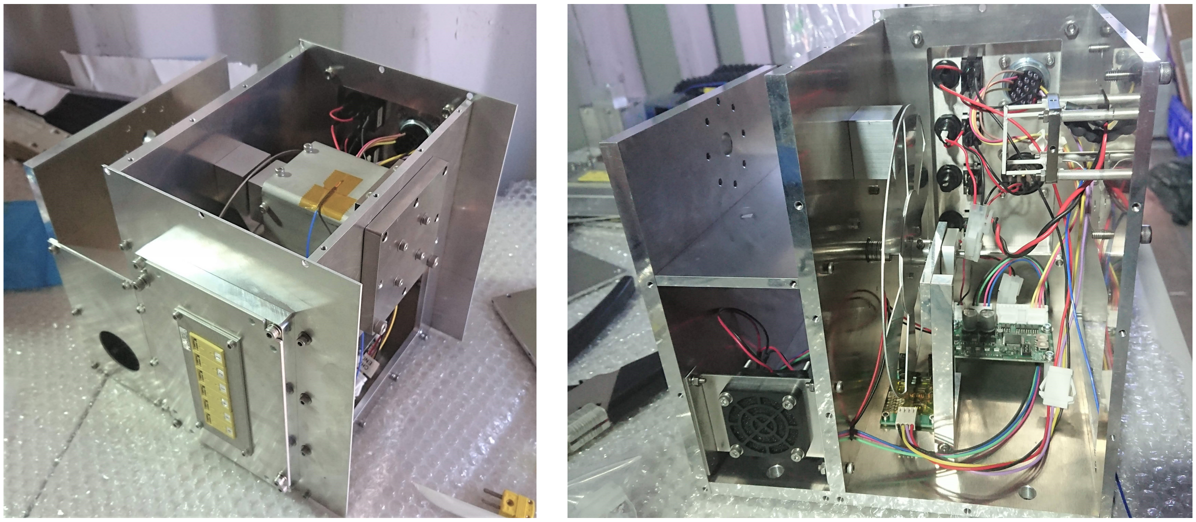

Figure 40: Photos were taken during assembly in the laboratory. (Left) top panel and service window are taken off. (Right) A connector panel is removed. In addition, outer and inner heater covers are removed to show the heater structure.

4.5.2 Control system

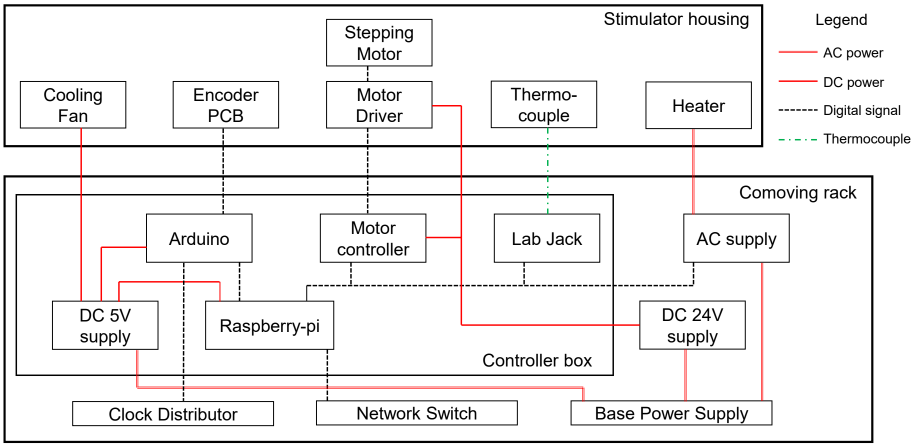

Figure 41: Connection diagram of stimulator controller. The controller box is installed inside the comoving rack of the telescope. Red (double/single) lines show (AC/DC) power cable, black dashed lines show digital signal (LAN and USB are included), and green chain lines show (K-type) thermocouple leads, respectively.

A diagram of the control system for our stimulator is shown in Fig. 41. A small onboard computer (raspberry-pi) is adopted for the control PC. It is used to control AC voltage supply, control the motor for chopper, communicate with ADC module (LabJack) for thermocouple readout, and transact slow control data to storage. The motor controller[7] communicates with the stepping motor driver, which locates inside of the stimulator box and finally converts the signal into the motor driving pulse. An onboard microprocessor (Arduino[8]) is used for chopper encoder readout because the fast response and continuous process are required. The Arduino board records every chopper timing according to the IRIG-B clock signal and sends data to the central control PC. The raspberry-pi controls the AC voltage supply for the heater via a USB-serial converter. The heater's nominal voltage is kept applied in regular operation even when the stimulator is not used. The AC supply's voltage, current, and power are constantly monitored from raspberry-pi. The LabJack reads thermocouples attached on four different points in the stimulator (heater, inner and outer cover of the heater parts, casing inner wall). Thermocouples and Labjack are connected with long compensation leads. Read temperatures are recorded in a specific interval at the slow control system.

4.5.3 Thermal source

Since PB-2 observes at two wavelengths, 90 GHz and 150 GHz, we needed a light source that could simultaneously cover a wide frequency band. Therefore, a blackbody radiation light source was adopted. We chose a ceramic (alumina) heater with $25 \times 25\text{mm}^2$ area[9] as a radiator for PB-2 stimulator because it has the most suitable size and high emissivity among commercially available heaters. It is uniformly heated up and is proven in PB-1 stimulator. (See appendix. **??**.) The effective stimulator temperature ($T_{\rm stm}$) is roughly approximated with $T_{heater} * (A_{\rm pipe}/A_{\rm beam})$, where $A_{\rm pipe}$ and $A_{\rm beam}$ are area of light pipe and beam spot size on mirror, respectively. Substituting them with design value, approximated $T_{\rm stm}$ turned out to be 100 mK. It is high enough unless optical efficiency from the heater to the pipe is devastating.

The source heater is hung at lead lines from the backplate, and hollow ceramic tubes support the leads. The heater can't be firmly attached to the structure. Otherwise, it will easily be broken by thermal expansion. Inner and outer covers surround the heater for thermal stability and heat prevention to other components. The nominal operating voltage of the heater is set at 40 V. The wattage of the heater is $\sim$ 31 W, and the temperature is $\sim$ 685 degC during stable operation. At higher voltages, the intensity of the source heater is greater, but the life of the source heater is shorter instead. The nominal voltage has been adjusted to account for this trade-off. The source heater has been in continuous operation for about two years so far.

---

[7] Oriental Motor EMP401

[8] Arduino Uno-R3, with Ethernet shield 2

[9] Sakaguchi MS-1000, maximum operation temperature 1000 deg C, maximum voltage 100V AC.

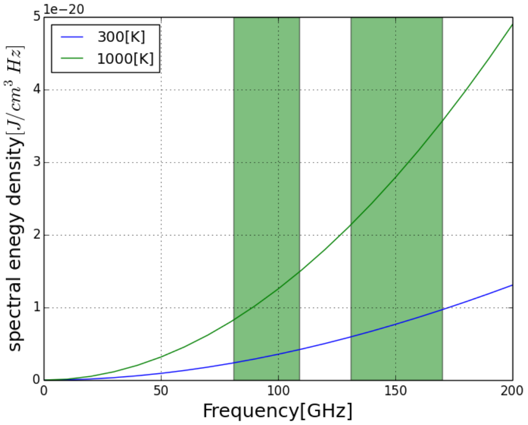

Figure 42: Since PB-2 observes at two wavelengths, 90 GHz and 150 GHz, we needed a light source that could simultaneously cover a wide frequency band. Green area shows the observation bands.

name	25mm ceramic heater MS-1000
size	$25 \times 25\text{mm}^2$
tempeature	1,000 degC Max
Wattege (room temperature)	89 W/cm^2
Voltage	120V
Life time (Approximate)	$>$ 10,000 hours (500 degC), $>$ 1,000 hours (1000 degC)

Table 11: Heater spec. Information is official manufacturer's data [62].

4.5.4 Optical design

The basic idea for the optical system is to maximize the received optical power by the detectors, under the condition of limited available inner-diameter on the secondary mirror (9 mm in diameter). A crucial requirement is that a modulator (mechanical chopper) is needed between the heater and output nozzle. We use a straight aluminum pipe with the maximum thickness (8mm inner diameter), the gap for the chopper to make as narrow as possible, and optical horns, Winston cone horn at the heater and both sides of the gap, as shown in Fig 43. The Winston Cone horn is a compound parabolic concentrator (CPC) that can concentrate light incident at a specific range of angles. It is suitable for focusing broadband of frequencies. See appendix. With the horns at the chopper, the ray at the gap is more concentrated, so the transmittance efficiency is to be better. On the other hand, a more oversized chopper wheel is required because of the larger aperture. It was designed to have a 16mm diameter aperture considering above trade-off [10]. The horn facing the heater is optimized to be 10 mm aperture, maximally utilizing the area of the source heater.

---

[10] There is only one free-parameter (diameter of the larger side aperture) for Winston cone horn when that of, the smaller gap is fixed to a particular value (8 mm: the same as the pipe).

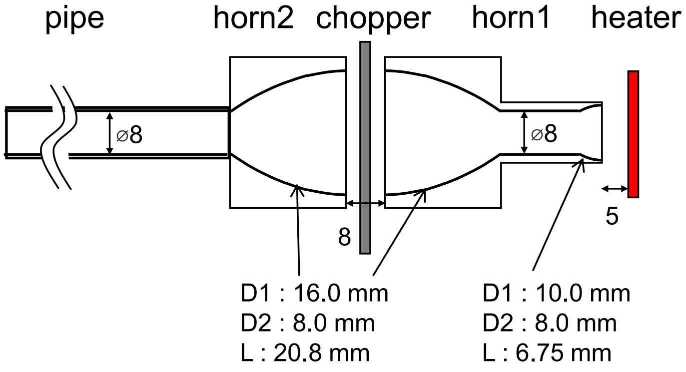

Figure 43: Design for the internal optical system of stimulator. We use a light pipe and optical horns. The gap for the chopper to make as narrow as possible. Winston cone horn at the heater and both sides of the gap. The figure is not scaled.

4.5.5 Modulation system

The modulation system mainly consists of a chopper wheel, a motor to drive the wheel, and an encoder to read the state of the wheel.

We adopted a rotation wheel chopper as a PB-1 stimulator, and the size is significantly larger, 160 mm in diameter (65 mm in PB-1). The number is 6, and this number was because it is as much number with the aperture of the horn is fully covered by one section of the chopper. This wheel is made of a 1 mm thick aluminum plate without an optical absorber on the surface to make the gap as short as possible. We adopt the stepping motor for flexibility in operation. A motor of ~ 0.2 Nm maximum torque [11] was chosen considering enough safety factors. The chopper wheel is connected to the motor via a flexible joint and ball-bearing supports on the shaft. The motor is driven by a driver circuit [12] which is mounted beneath the heater unit. The chopping frequency covers more than the Nyquist frequency (the sampling rate is about 152 Hz).

The flux function characterizes the progressive of the light. In the case the light horn is masked by the rotating chopper, the transmission of the light Φ is characterized as follows,

$$\Phi(\theta) = MS(\theta) \tag{108}$$

Where $\theta = \omega t$, ω is the constant angular velocity of the wheelis, M is the brightness and $S(\theta)$ is the uncovered fraction of the beam area.

$$S = \pi r^2 - \left(\beta r^2 - \frac{\overline{B_1 B_2} \times \overline{CU}}{2}\right), \tag{109}$$

where,

$$\overline{CU} = R\sin(\delta - \theta) = r\cos\beta \tag{110}$$

$$\overline{B_1 B_2} = 2\overline{CU} \times \tan\beta. \tag{111}$$

---

[11] oriental motor PKP225

[12] oriental motor CVD215

with $\sin\delta = r/R$, $\overline{CT} = r$ is the radius of the wheel. Then the area of the surface that is not covered by the wing is given by

$$S(\beta) = r^2\left(\pi - \beta + \frac{\sin 2\beta}{2}\right), \tag{112}$$

Where $\beta \in [0, \pi]$ for $\theta \in [0, 2\delta]$, and

$$\beta(\theta) = \arccos\frac{\sin(\delta - \theta)}{\sin\delta}. \tag{113}$$

In PB-2, the horn semi diameter $r = 8\,\mathrm{mm}$, $R = 62\,\mathrm{mm}$. And chopper encoder is attached to the opposite side of the horn as Fig. 38.

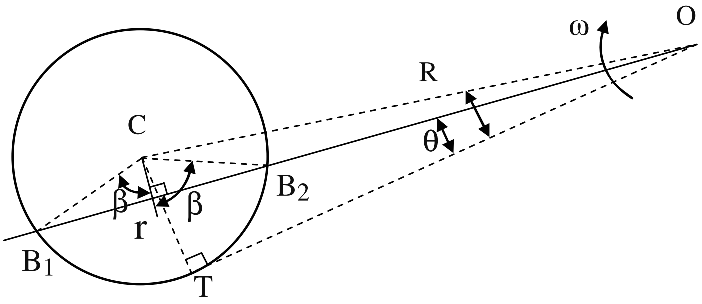

Figure 44: A schematic diagram of the horn and the chopper. This figure is taken from [63].

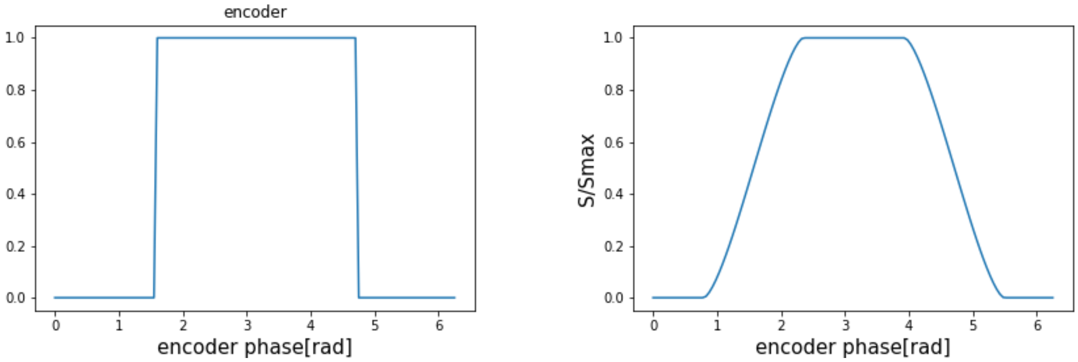

Figure 45: Beam simulation. (Left) The encoder signal. The encoder is attached to the opposite side of the light pipe. (Right) A covered area of the section of the light pipe beam.

4.5.6 Hardware operation

The sequence of the stimulator calibration is controlled from SA main control PC as well as CMB observation and other calibration such as planet observation [64]. The stimulator dedicated scripts also work for control chopper motor via site Ethernet to start data taking. The raspberry-pi transmits the signal into the motor controller with a serial transmission protocol.

The AC voltage supply [13] for the heater source is always kept at the nominal value unless the planned power outage is for maintenance. The voltage is also controlled from raspberry-pi. The voltage is gradually ramped up and down, considering the thermal stress of the heater [14]. The temperature of each point of the stimulator is continuously monitored with K-type thermocouples. The thermocouples readout with multi-purpose logger[15] which is connected to raspberry-pi, and the heater and temperature logs are sent to the slow-control system periodically. The discussion of temperature stability is in the performance study section.

The IR optical encoder detects when the chopper is open and closed. An Arduino records the timing according to the clock (IRIG-B) signal, which is provided as a standard clock. The array of timing when the chopper opens and closes is sent to a database. The intrinsic stability of chopping is 10 microseconds, and the overall spread is better than 1 ms in RMS, which is dominated by the space in mechanical imperfection.

4.5.7 Signal analysis

The TES time-ordered data is processed with a high pass filter and baseline subtraction at the beginning of data analysis. Then we chunk and stack the bolometer time-ordered data with encoder timing information to make averaged waveform. Finally, the amplitude of the modulated signal from the stimulator is estimated by fitting the averaged waveform. Analysis procedure is shown in Fig. **??**. As seen in 4.5.5, the shape of the waveform is approximately square wave We use a series of sinusoidal functions,

$$A(\theta) = \sum_{n=1}^{7} A_n \sin(n\theta + \phi_n) \tag{114}$$

for describing the waveform and fitted A_1 is inferred as the chopping amplitude.

4.5.8 Normal calibration run

In the typical calibration run, The chopper is driven in seven different frequencies [16] from the lowest to higher (Fig. 46). The frequencies are chosen referring to the set in PB, not to collide with any other known modulation and noise frequencies (and their harmonics).

---

[13] Kikusui PCR500M

[14] The supplier recommended values are 100 (K/min) in rising, 200 (K/min) in lowering

[15] LabJack U6 PRO

[16] 5, 9, 13, 19, 29, 37, and 44 Hz

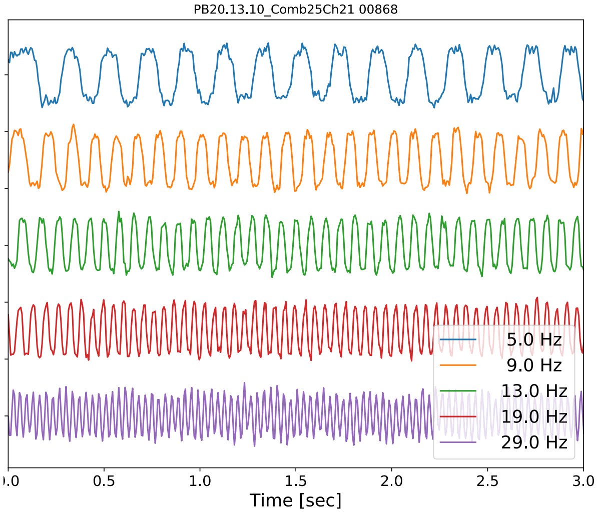

Figure 46: Time-ordered data example in one bolometer. In the typical calibration run, The chopper is driven in seven different frequencies.

4.5.9 Time constant

We use a one-pole time constant model for fitting the collection of stimulator amplitude for various frequencies. For well fabricated and properly tuned TESs, achieved resolution of time constant $\delta\tau$ is typically $0.02\,\mathrm{ms}$ for $\tau \sim 1\,\mathrm{ms}$ (close to design) case. It is cross-checked with the point source (planet) scan result. The source is seen shifted due to the time constant delay, depending on which direction the telescope is scanning. Both results show consistent results within the resolution. The changing of chopper frequencies enables us to measure the time constant of the bolometer. We use a one-pole time constant model for fitting the collection of stimulator amplitude at many frequencies. For $A(f)$ the response at some frequency, A_0 the detector gain, τ the bolometer time constant the one-pole model is

$$A(f) = \frac{A_0}{\sqrt{1 + (2\pi f \tau)^2}} \tag{115}$$

An example of the fitting of each bolometer response for each frequency is shown in Fig. 47 The bolometer responsivity is fit well by a one-pole model for which the reduced χ^2 is ~ 1.

4.5.10 Constant frequency run

The stimulator is also available as a constant reference source in calibration runs, such as engineering scan tests, planet scans, etc. The TES's gain can be monitored by extracting continuous stimulator signals from time-ordered data from the TES. In these runs, the chopper is continuously driven at a fixed (usually 5 Hz) frequency, and the pure stimulator signal amplitude could be extracted by filtering the time-ordered data.

H

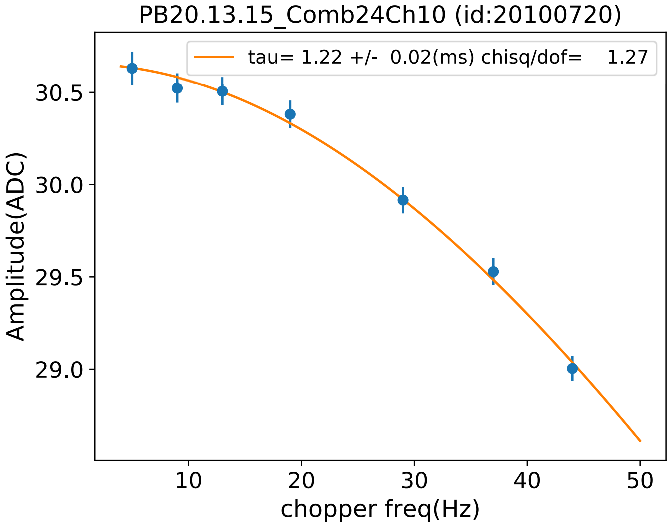

Figure 47: A demonstration to measure the time constant on a typical TES at the observation site. The time constant is estimated by fitting with the single heat capacity model.

At first, the TOD is high pass filtered to remove low-frequency fluctuation. Then demodulation is applied using the chopper-synchronized waveform. Finally, the waveform is low-pass filtered for smoothing.

5 Stimulator performance

After installation of the stimulator onto the telescope, the basic performances of the stimulator was evaluated in the early commissioning tests. In this section, the measurement for signal intensity and stability of stimulator are mainly reported. This evaluation test was performed to confirm that the basic performance of the stimulator met the requirements.

5.1 Signal stability

5.1.1 Source temperature test

At the observatory site in Atacama, Chile, the outside temperature typically changes by about 10 K in a day. Since the instrument was not fully installed at the initial test, the light source temperature strongly correlates with the outdoor temperature. Hence, to evaluate the stability of the source temperature, we adjusted the thermostat temperature to simulate the typical air temperature curve in the site and measured the temperature stability of the light source in the thermostat. Here, we evaluated the stability of the source temperature to changes on outdoor air temperature. Under the simulated air temperature change, the source temperature shifts within 3 K in one day. The stability of heater source is $\Delta T/T < 3$ K/1000 K $= 0.3\%$ at one day (Fig. 48). The coefficient of temperature change of the heater source ($\Delta T_{\mathrm{heater}}$ [K]) on outside air temperature change (ΔT_{air} [K]) were measured and found to be $\Delta T_{\mathrm{heater}}/\Delta T_{\mathrm{air}} \sim 0.21$.

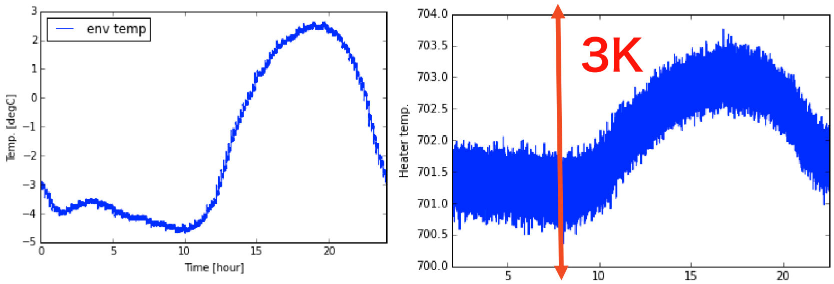

Figure 48: Lab test results. Under the simulated air temperature change, the source temperature shift within 3 K in one day. (Left) Simulated air temperature curve in thermostat. (Right) Measured heater temperature curve. The stability of heater source is $\Delta T/T < 3$ K/1000 K $= 0.3\%$ at one day.

During the commissioning at the observatory, time-ordered data of the source temperature acquired every 10 seconds for several data sets of 3 days to 2 weeks was obtained to evaluate the stability of the source temperature and the coefficients of the source and the ambient temperature ($\Delta T_{\mathrm{ambient}}$ [K]) (Fig. 49). The coefficients of source and ambient temperature are $\Delta T_{\mathrm{heater}}/\Delta T_{\mathrm{ambient}} = 0.34$. In the PB-1 experiment, the amplitude change in ambient temperature change during CES scans was typically 1–4 K. Therefore, a change in ambient temperature during one scan would affect the source temperature of 0.3–1.4 K, or $< 0.4\%$. This value satisfies the requirement for the stability of the source temperature ($< 0.65\%$).

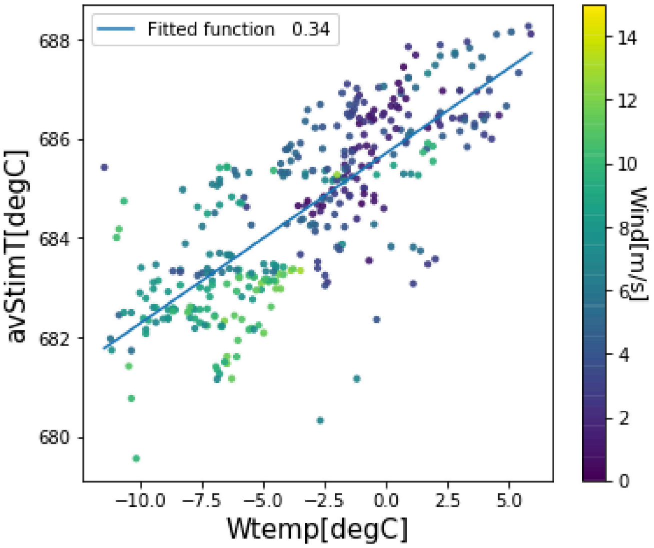

Figure 49: The data are correlated with the source temperature data and the telescope ambient air temperature. The data were obtained over a period of about 10 days during the commissioning at the observatory to evaluate the coefficients of source temperature and ambient temperature. The data interval per point is several hours. The coefficient of source temperature and ambient temperature is $\Delta T_{\mathrm{heater}}/\Delta T_{\mathrm{ambient}} = 0.34$.

Nextly, to check the change in the response of the bolometer output when the heater temperature varied, a test with the source voltage from 30 V to 50 V is also performed. The temperature of the stimulator source is changing from 770 to 950 K during the changing the voltage. As Fig. 50, the change in the bolometer responsibility is,

$$\frac{dg}{dT} = 0.15 \pm 0.01\,[\%/\mathrm{K}] \tag{116}$$

to the temperature of the stimulator source. Also, we checked the signal stability before and after CES scans. In consequence, the shift of the source temperature typically varies between -3 K and 3 K during one CES scan. It will affect the source temperature to Δg <0.45% at one CES scan.

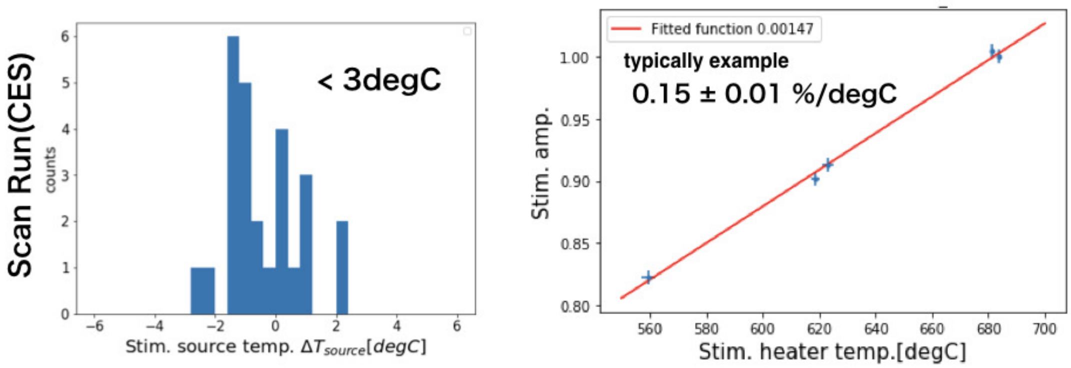

Figure 50: The results of the temperature stability test at the observatory. The shift of the source temperature typically varies between -3 K and 3 K during one CES scan. the responsivity is $0.15 \pm 0.01\%/\mathrm{K}$ to the temperature of the stimulator source.

5.1.2 Long term stability

Long-term stability of the source temperature at the observation site was confirmed. To improve the accuracy of the gain calibration of the bolometer, it is necessary to stabilize the heater temperature over one season of observations. For example, under no monitoring temperature conditions, the source temperature stability should be ¡0.03% during one season of observation, but in practice the source temperature is monitored. Fig. 51 shows the record of the heater temperature observation. The RMS of the heater temperature during one season was 1.7 K (0.17%), and the RMS excluding the seasonal variation was 1.0 K (0.10%). The average modulation for the day and night was 1.4 K (max.– min.). These are greater than the required values for the whole season under no monitoring temperature conditions. In observations, heater temperatures will be monitored and calibrated to meet stability requirements (less than 0.03%).

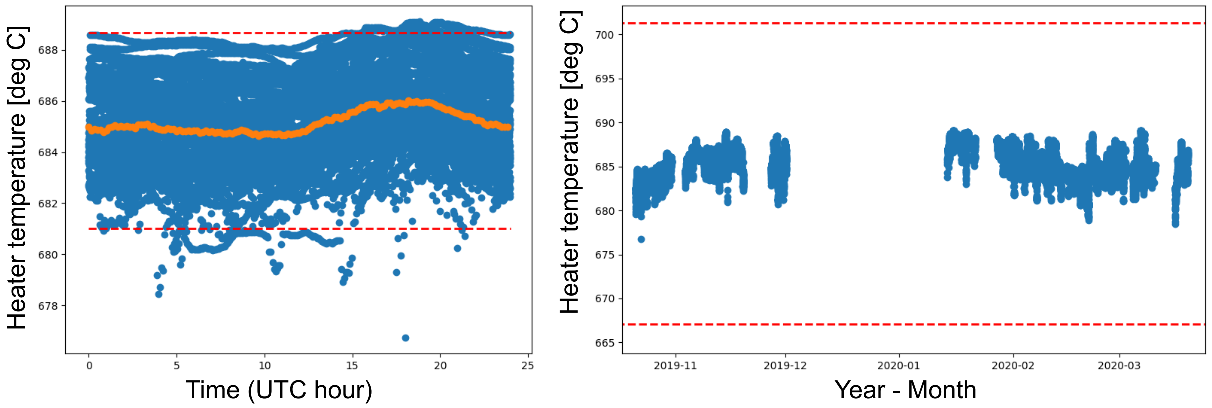

Figure 51: (Left) The observed heater temperature stacked in the 24-hour range. The average is shown in the orange marker, and the day-night variation is seen. The red dashed lines indicate a width of 1% power modulation within a CES period. (Right) Temperature after last heater modification. The red dashed lines show the width of the requirement of 4% power modulation during the whole observation season. The periods with missing radial region on data are periods when there was generator trouble and the periods closed due to the COVID-19.

5.2 Stimulator signal intensity

5.2.1 Planet measurements

The intensity or effective temperature of the stimulator is determined by observing a planet with a known antenna temperature and comparing their intensities. The effective temperature is used in units converted to CMB temperature. The gain g_c [ADC/$\mathrm{K_{CMB}}$] could be reconstructed from the the observed signal intensities of planet and the stimulator, and with telescope beam size. We had stimulator effective temperature measurements during the planet scan and part of the receiver alignment test. For simplicity, the planet is approximated as a point source with brightness temperature T_p. This is because the angular diameter of the planet is sufficiently small (typically 15–50 arcsec) relative to the beam of each bolometer (typically 3.5 and 5.2 arcmin).

Our scanning strategy is to scan az direction wide enough that all bolometers in the corresponding rows can see the planet, repeating scans changing relative el angle from the boresight and the target planet. As we adopt too wide (2 arcmin) interval of elevation angle to see whole beam profile of the planet, an elliptical Gaussian model is used to fit the beam map data using the planetary TOD data in the practical analysis.

A measured map on the sky $m(\theta, \phi)$ from the TOD data in units ADC counts can modeled as,

$$m(\theta, \phi) = \int d\theta' d\phi' B(\theta - \theta', \phi - \phi') T(\theta', \phi') \tag{117}$$

where $T(\theta, \phi)$ is the temperature on the sky, and $B(\theta, \phi)$ is the beam profile function in units of ADC counts per K $\cdot$ str. Assuming the planet as a point source,

$$T(\theta,\phi) \sim \delta(\theta)\delta(\phi)T_p\Omega_p \tag{118}$$

where $\delta(x)$ is the Dirac delta function, T_P is the temperature of the planet and Ω_p is the solid angle of the planet. Substituting $T(\theta,\phi)$ in Eq. (117) with Eq. (118),

$$m(\theta,\phi) = B(\theta,\phi)T_p\Omega_p. \tag{119}$$

The gain factor g_c can be expressed as a function of the measured beam map m and the parameters T_p and Ω_P of the planet. g_c is written as,

$$g_c = \int d\theta d\phi B(\theta,\phi) = \frac{\int d\theta d\phi m(\theta,\phi)}{T_p\Omega_p}. \tag{120}$$

We fit TOD data with an elliptical Gaussian model. The model used is,

$$m(x,y) = A_p \exp\left[-\left(a(x-x_0)^2 + 2b(x-x_0)(y-y_0) + c(y-y_0)^2\right)\right]. \tag{121}$$

Here

$$a = \frac{\cos^2\theta}{2\sigma_x^2} + \frac{\sin^2\theta}{2\sigma_y^2} \tag{122}$$

$$b = -\frac{\sin 2\theta}{4\sigma_x^2} + \frac{\sin 2\theta}{4\sigma_y^2} \tag{123}$$

$$c = \frac{\sin^2\theta}{2\sigma_x^2} + \frac{\cos^2\theta}{2\sigma_y^2} \tag{124}$$

where A_p is the amplitude of the planet. This expression is then used as a representation for the beam, and its integral can be performed analytically,

$$g_c = \frac{2\pi A_p\sigma_x\sigma_y}{T_p\Omega_p} \tag{125}$$

The receiver alignment is now in the final stage, and the measured beamwidth is 5.2/3.5 arcmin in FWHM for 90/150 GHz, which is almost exactly as designed (5.2/3.4 arcmin). It is also confirmed that the beam is focused at both frequencies and on all wafers (Fig. 52, Fig. 53). The optical yield from the planet observation is consistent with the optical yield of the stimulator. It will be described in a later section.

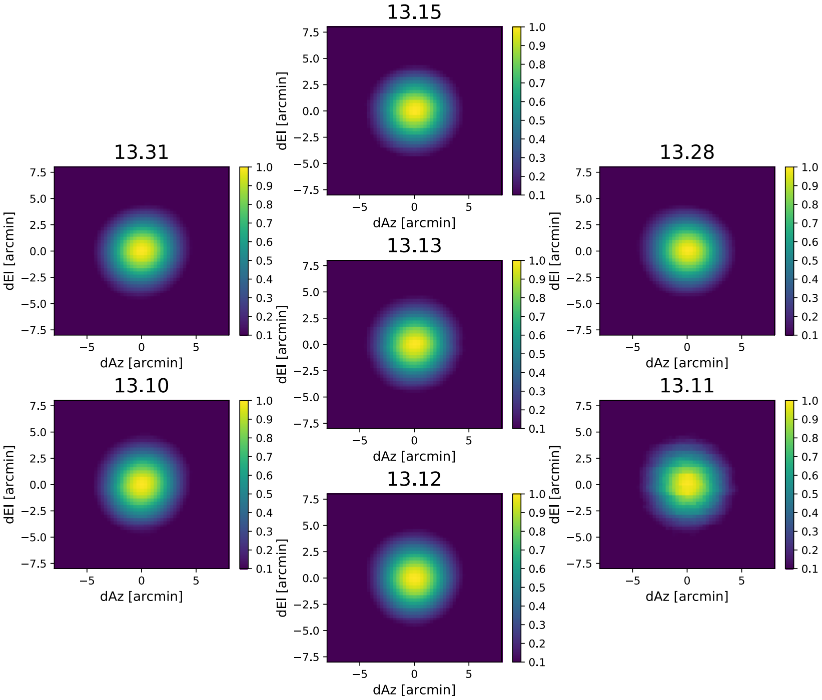

Figure 52: The coadding planet maps from all bolometers of each wafers in 90 GHz. The averaged beamwidth is 5.2 arcmin in FWHM.

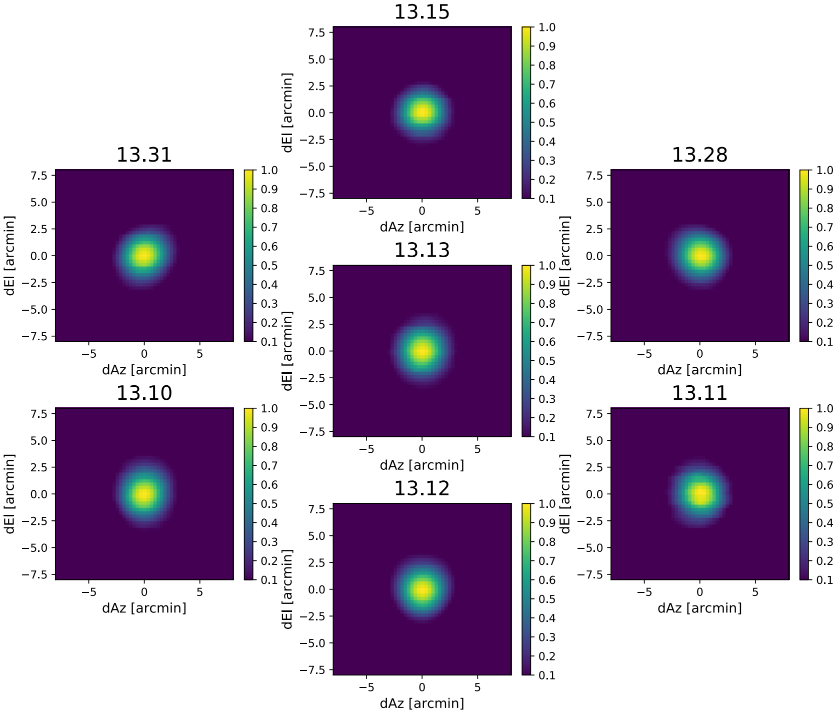

Figure 53: The coadding planet maps from all bolometers of each wafers in 150 GHz. The averaged beamwidth is 3.5 arcmin in FWHM.

5.2.2 Effective temperature of the stimulator

While scanning the planet, we simultaneously input the modulation signal from the stimulator. The stimulator amplitude can directly be compared with the intensity of the planet with that operation. We measured several planets in the commissioning test; we use Jupiter of $T_p = 173.6\ \mathrm{K_{CMB}}$ at 147 GHz and $T_p = 172.3\ \mathrm{K_{CMB}}$ at 100 GHz [65] as an antenna temperature. The effective temperature of the stimulator is calculated from the stimulator signal intensity as $T_{\mathrm{stm}} = A_{\mathrm{stm}}/g_c$. A_{stm} is the amplitude of the modulation signal of the stimulator.

The effective temperature of the stimulator across the focal plane is $44 \pm 7\,\mathrm{mK_{CMB}}$ at 90 GHz and $63 \pm 15\,\mathrm{mK_{CMB}}$ at 150 GHz, where 1σ spread on the focal plane is shown as an error (Fig. 54). The measured effective temperature fills the requirements ($> 3\,\mathrm{mK}$) over the entire focal plane. We will calibrate the final number of absolute effective temperatures of the stimulator with the CMB spectrum (comparing with C_l^{TT}).

The effective intensity of the light source varies across the focal plane in the range of about 35–85 mK. It was confirmed for the focal plane bolometer that the signal was more significant than PB-1 signal, $15\text{–}43\,\mathrm{mK_{CMB}}$ [66] at two observation frequencies. For performing gain calibration, the effective template of the stimulator is computed for each channel.

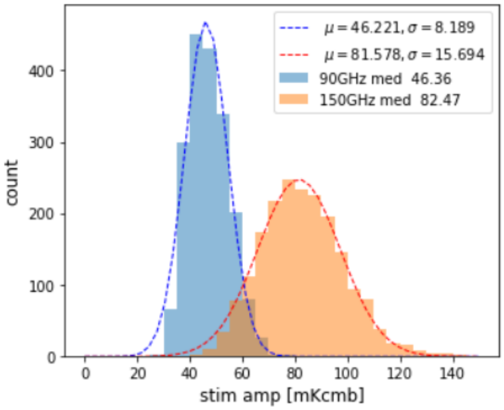

Figure 54: The effective temperature of the stimulator for each bolometer. The effective temperature of the stimulator across the focal plane is $44 \pm 7\,\mathrm{mK_{CMB}}$ at 90 GHz and $63 \pm 15\,\mathrm{mK_{CMB}}$ at 150 GHz, where 1σ spread on the focal plane. The effective temperature fills the requirements ($> 3\,\mathrm{mK}$) over the entire focal plane.

5.3 Performance summary

All the requirements are validated in discussion in this section, as listed in table 12.

Requirement item	measurement value
signal effective temperate T_{stm}	$46 \pm 8\,\mathrm{mK_{CMB}}$ (90 GHz) / $82 \pm 17\,\mathrm{mK_{CMB}}$ (150 GHz)
signal stability	$< 0.4\%$ (CES), $\sigma_T = 0.17\%$ (season)

Table 12: Summary of measured characteristics of stimulator. The signal effective temperate and stability met the required value on the table **??**.

5.4 Detector characterization

5.4.1 Optical yield from stimulator

To investigate the optical yield, we evaluated the response of the bolometer to the stimulator signal. As a result, we confirmed the signal from the stimulator in 4800 channels (about 60%) in the combined frequency bands of 90 GHz and 150 GHz. This result is consistent with the yield of the bolometer from planetary observations mentioned earlier. The optical yield is as high as 70% if we exclude the dark channels for calibration and the channels with only resistors connected.We observed that about 99% of the bolometers that were successfully tuned responded to the signal from the stimulator. Due to the multiplexed readout, the broken multiplexer unit can be observed as a group of missing parts on the hexagonal wafer (Fig. 55).

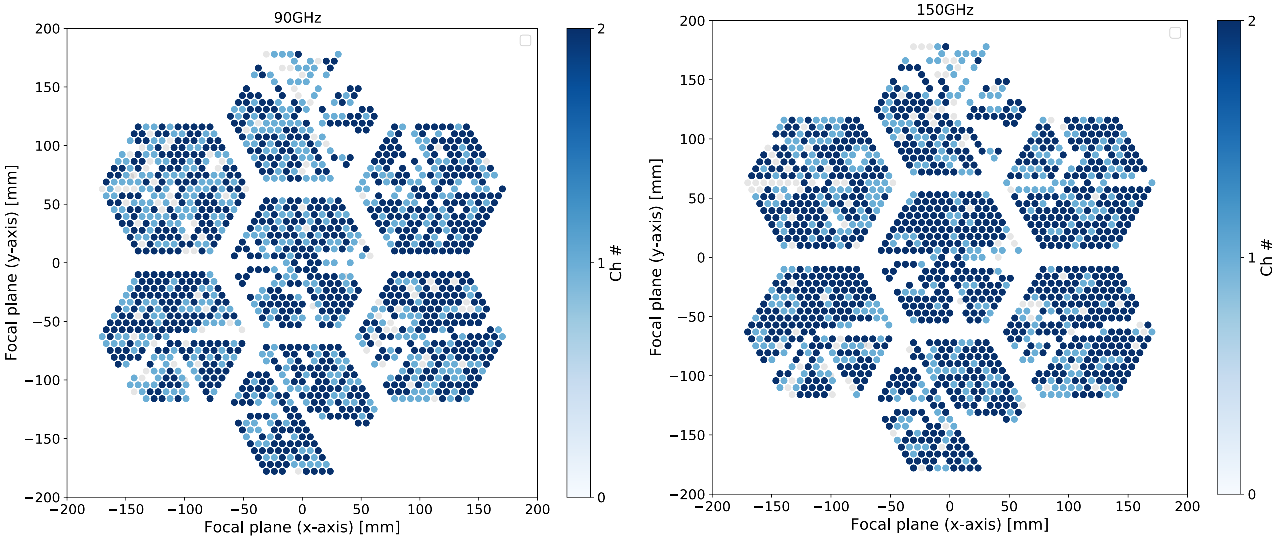

Figure 55: Preliminary optical yield in commissioning. We can measure at least once 2018 bolos (90 GHz), 2095 bolos (150 GHz). Color shows the number of active channels per pixel. Entry: 2591 bolos (90 GHz), 2749 bolos (150 GHz), total number is including unlabeled frequency band yet.

5.4.2 Time constant measurements

The heater source of the stimulator is chopped at various frequency steps, and the response of the bolometer at each frequency step is checked. The relative gain and time constant values of thousands of bolometers in both observation bands are obtained (Fig. 56). These values are also a preliminary result before optimizing the tuning of the bolometer. We dropped the bolometer resistance to a point where the ratio R_{frac} to the resistance at normal conduction was less than 0.7. We evaluated the time constant of the bolometers at $R_{\text{frac}} < 0.7$. The time constant was confirmed to be almost the same as the design value of 1 to 5 msec.

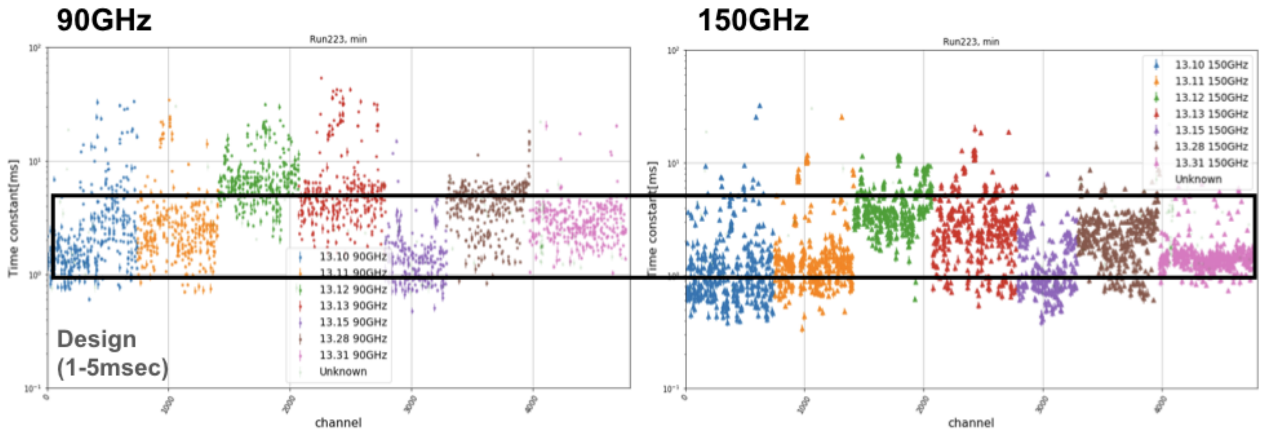

Figure 56: The evaluated time constant of the bolometer using the stimulator signal. We checked the bolometer that could be dropped to the bias point enough. The time constant was confirmed to be almost the same as the design value of 1 to 5 msec.

6 Future prospects

As discussed in Sec. 3, gain uncertainty causes leakage from the unpolarized signal to the polarized signal. Therefore, the gain uncertainty must be sufficiently lower than the statistical sensitivity of the PB-2 observation to reduce the statistical uncertainty of the tensor-to-scalar ratio r. This section discusses the accuracy of r achieved by future gain calibration precision estimated from measured data during commissioning.

6.1 Gain calibration precision

The current gain calibration precision in commissioning tests is 0.3% (90 GHz) and 0.2% (150 GHz) per observation (Fig. 57). Here, the gain calibration precision is based on the ratio of the gain to the statistical error obtained by fitting the response to the stimulator signal with a one-pole model, as explained in Sec. 4.5.9.

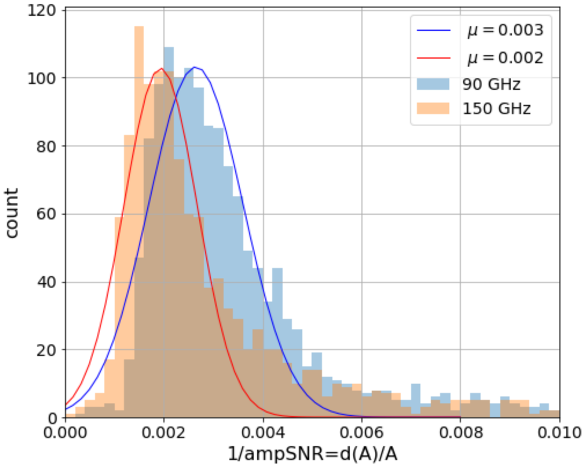

Figure 57: The current gain calibration precision in commissioning tests. The current gain calibration precision is 0.3% (90 GHz) and 0.2% (150 GHz) per observation. Here is a typical example of one stimulator measurement results.

Fig. 58 shows the correlation between gain calibration precision and noise for the same data set as in Fig. 57. Here, the effective temperate of the stimulator obtained in Sec. 5.2.2 is used to convert to $NET_{\mathrm{bolo}}\,[\mu\mathrm{K}\sqrt{\mathrm{s}}]$. The gain calibration precision improves as the noise level of the detector decreases, as seen in Eq. (75). Also, as seen in Eq. (76), it is expected that the stability of the heater source $\frac{\sigma_{T_{\mathrm{stm}}}}{T_{\mathrm{stm}}}$ limits the gain calibration accuracy in the region of sufficiently low noise levels. From the signal stability evaluation test in Sec. **??**, the signal stability is less than 0.45%. In Fig. 58, the gain calibration accuracy prediction curves for signal stability of $\frac{\sigma_{T_{\mathrm{stm}}}}{T_{\mathrm{stm}}} = 0.5\%, 0.1\%, 0.01\%$ are drawn as solid lines.

This data was obtained during the commissioning test, and the noise level should improve at future scientific observations. If the noise level is $360\mu\mathrm{K}\sqrt{\mathrm{s}}$, which is equivalent to the design value, and the signal stability is 0.5%, the gain calibration precision is expected to be 0.5% (90 GHz) and 0.5% (150 GHz). If the signal stability is 0.1% at $NET_{\mathrm{bolo}} = 360\mu\mathrm{K}\sqrt{\mathrm{s}}$, the gain calibration precision is expected to be 0.1% (90GHz) and 0.1% (150GHz).

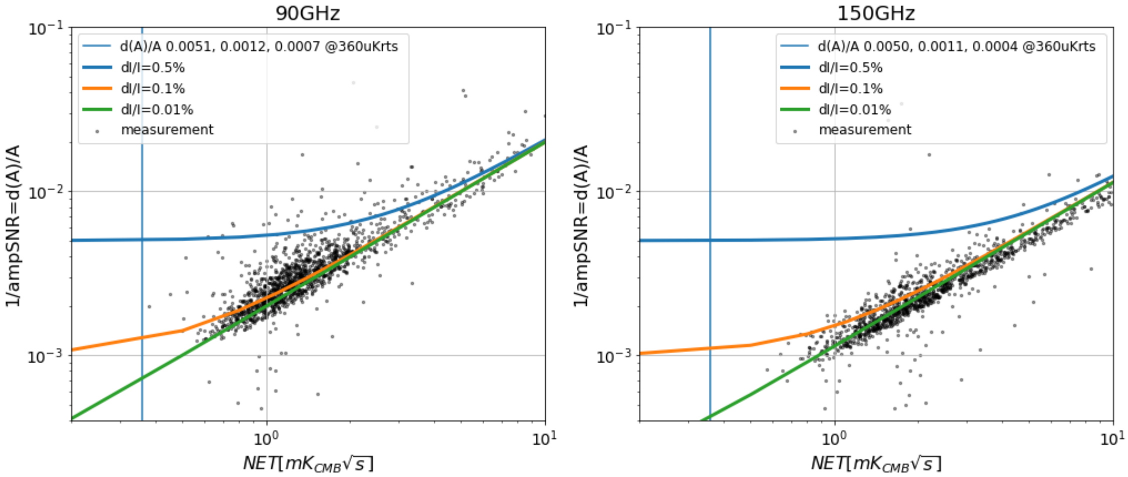

Figure 58: Scatter plot of relative precision of the gain (y-axis) versus noise (x-axis). The scatter points are the ratios of the gain and the gain error for each channel which is measured by the stimulator. The noise is defined as the white noise value converted by the effective temperature of the stimulator's signal. The measured gain model used to estimate the required values and the actual measured values agree. If $\frac{\sigma_{T_{\rm stm}}}{T_{\rm stm}} = 0.1\%$ and $NET_{\rm bolo} = 360\mu{\rm K}\sqrt{\rm s}$, the gain calibration precision is expected to be 0.1% (90GHz) and 0.1% (150GHz).

6.2 Impact of the stimulator on power spectrum measurements

The Fisher matrix method estimates the statistical uncertainty of r, $\sigma_r(r=0)$ (one-sigma limit for $r=0$) [67], as follows,

$$\sigma_r(r=0) = \left[\sum_{\ell=\ell_{\rm min}}^{\ell_{\rm max}} \left(\frac{C_l^{BB}(r=1)}{\Delta C_l^{BB}}\right)^2\right]^{-1/2} \tag{126}$$

where $l_{\rm min}$ and $l_{\rm max}$ are the minimum and maximum multipole moments given by the PB-2 measurements condition. The observational efficiency is assumed to be 18%, the sky coverage $f_{\rm sky}$ is assumed to be 2% [68], f_1 is assumed to be 1. Systematic error from gain uncertainty $\Delta C_l^{BB} = \Delta G^2 f_1 \star C_l^{TT}$ is come from Table. **??**. Power spectrum C_l^{BB} at $r=1$ is computed by CAMB[17] (Planck 2018 [12]). Assuming a large patch scan, we performed simulations to evaluate the systematic error of $\sigma_r(r=0)$ due to the gain uncertainty. The systematic error associated with the uncorrected gain is sufficiently small that the PB-2 can obtain a better sensitivity with correction in Fig. 59.

---

[17] https://camb.info

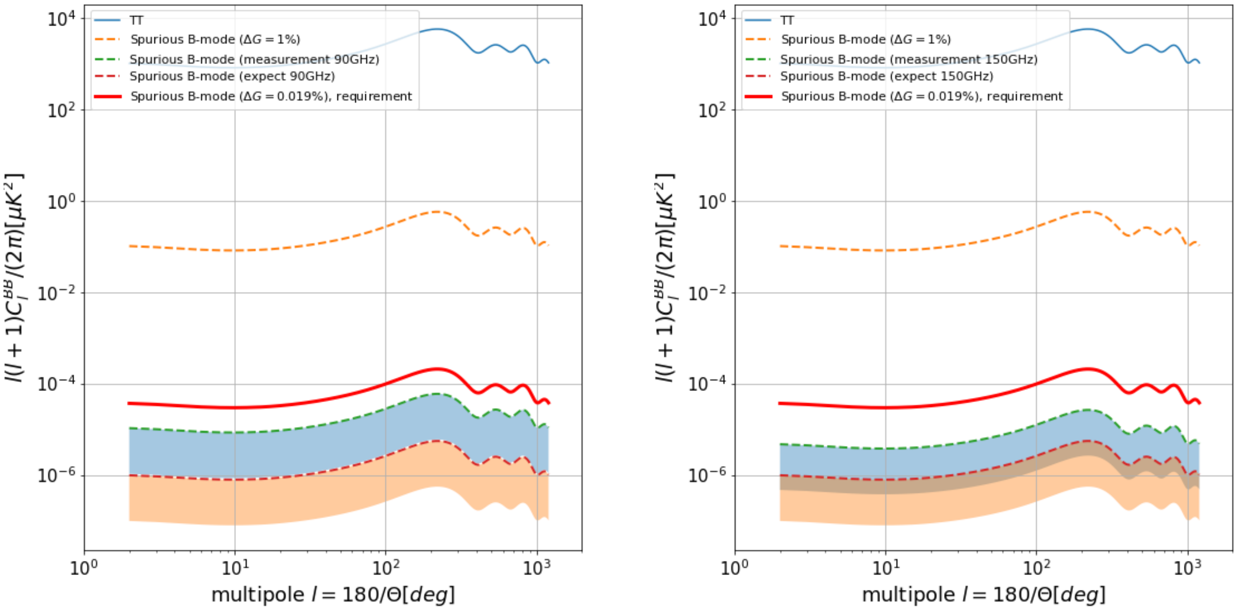

Figure 59: The lines with red shows the requirement value for the PB-2 sensitivity discussed in Sec.3. The lines with green dashes show the measurement results under the commissioning test in Sec. 6.1. The shaded areas correspond to the sky strategy ($0 < f_1 < 1$). The line with red dashes corresponds to the calibration precision when the noise level is as the design value of the experiment ($360\,\mu\mathrm{K}\sqrt{\mathrm{s}}$). I assumed 600 CES observations are taken and 1,800 pixels per observation per frequency band for averaging. (left) 90 GHz, (right) 150 GHz. Systematic error suppression by calibrating the gains for each observation.

Fig. 59 shows the gain calibration precision evaluated under the current commissioning test in Sec. 6.1, and the gain calibration precision will be further improved. In addition, $f_1 < 1$ will be conservative [30].The relationship between gain calibration precision and σ_r is shown in Fig. 60. The calibration precision of the gain for one bolometer per observation is expected to be 0.1% with improving noise level. Assuming 1,800 pixels per observation per frequency band, the relative gain calibration precision per observation is about 2.0×10^{-3} % when the noise level is as the design value of the experiment. The measurement error with respect to r is σ_r(r=0) $< 2.3 \times 10^{-4}$. σ_r(r=0) $< 1.5 \times 10^{-5}$ is expected when the noise level is equivalent to the design value, since the gain calibration precision is improved by improving the noise level. Here I assume that the gain is changing ideally slowly and linearly during the observation. Since there are about 600 CES observations in a season, the gain calibration precision for the whole season should be better than this, and it would be small enough. The gain calibration precision throughout the season will depend on the scan strategy and how the gain changes during CES observations. Future observations will estimate it. Consideration of the scan strategy and the way the gain changes during CES observations are future tasks.

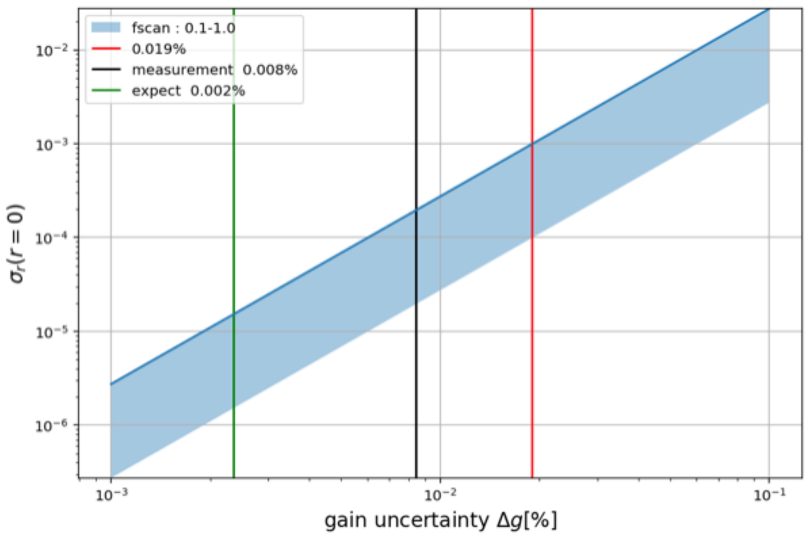

Figure 60: The relationship between gain calibration precision and σ_r. The precision will be further improved by improving the NET and determining the scanning strategy. The measurement error with respect to r is σ_r(r=0) $<$ 2.3 $\times$ 10^{-4}. σ_r(r=0) $<$ 1.5 $\times$ 10^{-5} is expected when the noise level is equivalent to the design value. The gain calibration precision throughout the season will depend on the scan strategy and the way the gain changes during CES observations, and will be estimated by future observations.

6.3 Future outlook

Much effort has gone into commissioning the first instruments in the PB-2. Further commissioning and characterization with the HWP installation are required before scientific observations start. The PB-2 will have completed its hardware performance evaluation, and it is expected to begin observations next year. The stimulator for the PB-2 can be widely applied to many future bolometers and multi-frequency CMB observation experiments. Future experimental extensions, Simons Array and Simons Observatory project, will increase the number of detectors by order of magnitude or more and observe in four different spectral bands to better control foreground contamination. In addition, the second telescope in the Simons Array will undergo integration testing next year and will observe cosmological patches with the PB-2 in the future. A third telescope is also planned, which is expected to complete the native dust monitoring channel of the Simons Array and enable the full scientific spectrum of the Simons Array project. It is compatible with the PB-2 and the Simons Array, Simons Observatory, and the stimulator will be used. This paper advances the effort to discover the primordial B-mode of the PB-2 by reducing the systematic error from the gain uncertainty. The systematic error of $\sigma(r = 0)$ due to the uncertainty in the gain measurement was evaluated. The systematic error associated with the relative gain is sufficiently small to provide better sensitivity. The first season of the PB-2 observations will show a robust systematic error control, which contributes to B-mode cosmology. In the future, a continuous gain monitoring method combined with HWP is being considered.This is worth considering in future integrated studies and the Simons Array.

7 Summary

The POLARBEAR-2 (PB-2) experiment will perform polarimetric observations of the cosmic microwave background radiation (CMB) on the ground. The PB-2 will install 7588 superconducting detectors (TES) to improve the statistical sensitivity, and simultaneous observations in two frequency bands, 90 GHz and 150 GHz, will help the separation of foreground radiation. After the three years of observations, the PB-2 will probe the inflationary model with a sensitivity of the tensor-scalar ratio $r < 0.01$ (95% C.L.). Since the B-mode signal will be faint, controlling the various systematic effects is needed. One of the primary systematic error sources is the fluctuation of the TES bolometer's responsivity, which is slightly fluctuating due to the temperature variations on the focal plane stage, the atmospheric instability.

An artificial calibration source, stimulator, has been developed for the PB-2 receiver system to calibrate the indefiniteness of gain and time constant, which are the significant systematic errors in the observations. The system adopted a thermal ceramic heater (1000K) as a blackbody radiator for covering up to full observation frequency bands. A frequency-independent reflective focusing horn enables simultaneous calibration at multiple frequencies. We installed this system behind the telescope's secondary mirror and made it coupled optically with the detectors through a light pipe penetrating the mirror. We can estimate the relative gain of the bolometers by monitoring the response to the stable optical signal from the stimulator. We can also estimate the time constants value of each bolometer with the modulated signal of the stimulator at various frequencies.

This paper mainly focuses on the gain calibration using the stimulator independently. I clarified the requirements for the equipment for gain calibration and calibration of time constant designed and developed the stimulator hardware. We need the signal intensity to be larger than 3 mK and the signal stability less than 0.65% (one CES).

The PB-2 receiver was disassembled and transported to the Chilean observatory in 2018. The instrument commissioning started in January 2019. The integrated evaluation test was performed at the observation site during the commissioning. The stimulator's measured effective temperature is 44 mK at 90 GHz and 63 mK at 150 GHz. The measured signal stability is less than 0.4% (one CES). I confirmed that the stimulator met the requirements for the relative gain calibration. We can estimate the time constants and obtain relative gains for thousands of bolometers with both 90 GHz and 150 GHz observation bands simultaneously. Also, the calibration system was applied in the integrated evaluation test of the optical system at the observation site and performed to an initial evaluation of the detector characteristics and the optical yield.

The gain calibration precision is expected to be 0.1% (90GHz) and 0.1% (150GHz) for each channel per observation when the noise level is the experiment's design value. The statistical uncertainty of r, $\sigma_r(\mathrm{r{=}0}) < 1.5 \times 10^{-5}$ is expected per observation, assuming that the gain is changing ideally slowly and linearly during the observation. Furthermore, we have demonstrated that the gain calibration with the stimulator can keep the significant systematic errors small enough to achieve the target sensitivity of the PB-2 experiment, which shows the feasibility of experimental verification of the inflation theory.

A Appendix

A.1 Gain calibration in the case with HWP

A.1.1 Gain monitoring with HWP

Noted the case with half-wave plate (HWP). When a linearly polarized wave with a polarization angle of ϕ incident on a rotating half-wave plate at $\theta_{\text{HWP}} = \omega_{\text{HWP}} t$, angle is roted by $2\theta_{\text{HWP}} = 2\omega_{\text{HWP}} t$ to the optical axis of the half-wave plate. Then, emitted at a polarization angle of $2\theta_{\text{HWP}} - \phi$. The emitted linearly polarized wave will rotate at $\theta_{\text{HWP}} = \pi$ as one roted, incident linearly polarized wave is modulated by $\omega_{\text{mod}} t = 4\omega_{\text{HWP}} t$ Therefore, the output is

$$V = G \cdot (T + \epsilon[Q \cos(4\omega_{\text{HWP}} t - 2\phi) + U \sin(4\omega_{\text{HWP}} t - 2\phi)]) \tag{127}$$

Thus, only the polarization components Q and U can be modulated. By setting the real part to Q and the imaginary part to U, the polarization component can be reconstructed from a single detector.

$$Q_{\text{out}}(t) - iU_{\text{out}}(t) = [Q_{\text{in}}(t) - iU_{\text{in}}(t)]e^{-i\omega_{\text{mod}} t} = [Q_{\text{in}}(t) - iU_{\text{in}}(t)]e^{-4i\omega_{\text{HWP}} t} \tag{128}$$

Since the polarization component can be reconstructed from a single detector, there is no need to calibrate the gain difference between the pair of bolometers.

A.1.2 Estimate T to 2f/4f leakage

Polarization signal caused by the asymmetry of the optical elements on the atmospheric side of the HWP is modulated through the HWP. In the PB2, the HWP is placed in front of the receiver, then the polarization signal generated by the surfaces of the primary and secondary mirror is considered to be modulated through the HWP. Assuming that the atmospheric fluctuations are δT_{sky} [K], the leakage coefficient is λ, and the $2f$ and $4f$ signals from the unpolarized light of each observation are $\delta A^{(2)}$ [K] and $\delta A^{(4)}$ [K], and considering the uncertainty of the polarization signal leakage is written as

$$\delta T_{\text{sky}} \delta\lambda \approx \frac{\delta A^{(2,4)}}{\sqrt{N_{\text{obs}}}}. \tag{129}$$

Rewriting the uncertainty of leakage as $\delta A^{(2,4)} = \delta g_{\text{bolo}} A^{(2,4)}$, Eq. (129) can be written as,

$$\delta T_{\text{sky}} \delta\lambda \approx \frac{A^{(2,4)} \delta g_{\text{bolo}}}{\sqrt{N_{\text{obs}}}}. \tag{130}$$

In the PB-1 it's estimate that $\lambda \sim 0.06\%$ [34]. Consider the case of calibration with an accuracy of $\delta\lambda < 0.01\%$,

$$\delta\lambda \approx \frac{A^{(2,4)} \delta g_{\text{bolo}}}{\delta T_{\text{sky}} \sqrt{N_{\text{obs}}}} < 0.01\%. \tag{131}$$

Assuming that 600 CES observations are taken in one season (one year), δg_{bolo} is written as

$$\frac{\delta g_{\mathrm{bolo}}}{g_{\mathrm{bolo}}} < 12\% \cdot \left(\frac{A^{(2,4)}}{0.1\,\mathrm{K}}\right)^{-1} \cdot \left(\frac{\delta T_{\mathrm{sky}}}{5\,\mathrm{K}}\right) \cdot \left(\frac{N_{\mathrm{obs}}}{600}\right)^{\frac{1}{2}} \tag{132}$$

$$\frac{\delta g_{\mathrm{bolo}}}{g_{\mathrm{bolo}}} = \frac{NET_{\mathrm{bolo}}}{T_{\mathrm{stm}}\sqrt{t}} < 12\% \tag{133}$$

The required temperature intensity is

$$T_{\mathrm{stm}} > \frac{360\mu K}{12\%\sqrt{120}} \sim 0.3\ \mathrm{mK}. \tag{134}$$

the required temperature stability in one CES is

$$\frac{\delta g_{\mathrm{array}}}{g_{\mathrm{array}}} \sim \frac{\sigma_{T_{\mathrm{stm}}}}{T_{\mathrm{stm}}} < 12\%. \tag{135}$$

A.2 PB-1 stimulator

A stimulator that we referred for the design in PB-2 was the one operated in PB-1 experiment. A schematic image of the PB-1 stimulator is shown in Fig. 61. The basic components are the same as that in the PB-2 except for an additional system for polarization rotation function.

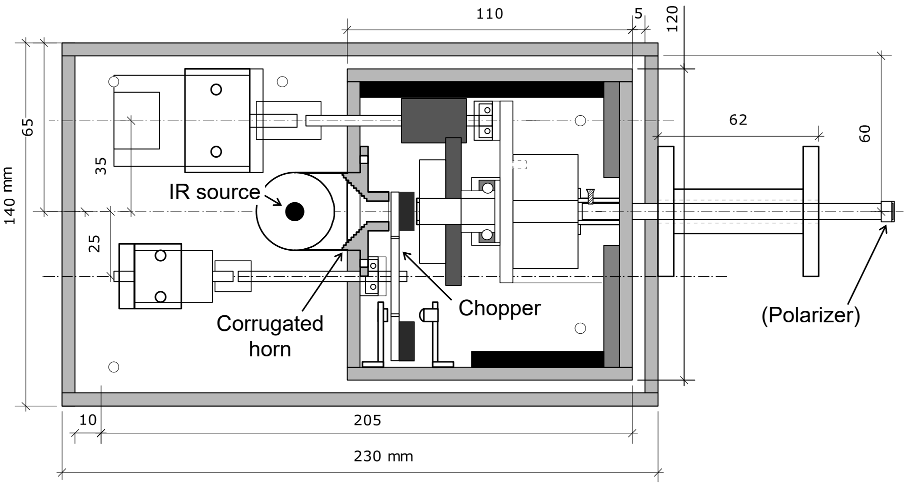

Figure 61: The stimulator used for PB-1. Radiation from IR source passes corrugated horn, chopper and pipe. Two motor and encoder systems are equipped: for each chopper and for polarizer.

The same type heater as the PB-2 (alumina plate) was originally adopted, but was replaced to a stick-shape, silicon nitride one, because the previous heater often had breakdown. The reason is now understood; due to ion migration by operation in DC, hence there is no danger to adopt it in the PB-2. The radiation from heater is collected by a corrugated conical horn which is optimized for 150 GHz. An optical chopper locates next to the horn. The chopper has 2 blades and made of aluminum plate with foam type black- body[18] applied on the receiver-side face. The chopper is driven by a low-torque stepping motor[19]. A wire-grid polarizer is set at the tip of the pipe of the stimulator. The pipe is driven by another stepping motor[20] via reduction gear so that the polarization angle could be controllable. The polarizer was used in the commissioning runs to investigate polarization properties, but unmounted in the CMB observations. The chopper is located in inner box inside of the main casing (outer box). The both inner and outer box are equipped with heater to stabilize the temperature. This stimulator is equipped with an additional heater at the bottom of the casing to warm the hardware, in case of very low temperatures. It will be adopted for the PB-2 stimulator if the PB-2 suffer the low temperature problem.

---

[18] Eccosorb®AN series

[19] Oriental Motor CMK235

[20] Oriental Motor CRK513

References

[1] E. Hubble. A Relation between Distance and Radial Velocity among Extra-Galactic Nebulae. *Proceedings of the National Academy of Science*, Vol. 15, pp. 168–173, March 1929.

[2] A. A. Penzias and R. W. Wilson. A Measurement of Excess Antenna Temperature at 4080 Mc/s. , Vol. 142, pp. 419–421, July 1965.

[3] NASA. LAMBDA. http://lambda.gsfc.nasa.gov/product/.

[4] Alan H. Guth. Inflationary universe: A possible solution to the horizon and flatness problems. *Phys. Rev. D*, Vol. 23, pp. 347–356, Jan 1981.

[5] A. D. Linde. A new inflationary universe scenario: A possible solution of the horizon, flatness, homogeneity, isotropy and primordial monopole problems. *Physics Letters B*, Vol. 108, pp. 389–393, February 1982.

[6] A. Albrecht and P. J. Steinhardt. Cosmology for grand unified theories with radiatively induced symmetry breaking. *Physical Review Letters*, Vol. 48, pp. 1220–1223, April 1982.

[7] A. D. Linde. Chaotic inflation. *Physics Letters B*, Vol. 129, pp. 177–181, September 1983.

[8] M. Tristram, A. J. Banday, K. M. Górski, R. Keskitalo, C. R. Lawrence, K. J. Andersen, R. B. Barreiro, J. Borrill, L. P. L. Colombo, H. K. Eriksen, R. Fernandez-Cobos, T. S. Kisner, E. Martínez-González, B. Partridge, D. Scott, T. L. Svalheim, and I. K. Wehus. Improved limits on the tensor-to-scalar ratio using bicep and planck, 2021.

[9] J. C. Mather, E. S. Cheng, Jr. Eplee, R. E., R. B. Isaacman, S. S. Meyer, R. A. Shafer, R. Weiss, E. L. Wright, C. L. Bennett, N. W. Boggess, E. Dwek, S. Gulkis, M. G. Hauser, M. Janssen, T. Kelsall, P. M. Lubin, Jr. Moseley, S. H., T. L. Murdock, R. F. Silverberg, G. F. Smoot, and D. T. Wilkinson. A Preliminary Measurement of the Cosmic Microwave Background Spectrum by the Cosmic Background Explorer (COBE) Satellite. , Vol. 354, p. L37, May 1990.

[10] D. J. Fixsen. THE TEMPERATURE OF THE COSMIC MICROWAVE BACKGROUND. *The Astrophysical Journal*, Vol. 707, No. 2, pp. 916–920, nov 2009.

[11] https://map.gsfc.nasa.gov/resources/cmbimages.html.

[12] Planck Collaboration, Akrami, Y., Arroja, F., Ashdown, M., Aumont, J., Baccigalupi, C., Ballardini, M., Banday, A. J., Barreiro, R. B., Bartolo, N., Basak, S., Benabed, K., Bernard, J.-P., Bersanelli, M., Bielewicz, P., Bock, J. J., Bond, J. R., Borrill, J., Bouchet, F. R., Boulanger, F., Bucher, M., Burigana, C., Butler, R. C., Calabrese, E., Cardoso, J.-F., Carron, J., Challinor, A., Chiang, H. C., Colombo, L. P. L., Combet, C., Contreras, D., Crill, B. P., Cuttaia, F., de Bernardis, P., de Zotti, G., Delabrouille,

J., Delouis, J.-M., Di Valentino, E., Diego, J. M., Donzelli, S., Doré, O., Douspis, M., Ducout, A., Dupac, X., Dusini, S., Efstathiou, G., Elsner, F., Enßlin, T. A., Eriksen, H. K., Fantaye, Y., Fergusson, J., Fernandez-Cobos, R., Finelli, F., Forastieri, F., Frailis, M., Franceschi, E., Frolov, A., Galeotta, S., Galli, S., Ganga, K., Gauthier, C., Génova-Santos, R. T., Gerbino, M., Ghosh, T., González-Nuevo, J., Górski, K. M., Gratton, S., Gruppuso, A., Gudmundsson, J. E., Hamann, J., Handley, W., Hansen, F. K., Herranz, D., Hivon, E., Hooper, D. C., Huang, Z., Jaffe, A. H., Jones, W. C., Keihänen, E., Keskitalo, R., Kiiveri, K., Kim, J., Kisner, T. S., Krachmalnicoff, N., Kunz, M., Kurki-Suonio, H., Lagache, G., Lamarre, J.-M., Lasenby, A., Lattanzi, M., Lawrence, C. R., Le Jeune, M., Lesgourgues, J., Levrier, F., Lewis, A., Liguori, M., Lilje, P. B., Lindholm, V., López-Caniego, M., Lubin, P. M., Ma, Y.-Z., Macías-Pérez, J. F., Maggio, G., Maino, D., Mandolesi, N., Mangilli, A., Marcos-Caballero, A., Maris, M., Martin, P. G., Martínez-González, E., Matarrese, S., Mauri, N., McEwen, J. D., Meerburg, P. D., Meinhold, P. R., Melchiorri, A., Mennella, A., Migliaccio, M., Mitra, S., Miville-Deschênes, M.-A., Molinari, D., Moneti, A., Montier, L., Morgante, G., Moss, A., Münchmeyer, M., Natoli, P., Nørgaard-Nielsen, H. U., Pagano, L., Paoletti, D., Partridge, B., Patanchon, G., Peiris, H. V., Perrotta, F., Pettorino, V., Piacentini, F., Polastri, L., Polenta, G., Puget, J.-L., Rachen, J. P., Reinecke, M., Remazeilles, M., Renzi, A., Rocha, G., Rosset, C., Roudier, G., Rubiño-Martín, J. A., Ruiz-Granados, B., Salvati, L., Sandri, M., Savelainen, M., Scott, D., Shellard, E. P. S., Shiraishi, M., Sirignano, C., Sirri, G., Spencer, L. D., Sunyaev, R., Suur-Uski, A.-S., Tauber, J. A., Tavagnacco, D., Tenti, M., Toffolatti, L., Tomasi, M., Trombetti, T., Valiviita, J., Van Tent, B., Vielva, P., Villa, F., Vittorio, N., Wandelt, B. D., Wehus, I. K., White, S. D. M., Zacchei, A., Zibin, J. P., and Zonca, A. Planck 2018 results - x. constraints on inflation. *A&A*, Vol. 641, p. A10, 2020.

[13] W. Hu and M. White. A CMB polarization primer. Vol. 2, pp. 323–344, October 1997.

[14] N. Aghanim, Y. Akrami, F. Arroja, M. Ashdown, J. Aumont, C. Baccigalupi, M. Ballardini, A. J. Banday, R. B. Barreiro, N. Bartolo, S. Basak, R. Battye, K. Benabed, J.-P. Bernard, M. Bersanelli, P. Bielewicz, J. J. Bock, J. R. Bond, J. Borrill, F. R. Bouchet, F. Boulanger, M. Bucher, C. Burigana, R. C. Butler, E. Calabrese, J.-F. Cardoso, J. Carron, B. Casaponsa, A. Challinor, H. C. Chiang, L. P. L. Colombo, C. Combet, D. Contreras, B. P. Crill, F. Cuttaia, P. de Bernardis, G. de Zotti, J. Delabrouille, J.-M. Delouis, F.-X. Désert, E. Di Valentino, C. Dickinson, J. M. Diego, S. Donzelli, O. Doré, M. Douspis, A. Ducout, X. Dupac, G. Efstathiou, F. Elsner, T. A. Enßlin, H. K. Eriksen, E. Falgarone, Y. Fantaye, J. Fergusson, R. Fernandez-Cobos, F. Finelli, F. Forastieri, M. Frailis, E. Franceschi, A. Frolov, S. Galeotta, S. Galli, K. Ganga, R. T. Génova-Santos, M. Gerbino, T. Ghosh, J. González-Nuevo, K. M. Górski, S. Gratton, A. Gruppuso, J. E. Gudmundsson, J. Hamann, W. Handley, F. K. Hansen, G. Helou, D. Herranz, S. R. Hildebrandt, E. Hivon, Z. Huang, A. H. Jaffe, W. C. Jones, A. Karakci, E. Keihänen, R. Keskitalo, K. Kiiveri, J. Kim, T. S. Kisner, L. Knox, N. Krachmalnicoff, M. Kunz, H. Kurki-Suonio, G. Lagache, J.-M. Lamarre, M. Langer, A. Lasenby, M. Lattanzi, C. R. Lawrence, M. Le Jeune, J. P. Leahy, J. Lesgourgues, F. Levrier, A. Lewis, M. Liguori, P. B. Lilje, M. Lilley, V. Lindholm, M. López-Caniego, P. M.

Lubin, Y.-Z. Ma, J. F. Macías-Pérez, G. Maggio, D. Maino, N. Mandolesi, A. Mangilli, A. Marcos-Caballero, M. Maris, P. G. Martin, M. Martinelli, E. Martínez-González, S. Matarrese, N. Mauri, J. D. McEwen, P. D. Meerburg, P. R. Meinhold, A. Melchiorri, A. Mennella, M. Migliaccio, M. Millea, S. Mitra, M.-A. Miville-Deschênes, D. Molinari, A. Moneti, L. Montier, G. Morgante, A. Moss, S. Mottet, M. Münchmeyer, P. Natoli, H. U. Nørgaard-Nielsen, C. A. Oxborrow, L. Pagano, D. Paoletti, B. Partridge, G. Patanchon, T. J. Pearson, M. Peel, H. V. Peiris, F. Perrotta, V. Pettorino, F. Piacentini, L. Polastri, G. Polenta, J.-L. Puget, J. P. Rachen, M. Reinecke, M. Remazeilles, C. Renault, A. Renzi, G. Rocha, C. Rosset, G. Roudier, J. A. Rubiño-Martín, B. Ruiz-Granados, L. Salvati, M. Sandri, M. Savelainen, D. Scott, E. P. S. Shellard, M. Shiraishi, C. Sirignano, G. Sirri, L. D. Spencer, R. Sunyaev, A.-S. Suur-Uski, J. A. Tauber, D. Tavagnacco, M. Tenti, L. Terenzi, L. Toffolatti, M. Tomasi, T. Trombetti, J. Valiviita, B. Van Tent, L. Vibert, P. Vielva, F. Villa, N. Vittorio, B. D. Wandelt, I. K. Wehus, M. White, S. D. M. White, A. Zacchei, and A. Zonca. Planck2018 results. *Astronomy Astrophysics*, Vol. 641, p. A1, Sep 2020.

[15] S. Takakura, M. A. O. Aguilar-Faúndez, Y. Akiba, K. Arnold, C. Baccigalupi, D. Barron, D. Beck, F. Bianchini, D. Boettger, J. Borrill, K. Cheung, Y. Chinone, T. Elleflot, J. Errard, G. Fabbian, C. Feng, N. Goeckner-Wald, T. Hamada, M. Hasegawa, M. Hazumi, L. Howe, D. Kaneko, N. Katayama, B. Keating, R. Keskitalo, T. Kisner, N. Krachmalnicoff, A. Kusaka, A. T. Lee, L. N. Lowry, F. T. Matsuda, A. J. May, Y. Minami, M. Navaroli, H. Nishino, L. Piccirillo, D. Poletti, G. Puglisi, C. L. Reichardt, Y. Segawa, M. Silva-Feaver, P. Siritanasak, A. Suzuki, O. Tajima, S. Takatori, D. Tanabe, G. P. Teply, and C. Tsai. Measurements of tropospheric ice clouds with a ground-based cmb polarization experiment, polarbear. *The Astrophysical Journal*, Vol. 870, No. 2, p. 102, Jan 2019.

[16] Planck Collaboration, Akrami, Y., Ashdown, M., Aumont, J., Baccigalupi, C., Ballardini, M., Banday, A. J., Barreiro, R. B., Bartolo, N., Basak, S., Benabed, K., Bersanelli, M., Bielewicz, P., Bond, J. R., Borrill, J., Bouchet, F. R., Boulanger, F., Bucher, M., Burigana, C., Calabrese, E., Cardoso, J.-F., Carron, J., Casaponsa, B., Challinor, A., Colombo, L. P. L., Combet, C., Crill, B. P., Cuttaia, F., de Bernardis, P., de Rosa, A., de Zotti, G., Delabrouille, J., Delouis, J.-M., Di Valentino, E., Dickinson, C., Diego, J. M., Donzelli, S., Doré, O., Ducout, A., Dupac, X., Efstathiou, G., Elsner, F., Enßlin, T. A., Eriksen, H. K., Falgarone, E., Fernandez-Cobos, R., Finelli, F., Forastieri, F., Frailis, M., Fraisse, A. A., Franceschi, E., Frolov, A., Galeotta, S., Galli, S., Ganga, K., Génova-Santos, R. T., Gerbino, M., Ghosh, T., González-Nuevo, J., Górski, K. M., Gratton, S., Gruppuso, A., Gudmundsson, J. E., Handley, W., Hansen, F. K., Helou, G., Herranz, D., Hildebrandt, S. R., Huang, Z., Jaffe, A. H., Karakci, A., Keihänen, E., Keskitalo, R., Kiiveri, K., Kim, J., Kisner, T. S., Krachmalnicoff, N., Kunz, M., Kurki-Suonio, H., Lagache, G., Lamarre, J.-M., Lasenby, A., Lattanzi, M., Lawrence, C. R., Le Jeune, M., Levrier, F., Liguori, M., Lilje, P. B., Lindholm, V., López-Caniego, M., Lubin, P. M., Ma, Y.-Z., Macías-Pérez, J. F., Maggio, G., Maino, D., Mandolesi, N., Mangilli, A., Marcos-Caballero, A., Maris, M., Martin, P. G., Martínez-González, E., Matarrese, S., Mauri, N., McEwen, J. D., Meinhold, P. R., Melchiorri, A., Mennella,

A., Migliaccio, M., Miville-Deschênes, M.-A., Molinari, D., Moneti, A., Montier, L., Morgante, G., Natoli, P., Oppizzi, F., Pagano, L., Paoletti, D., Partridge, B., Peel, M., Pettorino, V., Piacentini, F., Polenta, G., Puget, J.-L., Rachen, J. P., Reinecke, M., Remazeilles, M., Renzi, A., Rocha, G., Roudier, G., Rubiño-Martín, J. A., Ruiz-Granados, B., Salvati, L., Sandri, M., Savelainen, M., Scott, D., Seljebotn, D. S., Sirignano, C., Spencer, L. D., Suur-Uski, A.-S., Tauber, J. A., Tavagnacco, D., Tenti, M., Thommesen, H., Toffolatti, L., Tomasi, M., Trombetti, T., Valiviita, J., Van Tent, B., Vielva, P., Villa, F., Vittorio, N., Wandelt, B. D., Wehus, I. K., Zacchei, A., and Zonca, A. Planck 2018 results - iv. diffuse component separation. *A&A*, Vol. 641, p. A4, 2020.

[17] Deliang Wu, Hong Li, Shulei Ni, Zheng-Wei Li, and Cong-Zhan Liu. Detecting primordial gravitational waves: a forecast study on optimizing frequency distribution of next generation ground-based cmb telescope. *The European Physical Journal C*, Vol. 80, No. 2, p. 139, 2020.

[18] P.A.R. Ade, Z. Ahmed, M. Amiri, D. Barkats, R. Basu Thakur, C.A. Bischoff, D. Beck, J.J. Bock, H. Boenish, E. Bullock, V. Buza, J.R. Cheshire, J. Connors, J. Cornelison, M. Crumrine, A. Cukierman, E.V. Denison, M. Dierickx, L. Duband, M. Eiben, S. Fatigoni, J.P. Filippini, S. Fliescher, N. Goeckner-Wald, D.C. Goldfinger, J. Grayson, P. Grimes, G. Hall, G. Halal, M. Halpern, E. Hand, S. Harrison, S. Henderson, S.R. Hildebrandt, G.C. Hilton, J. Hubmayr, H. Hui, K.D. Irwin, J. Kang, K.S. Karkare, E. Karpel, S. Kefeli, S.A. Kernasovskiy, J.M. Kovac, C.L. Kuo, K. Lau, E.M. Leitch, A. Lennox, K.G. Megerian, L. Minutolo, L. Moncelsi, Y. Nakato, T. Namikawa, H.T. Nguyen, R. O'Brient, R.W. Ogburn, S. Palladino, T. Prouve, C. Pryke, B. Racine, C.D. Reintsema, S. Richter, A. Schillaci, R. Schwarz, B.L. Schmitt, C.D. Sheehy, A. Soliman, T.St. Germaine, B. Steinbach, R.V. Sudiwala, G.P. Teply, K.L. Thompson, J.E. Tolan, C. Tucker, A.D. Turner, C. Umiltà, C. Vergès, A.G. Vieregg, A. Wandui, A.C. Weber, D.V. Wiebe, J. Willmert, C.L. Wong, W.L.K. Wu, H. Yang, K.W. Yoon, E. Young, C. Yu, L. Zeng, C. Zhang, and S. Zhang. Improved constraints on primordial gravitational waves using planck , wmap, and bicep/ keck observations through the 2018 observing season. *Physical Review Letters*, Vol. 127, No. 15, Oct 2021.

[19] Y. Inoue, P. Ade, Y. Akiba, C. Aleman, K. Arnold, C. Baccigalupi, B. Barch, D. Barron, A. Bender, D. Boettger, J. Borrill, S. Chapman, Y. Chinone, A. Cukierman, T. de Haan, M. A. Dobbs, A. Ducout, R. Dünner, T. Elleflot, J. Errard, G. Fabbian, S. Feeney, C. Feng, G. Fuller, A. J. Gilbert, N. Goeckner-Wald, J. Groh, G. Hall, N. Halverson, T. Hamada, M. Hasegawa, K. Hattori, M. Hazumi, C. Hill, W. L. Holzapfel, Y. Hori, L. Howe, F. Irie, G. Jaehnig, A. Jaffe, O. Jeong, N. Katayama, J. P. Kaufman, K. Kazemzadeh, B. G. Keating, Z. Kermish, R. Keskitalo, T. S. Kisner, A. Kusaka, M. Le Jeune, A. T. Lee, D. Leon, E. V. Linder, L. Lowry, F. Matsuda, T. Matsumura, N. Miller, K. Mizukami, J. Montgomery, M. Navaroli, H. Nishino, H. Paar, J. Peloton, D. Poletti, G. Puglisi, C. R. Raum, G. M. Rebeiz, C. L. Reichardt, P. L. Richards, C. Ross, K. M. Rotermund, Y. Segawa, B. D. Sherwin, I. Shirley, P. Siritanasak, N. Stebor, R. Stompor, J. Suzuki, A. Suzuki, O. Tajima, S. Takada, S. Takatori, G. P. Teply, A. Tikhomirov, T. Tomaru, N. Whitehorn, A. Zahn, and O. Zahn. POLARBEAR-2: an instrument for CMB polarization measurements. In Wayne S. Holland and Jonas

Zmuidzinas, editors, *Millimeter, Submillimeter, and Far-Infrared Detectors and Instrumentation for Astronomy VIII*, Vol. 9914, pp. 372 – 380. International Society for Optics and Photonics, SPIE, 2016.

[20] Steve K. Choi, Matthew Hasselfield, Shuay-Pwu Patty Ho, Brian Koopman, Marius Lungu, Maximilian H. Abitbol, Graeme E. Addison, Peter A. R. Ade, Simone Aiola, David Alonso, and et al. The atacama cosmology telescope: a measurement of the cosmic microwave background power spectra at 98 and 150 ghz. *Journal of Cosmology and Astroparticle Physics*, Vol. 2020, No. 12, pp. 045–045, Dec 2020.

[21] Sumit Dahal, John W. Appel, Rahul Datta, Michael K. Brewer, Aamir Ali, Charles L. Bennett, Ricardo Bustos, Manwei Chan, David T. Chuss, Joseph Cleary, Jullianna D. Couto, Kevin L. Denis, Rolando Dünner, Joseph Eimer, Francisco Espinoza, Thomas Essinger-Hileman, Joseph E. Golec, Kathleen Harrington, Kyle Helson, Jeffrey Iuliano, John Karakla, Yunyang Li, Tobias A. Marriage, Jeffrey J. McMahon, Nathan J. Miller, Sasha Novack, Carolina Núñez, Keisuke Osumi, Ivan L. Padilla, Gonzalo A. Palma, Lucas Parker, Matthew A. Petroff, Rodrigo Reeves, Gary Rhoades, Karwan Rostem, Deniz A. N. Valle, Duncan J. Watts, Janet L. Weiland, Edward J. Wollack, and Zhilei Xu. Four-year cosmology large angular scale surveyor (class) observations: On-sky receiver performance at 40, 90, 150, and 220 ghz frequency bands, 2021.

[22] Güsten, R., Nyman, L. Å., Schilke, P., Menten, K., Cesarsky, C., and Booth, R. The atacama pathfinder experiment (apex) - a new submillimeter facility for southern skies -. *A&A*, Vol. 454, No. 2, pp. L13–L16, 2006.

[23] Frederick T. Matsuda, Satoru Takakura, Kam Arnold, David Boettger, Yuji Chinone, Masashi Hazumi, Brian Keating, Akito Kusaka, and Adrian T. Lee. Cross-polarization systematics due to Mizuguchi-Dragone condition breaking by a continuously rotating half-wave plate at prime focus in the Huan Tran telescope. In Jonas Zmuidzinas and Jian-Rong Gao, editors, *Millimeter, Submillimeter, and Far-Infrared Detectors and Instrumentation for Astronomy IX*, Vol. 10708, pp. 769 – 786. International Society for Optics and Photonics, SPIE, 2018.

[24] Cryomech Inc. http://www.cryomech.com.

[25]

[26] J. Groh. *Design and Deployment of the Simons Array Cosmic Microwave Background Polarization Instrument*. PhD thesis, University of California, Berkeley, 2021.

[27] Y. Inoue. Development of polarbear-2 receiver system for cosmic microwave background polarization experiment. 2016.

[28] Zotefoams plc, http://www.zotefoams.com.

[29] J. Choi, H. Ishitsuka, S. Mima, S. Oguri, K. Takahashi, and O. Tajima. Radio-transparent multi-layer insulation for radiowave receivers. *Review of Scientific Instruments*, Vol. 84, No. 11, 2013.

[30] Frederick. T.Matsuda. *Cosmic Microwave Background Polarization Science and Optical Design of the Polarbear and Simons Array Experiments.* PhD thesis, University of California, San Diego, 2017.

[31] Y. Inoue, T. Hamada, M. Hasegawa, M. Hazumi, Y. Hori, A. Suzuki, T. Tomaru, T. Matsumura, T. Sakata, T. Minamoto, and T. Hirai. Two-layer anti-reflection coating with mullite and polyimide foam for large-diameter cryogenic infrared filters. Vol. 55, p. D22, December 2016.

[32] Nihon Ceratech. http://www.ceratech.co.jp/product/#material.

[33] Charles A. Hill, Shawn Beckman, Yuji Chinone, Neil Goeckner-Wald, Masashi Hazumi, Brian Keating, Akito Kusaka, Adrian T. Lee, Frederick Matsuda, Richard Plambeck, and et al. Design and development of an ambient-temperature continuously-rotating achromatic half-wave plate for cmb polarization modulation on the polarbear-2 experiment. *Millimeter, Submillimeter, and Far-Infrared Detectors and Instrumentation for Astronomy VIII*, Jul 2016.

[34] Satoru Takakura, Mario Aguilar, Yoshiki Akiba, Kam Arnold, Carlo Baccigalupi, Darcy Barron, Shawn Beckman, David Boettger, Julian Borrill, Scott Chapman, Yuji Chinone, Ari Cukierman, Anne Ducout, Tucker Elleflot, Josquin Errard, Giulio Fabbian, Takuro Fujino, Nicholas Galitzki, Neil Goeckner-Wald, Nils W. Halverson, Masaya Hasegawa, Kaori Hattori, Masashi Hazumi, Charles Hill, Logan Howe, Yuki Inoue, Andrew H. Jaffe, Oliver Jeong, Daisuke Kaneko, Nobuhiko Katayama, Brian Keating, Reijo Keskitalo, Theodore Kisner, Nicoletta Krachmalnicoff, Akito Kusaka, Adrian T. Lee, David Leon, Lindsay Lowry, Frederick Matsuda, Tomotake Matsumura, Martin Navaroli, Haruki Nishino, Hans Paar, Julien Peloton, Davide Poletti, Giuseppe Puglisi, Christian L. Reichardt, Colin Ross, Praween Siritanasak, Aritoki Suzuki, Osamu Tajima, Sayuri Takatori, and Grant Teply. Performance of a continuously rotating half-wave plate on the polarbear telescope. *Journal of Cosmology and Astroparticle Physics*, Vol. 2017, No. 05, p. 008, 2017.

[35] C. Hill. *Sensitivity Simulations and Half-wave Plate Polarization Modulators for Cosmic Microwave Background Observatories.* PhD thesis, the University of California, Berkeley, 2020.

[36] K.D. Irwin and G.C. Hilton. *Transition-Edge Sensors*, pp. 63–150. Springer Berlin Heidelberg, Berlin, Heidelberg, 2005.

[37] A. Suzuki. *Multichroic Bolometric Detector Architecture for Cosmic Microwave Background Polarimetry Experiments.* PhD thesis, the University of California, Berkeley, 2013.

[38] http://www.cybernet.co.jp/ansys/product/lineup/hfss/.

[39] Praween Siritanasak, C. Aleman, Kamugisha Arnold, A. Cukierman, Masashi Hazumi, K. Kazemzadeh, B. Keating, T. Matsumura, A. Lee, C. Lee, E. Quealy, D. Rosen,

Nathan Stebor, and A. Suzuki. The broadband anti-reflection coated extended hemispherical silicon lenses for polarbear-2 experiment. *Journal of Low Temperature Physics*, Vol. 184, , 08 2016.

[40] A. Suzuki, P. Ade, Y. Akiba, C. Aleman, K. Arnold, C. Baccigalupi, B. Barch, D. Barron, A. Bender, D. Boettger, J. Borrill, S. Chapman, Y. Chinone, A. Cukierman, M. Dobbs, A. Ducout, R. Dunner, T. Elleflot, J. Errard, G. Fabbian, S. Feeney, C. Feng, T. Fujino, G. Fuller, A. Gilbert, N. Goeckner-Wald, J. Groh, T. D. Haan, G. Hall, N. Halverson, T. Hamada, M. Hasegawa, K. Hattori, M. Hazumi, C. Hill, W. Holzapfel, Y. Hori, L. Howe, Y. Inoue, F. Irie, G. Jaehnig, A. Jaffe, O. Jeong, N. Katayama, J. Kaufman, K. Kazemzadeh, B. Keating, Z. Kermish, R. Keskitalo, T. Kisner, A. Kusaka, M. L. Jeune, A. Lee, D. Leon, E. Linder, L. Lowry, F. Matsuda, T. Matsumura, N. Miller, K. Mizukami, J. Montgomery, M. Navaroli, H. Nishino, J. Peloton, D. Poletti, G. Puglisi, G. Rebeiz, C. Raum, C. Reichardt, P. Richards, C. Ross, K. Rotermund, Y. Segawa, B. Sherwin, I. Shirley, P. Siritanasak, N. Stebor, R. Stompor, J. Suzuki, O. Tajima, S. Takada, S. Takakura, S. Takatori, A. Tikhomirov, T. Tomaru, B. Westbrook, N. Whitehorn, T. Yamashita, A. Zahn, and O. Zahn. The Polarbear-2 and the Simons Array Experiments. *Journal of Low Temperature Physics*, Vol. 184, pp. 805–810, August 2016.

[41] Zigmund .D .K. *The POLARBEAR Experiment: Design and Characterization.* PhD thesis, University of California, Berkeley, 2012.

[42] F. Matsuda, L. Lowry, A. Suzuki, M. Aguilar Fáundez, K. Arnold, D. Barron, F. Bianchini, K. Cheung, Y. Chinone, T. Elleflot, G. Fabbian, N. Goeckner-Wald, M. Hasegawa, D. Kaneko, N. Katayama, B. Keating, A. T. Lee, M. Navaroli, H. Nishino, H. Paar, G. Puglisi, P. L. Richards, J. Seibert, P. Siritanasak, O. Tajima, S. Takatori, C. Tsai, and B. Westbrook. The polarbear fourier transform spectrometer calibrator and spectroscopic characterization of the polarbear instrument. *Review of Scientific Instruments*, Vol. 90, No. 11, p. 115115, Nov 2019.

[43] Benjamin Westbrook, Peter Ade, M. Aguilar, Y. Akiba, Kamugisha Arnold, Carlo Baccigalupi, D. Barron, D. Beck, Shawn Beckman, A. Bender, Federico Bianchini, D. Boettger, J. Borrill, Scott Chapman, Y. Chinone, Gabriele Coppi, K. Crowley, A. Cukierman, T. Haan, and A. Zahn. The polarbear-2 and simons array focal plane fabrication status. *Journal of Low Temperature Physics*, Vol. 193, , 12 2018.

[44] Darcy Barron, Kayla Mitchell, John Groh, Kam Arnold, Tucker Elleflot, Logan Howe, Jen Ito, Adrian T. Lee, Lindsay N. Lowry, Adam Anderson, Jessica Avva, Tylor Adkins, Carlo Baccigalupi, Kolen Cheung, Yuji Chinone, Oliver Jeong, Nobu Katayama, Brian Keating, Joshua Montgomery, Haruki Nishino, Christopher Raum, Praween Siritanasak, Aritoki Suzuki, Sayuri Takatori, Calvin Tsai, Benjamin Westbrook, and Yuyang Zhou. Integrated electrical properties of the frequency multiplexed cryogenic readout system for polarbear/simons array. *IEEE Transactions on Applied Superconductivity*, Vol. 31, No. 5, pp. 1–5, 2021.

[45] K. Hattori, Y. Akiba, K. Arnold, D. Barron, A. N. Bender, A. Cukierman, T. de Haan, M. Dobbs, T. Elleflot, M. Hasegawa, M. Hazumi, W. Holzapfel, Y. Hori, B. Keating, A. Kusaka, A. Lee, J. Montgomery, K. Rotermund, I. Shirley, A. Suzuki, and N. Whitehorn. Development of Readout Electronics for POLARBEAR-2 Cosmic Microwave Background Experiment. *Journal of Low Temperature Physics*, Vol. 184, pp. 512–518, July 2016.

[46] T. Elleflot. *Measuring the Polarization of the Cosmic Microwave Background with POLARBEAR-1 and Developing the Next-Generation Experiment POLARBEAR-2*. PhD thesis, UNIVERSITY OF CALIFORNIA SAN DIEGO, 2019.

[47] Lloyd Knox. Determination of inflationary observables by cosmic microwave background anisotropy experiments. *Physical Review D*, Vol. 52, No. 8, pp. 4307–4318, Oct 1995.

[48] Meir Shimon, Brian Keating, Nicolas Ponthieu, and Eric Hivon. Cmb polarization systematics due to beam asymmetry: Impact on inflationary science. *Phys. Rev. D*, Vol. 77, p. 083003, Apr 2008.

[49] Meir Shimon, Brian Keating, Nicolas Ponthieu, and Eric Hivon. Cmb polarization systematics due to beam asymmetry: Impact on inflationary science. *Physical Review D*, Vol. 77, No. 8, Apr 2008.

[50] N. J. Miller, M. Shimon, and B. G. Keating. Cmb beam systematics: Impact on lensing parameter estimation. *Phys. Rev. D*, Vol. 79, p. 063008, Mar 2009.

[51] Bicep2 Collaboration, P. A. R. Ade, R. W. Aikin, D. Barkats, S. J. Benton, C. A. Bischoff, J. J. Bock, J. A. Brevik, I. Buder, E. Bullock, C. D. Dowell, L. Duband, J. P. Filippini, S. Fliescher, S. R. Golwala, M. Halpern, M. Hasselfield, S. R. Hildebrandt, G. C. Hilton, K. D. Irwin, K. S. Karkare, J. P. Kaufman, B. G. Keating, S. A. Kernasovskiy, J. M. Kovac, C. L. Kuo, E. M. Leitch, M. Lueker, C. B. Netterfield, H. T. Nguyen, R. O'Brient, R. W. Ogburn, IV, A. Orlando, C. Pryke, S. Richter, R. Schwarz, C. D. Sheehy, Z. K. Staniszewski, R. V. Sudiwala, G. P. Teply, J. E. Tolan, A. D. Turner, A. G. Vieregg, C. L. Wong, and K. W. Yoon. Bicep2 III: Instrumental Systematics. *apj*, Vol. 814, p. 110, December 2015.

[52] M. Navaroli. *Precise Astronomical Polarization Angle Calibration and its Impact on Studying Lorentz and Parity Violation in the Cosmic Microwave Background*. PhD thesis, UNIVERSITY OF CALIFORNIA SAN DIEGO, 2021.

[53] G. Hinshaw, D. Larson, E. Komatsu, D. N. Spergel, C. L. Bennett, J. Dunkley, M. R. Nolta, M. Halpern, R. S. Hill, N. Odegard, L. Page, K. M. Smith, J. L. Weiland, B. Gold, N. Jarosik, A. Kogut, M. Limon, S. S. Meyer, G. S. Tucker, E. Wollack, and E. L. Wright. Nine-year wilkinson microwave anisotropy probe (wmap) observations: Cosmological parameter results. *The Astrophysical Journal Supplement Series*, Vol. 208, No. 2, p. 19, Sep 2013.

[54] M. Piat, G. Lagache, J. P. Bernard, M. Giard, and J. L. Puget. Cosmic background dipole measurements with the planck-high frequency instrument. *Astronomy and Astrophysics*, Vol. 393, No. 1, pp. 359–368, Sep 2002.

[55] The Polarbear Collaboration: P. A. R. Ade, Y. Akiba, A. E. Anthony, K. Arnold, M. Atlas, D. Barron, D. Boettger, J. Borrill, S. Chapman, Y. Chinone, M. Dobbs, T. Elleflot, J. Errard, G. Fabbian, C. Feng, D. Flanigan, A. Gilbert, W. Grainger, N. W. Halverson, M. Hasegawa, K. Hattori, M. Hazumi, W. L. Holzapfel, Y. Hori, J. Howard, P. Hyland, Y. Inoue, G. C. Jaehnig, A. H. Jaffe, B. Keating, Z. Kermish, R. Keskitalo, T. Kisner, M. Le Jeune, A. T. Lee, E. M. Leitch, E. Linder, M. Lungu, F. Matsuda, T. Matsumura, X. Meng, N. J. Miller, H. Morii, S. Moyerman, M. J. Myers, M. Navaroli, H. Nishino, A. Orlando, H. Paar, J. Peloton, D. Poletti, E. Quealy, G. Rebeiz, C. L. Reichardt, P. L. Richards, C. Ross, I. Schanning, D. E. Schenck, B. D. Sherwin, A. Shimizu, C. Shimmin, M. Shimon, P. Siritanasak, G. Smecher, H. Spieler, N. Stebor, B. Steinbach, R. Stompor, A. Suzuki, S. Takakura, T. Tomaru, B. Wilson, A. Yadav, and O. Zahn. A Measurement of the Cosmic Microwave Background B-mode Polarization Power Spectrum at Sub-degree Scales with POLARBEAR. Vol. 794, p. 171, October 2014.

[56] Amir Hajian, Viviana Acquaviva, Peter A. R. Ade, Paula Aguirre, Mandana Amiri, John William Appel, L. Felipe Barrientos, Elia S. Battistelli, John R. Bond, Ben Brown, Bryce Burger, Jay Chervenak, Sudeep Das, Mark J. Devlin, Simon R. Dicker, W. Bertrand Doriese, Joanna Dunkley, Rolando Dnner, Thomas Essinger-Hileman, Ryan P. Fisher, Joseph W. Fowler, Mark Halpern, Matthew Hasselfield, Carlos Hernández-Monteagudo, Gene C. Hilton, Matt Hilton, Adam D. Hincks, Renée Hlozek, Kevin M. Huffenberger, David H. Hughes, John P. Hughes, Leopoldo Infante, Kent D. Irwin, Jean Baptiste Juin, Madhuri Kaul, Jeff Klein, Arthur Kosowsky, Judy M. Lau, Michele Limon, Yen-Ting Lin, Robert H. Lupton, Tobias A. Marriage, Danica Marsden, Phil Mauskopf, Felipe Menanteau, Kavilan Moodley, Harvey Moseley, Calvin B. Netterfield, Michael D. Niemack, Michael R. Nolta, Lyman A. Page, Lucas Parker, Bruce Partridge, Beth Reid, Neelima Sehgal, Blake D. Sherwin, Jon Sievers, David N. Spergel, Suzanne T. Staggs, Daniel S. Swetz, Eric R. Switzer, Robert Thornton, Hy Trac, Carole Tucker, Ryan Warne, Ed Wollack, and Yue Zhao. THE ATACAMA COSMOLOGY TELESCOPE: CALIBRATION WITH THEWILKINSON MICROWAVE ANISOTROPY PROBEUSING CROSS-CORRELATIONS. *The Astrophysical Journal*, Vol. 740, No. 2, p. 86, oct 2011.

[57] P. A. R. Ade, R. W. Aikin, D. Barkats, S. J. Benton, C. A. Bischoff, J. J. Bock, J. A. Brevik, I. Buder, E. Bullock, C. D. Dowell, and et al. Bicep2. iii. instrumental systematics. *The Astrophysical Journal*, Vol. 814, No. 2, p. 110, Nov 2015.

[58] R. J. Thornton, P. A. R. Ade, S. Aiola, F. E. Angilè, M. Amiri, J. A. Beall, D. T. Becker, H-M. Cho, S. K. Choi, P. Corlies, and et al. The atacama cosmology telescope: The polarization-sensitive actpol instrument. *The Astrophysical Journal Supplement Series*, Vol. 227, No. 2, p. 21, Dec 2016.

[59] Y. D. Takahashi, P. A. R. Ade, D. Barkats, J. O. Battle, E. M. Bierman, J. J. Bock, H. C. Chiang, C. D. Dowell, L. Duband, E. F. Hivon, and et al. Characterization of the bicep telescope for high-precision cosmic microwave background polarimetry. *The Astrophysical Journal*, Vol. 711, No. 2, pp. 1141–1156, Feb 2010.

[60] C. Bischoff, A. Brizius, I. Buder, Y. Chinone, K. Cleary, R. N. Dumoulin, A. Kusaka, R. Monsalve, S. K. Næss, L. B. Newburgh, and et al. The q/u imaging experiment instrument. *The Astrophysical Journal*, Vol. 768, No. 1, p. 9, Apr 2013.

[61] J. T. Sayre, P. Ade, K. A. Aird, J. E. Austermann, J. A. Beall, D. Becker, B. A. Benson, L. E. Bleem, J. Britton, J. E. Carlstrom, and et al. Design and characterization of 90 ghz feedhorn-coupled tes polarimeter pixels in the sptpol camera. *SPIE Millimeter, Submillimeter, and Far-Infrared Detectors and Instrumentation for Astronomy VI*, Vol. 8452, pp. 974 – 985, Oct 2012.

[62] `http://sakaguchi-dennetsu.co.jp/lineup/heater/ceramic_heater_index/`.

[63] V F Duma. Theoretical approach on optical choppers for top-hat light beam distributions. *Journal of Optics A: Pure and Applied Optics*, Vol. 10, No. 6, p. 064008, apr 2008.

[64] Haruki Nishino, Darcy Barron, Amy N. Bender, Yuji Chinone, Kevin T. Crowley, Tucker Elleflot, John Groh, Masaya Hasegawa, Masashi Hazumi, Charles A. Hill, Haruaki Hirose, Logan Howe, Daisuke Kaneko, Shuhei Kikuchi, Theodore Kisner, Akito Kusaka, Joshua Montgomery, Alexandra S. Rahlin, Praween Siritanasak, Graeme Smecher, Satoru Takakura, Sayuri Takatori, Daiki Tanabe, Benjamin Westbrook, Nathan Whitehorn, Alex Zahn, and Yuyang Zhou. Data acquisition and management system for the CMB polarization experiment: Simons Array. In Jonas Zmuidzinas and Jian-Rong Gao, editors, *Millimeter, Submillimeter, and Far-Infrared Detectors and Instrumentation for Astronomy X*, Vol. 11453, pp. 328 – 340. International Society for Optics and Photonics, SPIE, 2020.

[65] Planck Collaboration, Yashar Akrami, Mark Ashdown, Jonathan Aumont, Carlo Baccigalupi, Mario Ballardini, A. Banday, Ramon Barreiro, Nicola Bartolo, Susanta Basak, K. Benabed, J. Bernard, M. Bersanelli, P. Bielewicz, Laura Bonavera, J. Bond, J. Borrill, François Bouchet, F. Boulanger, and Andrea Zacchei. Planck intermediate results. lii. planet flux densities. *Astronomy and Astrophysics*, Vol. 607, , 12 2016.

[66] D. Boettger. *CMB Polarization Measurements with the Polarbear Experiment.* PhD thesis, University of California, San Diego, 2017.

[67] Josquin Errard, Stephen M. Feeney, Hiranya V. Peiris, and Andrew H. Jaffe. Robust forecasts on fundamental physics from the foreground-obscured, gravitationally-lensed CMB polarization. *Journal of Cosmology and Astroparticle Physics*, Vol. 2016, No. 03, pp. 052–052, mar 2016.

[68] S. Takakura. *Characterization of a continuous polarization modulator using a half-wave plate for measurements of degree-scale cosmic microwave background with the POLARBEAR experiment.* PhD thesis, Osaka University, 2017.